Dissertation

submitted to the

Combined Faculties for the Natural Sciences and for Mathematics

of the Ruperto-Carola University of Heidelberg, Germany

for the degree of

Doctor of Natural Sciences

presented by

Diplom-Physiker Matthias Ruf

born in Freiburg

Oral examination: May 27th, 2009

Numerical studies of pair creation in counterpropagating laser fields

Referees: **Prof. Dr. Christoph H. Keitel**
Prof. Dr. Hans J. Pirner

Zusammenfassung

Paarerzeugung aus dem Vakuum durch elektromagnetische Felder ist wahrscheinlich eines der faszinierendsten Phänomene der Physik. Falls die Felder genügend stark sind wird das QED-Vakuum instabil. Infolge des enormen Fortschritts in der Lasertechnologie während der letzten Jahre kommt eine experimentelle Untersuchung rein Laser induzierter Paarerzeugung in Reichweite. Der Schwerpunkt dieser Arbeit liegt auf der Paarerzeugung in gegenläufigen Laserfeldern. Dabei wird die Erzeugungswahrscheinlichkeit durch die Benutzung numerisch gewonnener Lösungen der Dirac Gleichung berechnet. Falls die Felder rein zeitabhängig sind birgt der numerische Ansatz das Potential die Impulsverteilung der erzeugten Teilchen in einer einzigen Propagation zu erhalten. Darüber hinaus ermöglicht er die Magnetfeldkomponente der Laserfelder mit einzubeziehen, welche normalerweise vernachlässigt wird. Diese hat einen starken Einfluss auf den Paarerzeugungsprozess für hohe Laserfrequenzen.
Die angewandten numerischen Rechnungen stellen einen erheblichen Zeitaufwand dar, deshalb war das zweite Projekt dieser Arbeit die Entwicklung eines effizienten Programms um relativistische quantenmechanische Probleme zu lösen. Dies wurde durch die Anwendung des split-operator Verfahrens auf die Klein-Gordon Gleichung erreicht. Hierbei ergibt sich die Möglichkeit paralleles Rechnen einzusetzten. Jedoch spielt die damit zusammenhängende Spinstatistik eine entscheidende Rolle bei der Paarproduktion, welches an mehreren Beispielen gezeigt wird.

Abstract

Pair creation from vacuum induced by electromagnetic fields is probably one of the most intriguing phenomena in physics. If the fields are sufficiently strong, the QED vacuum become unstable. Due to the remarkable progress in laser technology during recent years an experimental investigation of pair creation by pure laser light is coming into reach. The focus of this thesis is on pair creation in counterpropagating laser beams. The pair creation probability is calculated employing the numerically obtained solutions of the Dirac equation. This numerical ansatz has the capability of calculating the momentum distribution of the created pairs in a single propagation, for pure time dependent field configurations. Furthermore, it allows to take the magnetic component of the laser fields into account, which is usually neglected. The latter strongly affects the creation process at high laser frequency.
The involved numerical calculations are rather time consuming, therefore the second project of this thesis was to develop a highly efficient code for solving relativistic quantum mechanical problems. This is accomplished by adopting the split-operator method to the Klein-Gordon equation. Here the possibility arises to use parallel computing. However the corresponding spin-statistics becomes crucial in the case of pair creation, demonstrated in several examples.

In connection with this thesis, the following articles were published in refereed journals:

- M. Ruf, G. R. Mocken, C. Müller, K. Z. Hatsagortsyan, and C. H. Keitel,
  Pair production in laser fields oscillating in space and time,
  Physical Review Letters **102**, 080402 (2009)
  [and March 2009 issue of Virtual Journal of Ultrafast Science]

- C. Müller, C. Deneke, M. Ruf, G. R. Mocken, K. Z. Hatsagortsyan, and C. H. Keitel,
  Lepton Pair Production in High-Frequency Laser Fields,
  Laser Physics **19**, 791 (2009)

Furthermore the following manuscripts have been submitted for publication or are in preparation:

- C. Müller, K. Z. Hatsagortsyan, M. Ruf, S. Müller, H. G. Hetzheim, M. C. Kohler, and C. H. Keitel,
  Relativistic Nonperturbative Above-Threshold Phenomena in Strong Laser Fields,
  submitted

- G. R. Mocken, M. Ruf, C. Müller, and C. H. Keitel,
  Resonant and non-resonant electron-positron pair creation in laser fields,
  in preparation

- M. Ruf, H. Bauke, and C. H. Keitel,
  A split-operator approach to the Klein-Gordon equation,
  in preparation

- M. Ruf, C. Müller, K. Z. Hatsagortsyan, G. R. Mocken, and C. H. Keitel,
  Spin effects in purely laser-induced pair creation,
  in preparation

Contents

Introduction

In the presence of very strong electromagnetic fields the quantum electrodynamic vacuum may become unstable and decay into electron-positron (e^+e^-) pairs [1–3]. The characteristic field strength for this vacuum instability is the Schwinger field $E_c \equiv m^2c^3/(|e|\hbar) = 1.3 \times 10^{16}$ V/cm, where m is the electron mass, c the speed of light, $\hbar$ the Planck constant, and e is the electron charge. This critical value corresponds to a field strength which generates an energy of the order of the rest mass on the Compton wavelength. One of the ways to produce such strong fields in the laboratory are heavy-ion collisions which have been extensively studied, both theoretically and experimentally (see e.g. the reviews in [4–7]).

Shortly after the invention of the laser almost 50 years ago, theoreticians began to study pair creation by intense laser light [8, 9]. In view of spectacular achievements in the generation of strong laser fields [10–12] and of opening perspectives for short wavelengths [13–16] and ultra-high intensities [17–19] (see also reviews [20–22]) the question arises whether the vacuum instability can also be tested with laser fields [23, 24]. The only observation of laser-induced pair creation until now was accomplished ten years ago at SLAC (Stanford, California), where a 46 GeV electron beam was brought into collision with an intense optical laser pulse [25]. In this experiment, a γ-photon produced via Compton scattering or the electron Coulomb field assisted the laser beam in the pair creation.

Pair creation from pure laser light has not been observed until now. It can, in principle, be realized e.g. in the superposition of two laser waves, since a single plane-wave laser field cannot extract any e^+e^- pairs from the vacuum, no matter what its intensity and frequency are. The special case of counter-propagating laser beams of equal intensity and frequency results in a standing laser wave. All theoretical investigations so far have approximated this standing laser wave by a spatially homogeneous electric field oscillating in time. This dipole approximation is expected to be well-justified in optical laser fields, where the wavelength is much larger than the typical length scale of the process. Several theorists have addressed pair creation in this field configuration employing various methods. The investigations started shortly after the invention of the laser in the 1970s [8, 9, 26–29] (see also [30] for a book review) and have recently been revived [31–43] by the large technological progress in laser technique. Also effects of the finite extent of focused laser pulses in space and time have been explored [44–49], as well as the influence of the laser magnetic-field component [50]. In general, the treatment of processes occurring in external fields which are inhomogeneous both in space and time, represents a challenging task for nonperturbative Quantum Field Theory [51–53].

The focus of this theoretical thesis is on pair creation in such a field configuration. The pair creation probability is calculated employing the solution of the Dirac equation, according to the field theoretical approach to vacuum decay in external fields with unstable vacuum [54]. In intuitive terms, this procedure is equivalent to describing the pair production as an electron transition from an initial negative-energy state (which corresponds to a positron in the final state) to a final positive-energy state.

The solutions of the Dirac equation are obtained numerically. An advanced computer code that solves the Dirac equation in an arbitrary external potential on a two-dimensional spatial grid [55, 56] is employed. However, these calculations are very time consuming. Therefore the second project of this thesis was to develop a highly efficient code for solving relativistic quantum mechanical problems. One step in this direction is the possibility to employ parallel computing. The split-operator method employed in the Dirac code utilizes Fourier transformations, and thus cannot be parallelized efficiently. Another relativistic quantum mechanical wave equation is given by the Klein-Gordon equation. However, the form of the Klein-Gordon equation differs from the usual Hamiltonian form of quantum mechanical equations of motion, because it is of second order in time. Therefore it is not directly accessible for the split-operator method. This obstacle may be overcome by introducing a new two-component wave function which transforms the Klein-Gordon equation into the desired form. Employing the split-operator method to the two-component Klein-Gordon equation provides some enormous advantages, among others the avoidance of Fourier transformations, and thus the possibility of parallelization. The Klein-Gordon equation describes spinless particles (bosons), whereas the Dirac equation describes sin-$\frac{1}{2}$ particles (fermions). However, the Klein-Gordon equation represents a good approximation to the Dirac equation, as long as the spin plays a minor role in the investigated problem. It turns out, that for the particular case of pair creation in external fields, the spin of the created particle is crucial, thus the investigation of e^+e^- pair creation has to employ the Dirac theory.

During this thesis, a highly efficient parallel computer code has been developed, propagating the Klein-Gordon equation on a one- or two- dimensional grid. This program was applied to several toy systems to test the performance and the correctness of the results. Furthermore, having a computer code at hand which propagates the Dirac equation, it was possible to investigate e^+e^- pair creation in counterpropagating laser fields for both dipole- and nondipole-approximation. The results obtained in the dipole case (oscillating electric field) are in accordance to former predictions, like Rabi oscillations of the transition probabilities. The numerical ansatz employed, has the capacity to yield the momentum distribution of the created particles in a single propagation, for pure time dependent external fields. A dramatic spin dependence is revealed for circular laser polarization, not obtained before, which can be explained by a spin modified quasiclassical calculation. Finally the influence of the magnetic field component of the laser pulse to the pair creation process was investigated. Here a strong influence is obtained for high laser frequency: the production probability is reduced, the resonant Rabi-oscillation pattern is distorted and the resonance positions are shifted, multiplied and split.

This thesis is structured as follows. The first chapter is dedicated to the Klein-Gordon equation and presents the application of the split-operator method to it. The main features of the Klein-Gordon code and the resulting advantages are shortly described, followed by a few simple but instructive examples, like the potential step leading to the Klein paradox. Here an alternative interpretation of this phenomenon is presented, which differs slightly from the usual textbook argument. Afterwards, the main topic of this thesis - pair creation in counterpropagating laser fields - is investigated. The first section of chapter 2 presents the Quantum Field Theoretical (QFT) fundament of the utilized computations. Apart from this section, the dipole approximation is employed throughout this chapter. Subsequent to a quasiclassical approach the main results are presented for both the Dirac and Klein-Gordon theory, to emphasize the influence of the spin statistics. The last section of this chapter presents a modified quasiclassical approach, including the spin degree of freedom. The last chapter refrains from the dipole approximation and takes the magnetic component of the laser fields into account.

Chapter 1

Klein-Gordon theory and algorithm

The first section of this chapter introduces the split-operator algorithm, a scheme to propagate an initial wave function in time, for the example of the Schrödinger equation. After this the Klein-Gordon equation is introduced, a relativistic wave equation for spinless particles. The main goal is to apply the split-operator algorithm to this equation. However, the form of the Klein-Gordon equation differs from the usual Hamiltonian form of quantum mechanical equations of motion, because it is of second order in time. Therefore it is not directly accessible for the split-operator method. One can overcome this obstacle by introducing a new two-component wave function which transforms the Klein-Gordon equation into the desired form. The third section illustrates the explicit application of the split-operator method onto the Klein-Gordon equation and the resulting advantages. In section 1.4 the main features of the computer code are presented, followed by a section with a few simple but instructive examples. The final section introduces the Dirac equation and the application of the split-operator method to it.

1.1 The split-operator algorithm

The state of a quantum mechanical system is described in position representation by a wave function $\psi(t, \boldsymbol{r})$. In nonrelativistic quantum mechanics the time evolution of this wave function under the influence of an external electromagnetic potential is governed by the Schrödinger equation [57]

$$i\hbar \frac{\partial \psi(t,\boldsymbol{r})}{\partial t} = \left[\frac{1}{2m} \left(\hat{\boldsymbol{p}} - \frac{q}{c} \boldsymbol{A}(t,\boldsymbol{r}) \right)^2 + q\phi(t,\boldsymbol{r}) \right] \psi(t,\boldsymbol{r}), \tag{1.1}$$

here m and q are the mass and the charge of the particle, $\hat{\boldsymbol{p}}$ denotes the momentum operator, whereas $\phi(t, \boldsymbol{r})$ and $\boldsymbol{A}(t, \boldsymbol{r})$ denote the scalar and vector potential of the external electromagnetic field, respectively. We shortly describe, how this equation is obtained to see later on the connection to the relativistic case. Starting with the usual nonrelativistic energy-momentum relation

$$E = \frac{\boldsymbol{p}^2}{2m}, \tag{1.2}$$

the free Schrödinger equation is obtained by replacing the physical quantities by operators, due to the correspondence rule:

$$E \to i\hbar\frac{\partial}{\partial t}, \quad \boldsymbol{p} \to \hat{\boldsymbol{p}} = -i\hbar\nabla. \tag{1.3}$$

In order to take the interaction with an external electromagnetic field into account, the free operators have to be modified, following the minimal coupling scheme:

$$i\hbar\frac{\partial}{\partial t} \to i\hbar\frac{\partial}{\partial t} - q\phi, \quad \hat{\boldsymbol{p}} \to \hat{\boldsymbol{p}} - \frac{q}{c}\boldsymbol{A}. \tag{1.4}$$

In this way one obtains the Schrödinger equation (1.1). It has a characteristic Hamiltonian form, defined by introducing the Hamilton operator $\hat{H}$,

$$i\hbar\frac{\partial\psi(t,\boldsymbol{r})}{\partial t} = \hat{H}(t,\boldsymbol{r})\psi(t,\boldsymbol{r}). \tag{1.5}$$

The main task is to obtain the time evolved wave function at a final time t_f, given an initial wave function at an initial time t_i. A formal solution of this problem is given by the time-evolution operator [58]

$$\hat{U}(t_2,t_1) = \hat{T}\exp\left(-\frac{i}{\hbar}\int_{t_1}^{t_2}dt'\hat{H}(t')\right), \tag{1.6}$$

$$\psi(t_f,\boldsymbol{r}) = \hat{U}(t_f,t_i)\psi(t_i,\boldsymbol{r}), \tag{1.7}$$

which is unitary, if the Hamiltonian is Hermitian, and $\hat{T}$ denotes the Dyson time ordering operator. However this is just a formal solution of equation (1.5), and in most cases the time-evolution operator (1.6) is not analytically computable. Many relevant systems require numerical methods, e.g. the split-operator method.

This numerical scheme goes back to a work by Feit *et al.* [59], where it was applied to the Schrödinger equation with a time-independent Hamiltonian. Later the method has been generalized to the Schrödinger equation with a time-dependent Hamiltonian [60]. Since then it was applied successfully to several other equations, e.g. the Dirac equation [55, 56, 61], the time-dependent Gross-Pitaevskii equation [62], and the nonlinear Schrödinger equation [63].

In general it is very difficult to transfer the time evolution operator (1.6) into a numerical propagation scheme. The crucial point is to split the time-evolution operator (1.6) into a product of operators which are diagonal either in position or momentum representation. For this reason, letting $\hat{O}$ denote an arbitrary operator, we introduce a new operator by

$$\hat{U}_{\hat{O}}(t_2,t_1,\kappa) = \exp\left(-\kappa\frac{i}{\hbar}\int_{t_1}^{t_2}dt'\hat{O}(t')\right). \tag{1.8}$$

Furthermore, we assume that the Hamiltonian can be written as a sum of two operators

$$\hat{H}(t) = \hat{K}(t) + \hat{V}(t), \tag{1.9}$$

e.g. the kinetic and the potential energy part. With this we are able to factorize the time-evolution operator (1.6) as

$$\hat{U}(t+\Delta t,t) = \hat{U}_{\hat{V}}\left(t+\Delta t,t,\frac{1}{2}\right)\hat{U}_{\hat{K}}\left(t+\Delta t,t,1\right)\hat{U}_{\hat{V}}\left(t+\Delta t,t,\frac{1}{2}\right) + \mathcal{O}(\Delta t^3). \tag{1.10}$$

The error $\mathcal{O}(\Delta t^3)$ stems from the non-commutativity of the kinetic and potential energy operators, i.e. $[\hat{K}, \hat{V}] \neq 0$. However, neglecting terms of order $\mathcal{O}(\Delta t^3)$ equation (1.10) gives an explicit unitary time-stepping scheme for the propagation of a wave function, which is accurate to second-order

$$\psi(t+\Delta t, \boldsymbol{r}) \approx \hat{U}_{\hat{V}}\left(t+\Delta t, t, \frac{1}{2}\right) \hat{U}_{\hat{K}}\left(t+\Delta t, t, 1\right) \hat{U}_{\hat{V}}\left(t+\Delta t, t, \frac{1}{2}\right) \psi(t, \boldsymbol{r}). \tag{1.11}$$

In the case of the Schrödinger equation (1.1) it is often possible to find a splitting of the Hamiltonian $\hat{H}$ such that the operator $\hat{U}_{\hat{K}}$ is diagonal in momentum representation and the operator $\hat{U}_{\hat{V}}$ is diagonal in position representation. Thus, the calculation of these operators becomes feasible in the appropriate space.
As an illustrative example we consider now the so-called dipole approximation, where it is assumed that the vector potential is homogeneous and thus purely time dependent $\boldsymbol{A}(t, \boldsymbol{r}) \approx \boldsymbol{A}(t)$. This approximation is applicable to a large class of potentials, where the interaction length is small compared to the spatial variation of the vector potential. Here it is possible to split the Hamiltonian into two operators

$$\hat{K}(t) = -\frac{\hbar^2}{2m}\nabla^2 + i\frac{\hbar q}{mc}\boldsymbol{A}(t)\cdot\nabla + \frac{q^2}{2mc^2}\boldsymbol{A}(t)^2, \tag{1.12}$$

$$\hat{V}(t) = q\phi(t, \boldsymbol{r}), \tag{1.13}$$

which separate the spatially dependent parts from spatial derivatives. Thus $\hat{U}_{\hat{V}}$ is diagonal in position space and $\hat{U}_{\hat{K}}$ is diagonal in momentum space. The crucial point in this example is the fact, that the vector potential does not depend on the spatial coordinate $\boldsymbol{r}$ explicitly. If it would depend on the spatial coordinate, the middle term in equation (1.12) would change into $\frac{i\hbar q}{2mc}\left(\nabla\boldsymbol{A}(t, \boldsymbol{r}) + 2\boldsymbol{A}(t, \boldsymbol{r})\cdot\nabla\right)$, which is spatially dependent and also contains spatial derivatives. Such a term makes it generally impossible to find an appropriate splitting.
In a numerical implementation, the wave function $\psi(t_i, \boldsymbol{r})$ is discretized on a rectangular grid of N points, and the time interval $t_f - t_i$ is divided into M steps of size $\Delta t = (t_f - t_i)/M$. After applying $\hat{U}_{\hat{V}}(t+\Delta t, t, \frac{1}{2})$ which is a multiplication in position space, one applies a Fourier transformation $\mathcal{F}$ onto the wave function, making the transition from position into momentum space. Here $\hat{U}_{\hat{K}}(t+\Delta t, t, 1)$, which contains spatial derivatives in position space, becomes a trivial multiplication-operator. After the application of this operator one has to Fourier-transform back into position space to apply $\hat{U}_{\hat{V}}(t+\Delta t, t, \frac{1}{2})$ again. This elementary step has to be applied until the final time t_f is reached:

$$\begin{aligned}\psi(t_f, \boldsymbol{r}) \approx\ & \hat{U}_{\hat{V}}\left(t_f, t_f - \Delta t, \frac{1}{2}\right) \mathcal{F}^{-1}\hat{U}_{\hat{K}}(t_f, t_f - \Delta t, 1) \\ \times \prod_{n=1}^{M-1} & \left[\mathcal{F}\,\hat{U}_{\hat{V}}\left(t_i + (n+1)\Delta t, t_i + (n-1)\Delta t, \frac{1}{2}\right) \mathcal{F}^{-1}\hat{U}_{\hat{K}}(t_i + n\Delta t, t_i + (n-1)\Delta t, 1)\right] \\ & \times \mathcal{F}\,\hat{U}_{\hat{V}}\left(t_i + \Delta t, t_i, \frac{1}{2}\right) \psi(t_i, \boldsymbol{r}).\end{aligned} \tag{1.14}$$

The most time consuming part in these calculations are the transformations from position into momentum space and vice versa. If these are accomplished by a Fast-Fourier-Transformation (FFT) the computation of an elementary step of the split-operator

method takes $\mathcal{O}(N \log N)$ operations. A big drawback is the bad scaling behavior of the FFT in parallel implementations. One can overcome this obstacle in the case of the Klein-Gordon equation to which we will turn in the next section.

1.2 The Klein-Gordon equation

The goal of this section is to obtain a relativistic generalization of the Schrödinger equation shortly described in the previous section, and bringing it to a form suitable for the split-operator method. Such an equation is the Klein-Gordon equation, which is a relativistic equation of motion for a scalar wave function [64–69]. It governs the behavior of a charged spinless particle under the influence of external electromagnetic potentials. The discovery of the Klein-Gordon equation may be attributed to various physicists. Depending on who is credited, the equation is named differently, see [70] for the history of the Klein-Gordon equation.
As in the previous section, we start with the now relativistic energy-momentum relation

$$E = c\sqrt{\boldsymbol{p}^2 + m^2c^2}. \tag{1.15}$$

Employing the correspondence rule directly to equation (1.15) would introduce an asymmetry between space and time components, which is not favorable in a relativistic theory. Furthermore it would lead to nonlocality effects. To avoid this, we take as a starting point the square of the relativistic energy-momentum relation (1.15) and substitute the classical quantities by operators as in equation (1.3). This leads to the free Klein-Gordon equation

$$-\hbar^2 \frac{\partial^2 \psi(x)}{\partial t^2} = \left[-c^2\hbar^2\nabla^2 + m^2c^4\right] \psi(x), \tag{1.16}$$

which has the following solutions

$$\psi_{\boldsymbol{p}}^{(\pm)} = \sqrt{\frac{mc^2}{EV}} \exp\left(\mp i \frac{p_\mu x^\mu}{\hbar}\right). \tag{1.17}$$

Here the plus-minus sign indicates the sign of the energy of the solutions, which can be both, positive or negative, and V denotes a normalization volume. The symbols x and p denote the four-vectors $x = (x^\mu) = (ct, \boldsymbol{r})$ and $p = (p^\mu) = (E/c, \boldsymbol{p})$, respectively. We employ the metric $g = (g^{\mu\nu}) = \mathrm{diag}(1, -1, -1, -1)$, therefore the product of two four-vectors $a = (a^\mu) = (a^0, \boldsymbol{a})$ and $b = (b^\mu) = (b^0, \boldsymbol{b})$ is given by $ab = a_\mu b^\mu = a^0 b^0 - \boldsymbol{ab}$.

At first sight a solution with negative energy might sound unphysical, and this was the first of two reasons why people abandoned this equation in the beginning and searched for another relativistic wave equation. However, as we will see later, these solutions are related to antiparticles and really have a physical meaning.

The next step is to employ the minimal coupling scheme, which enables us to take the interaction with an electromagnetic field into account. The explicit form of this coupling (1.4) follows from the requirement, that the equation has to be invariant under local gauge transformations, leading to the canonical form of the Klein-Gordon equation

$$\left[\left(i\hbar\frac{\partial}{\partial t} - q\phi\right)^2 - c^2\left(-i\hbar\nabla - \frac{q}{c}\boldsymbol{A}\right)^2 - m^2c^4\right] \psi(x) = 0. \tag{1.18}$$

In order to emphasize the relativistic character of this equation, it may be written in a manifestly covariant form

$$\left[\left(\hat{p}_\mu - \frac{q}{c}A_\mu\right)\left(\hat{p}^\mu - \frac{q}{c}A^\mu\right) - m^2c^2\right]\psi(x) = 0, \tag{1.19}$$

with the four-momentum operator $\hat{p} = (\hat{p}^\mu) = i\hbar(\partial^\mu) = i\hbar(\partial/c\partial t, -\nabla)$ and the four vector $A = (A^\mu) = (\phi, \boldsymbol{A})$. To gain more insight, we derive now the equation of continuity. Multiplication of the Klein-Gordon equation by ψ^* from the left, followed by a subtraction of the complex conjugate leads to

$$\frac{\partial\rho(x)}{\partial t} + \nabla\boldsymbol{j}(x) = 0 \quad \text{or} \quad \partial_\mu j^\mu(x) = 0, \tag{1.20}$$

with the four-current $(j^\mu) = (c\rho, \boldsymbol{j})$ given by

$$j^\mu = \frac{i\hbar}{2m}\left(\psi^*\partial^\mu\psi - \psi\partial^\mu\psi^*\right) - \frac{q}{mc}A^\mu\psi^*\psi. \tag{1.21}$$

This equation leads immediately to the conserved quantity

$$Q = \int d^3r\,\rho(x) = \text{const.} \tag{1.22}$$

Here the second problematic issue of the Klein-Gordon equation becomes visible, because the density $\rho = j^0/c$ can become negative. This is for example the case for all negative-energy solutions (1.17). At first sight, this renders a probabilistic interpretation of the density impossible. It is instructive at this point to examine the negative-energy solutions once again. The charge conjugation of a negative-energy solution $\psi_C^{(-)} = \psi^{(-)*}$ fulfills the canonical Klein-Gordon equation (1.18) in the same potentials with positive-energy and opposite charge $q \to -q$. So the negative-energy solutions become physically meaningful as representations of antiparticles. Therefore the Klein-Gordon equation describes two kinds of spinless particles, each with opposite charge, e.g. π^+ and π^-. With this new interpretation at hand it is possible to reinterpret the probability density $\rho(x)$ as a charge density $q\rho(x)$. Now it becomes also obvious why we chose the letter Q for the conserved quantity (1.22); it denotes the total charge which is of course conserved. Also the density current $\boldsymbol{j}$ is now reinterpreted as a charge current $q\boldsymbol{j}$.

As in the case of the Schrödinger equation, it is generally not possible to find analytic solutions of the Klein-Gordon equation (1.18). Therefore a numerical ansatz has to be found. Unfortunately, it is not possible to apply the split-operator method described in the previous section directly to this equation, because it is of second order in time and has not the usual Hamiltonian form (1.5) like the Schrödinger equation. However it is possible, by introducing a new two-component wave function, to transform the canonical Klein-Gordon equation into the desired Hamiltonian form [68, 69]. For this reason we introduce two new wave functions φ and χ as

$$\varphi + \chi = \psi, \tag{1.23}$$

$$\varphi - \chi = \frac{1}{mc^2}\left[i\hbar\frac{\partial}{\partial t} - q\phi\right]\psi, \tag{1.24}$$

resulting in the explicit expressions

$$\varphi = \frac{1}{2mc^2}\left[mc^2 + i\hbar\frac{\partial}{\partial t} - q\phi\right]\psi, \tag{1.25}$$

$$\chi = \frac{1}{2mc^2}\left[mc^2 - i\hbar\frac{\partial}{\partial t} + q\phi\right]\psi. \tag{1.26}$$

Now the Klein-Gordon equation (1.18) can be rewritten as

$$\left[i\hbar\frac{\partial}{\partial t} - q\phi\right](\varphi + \chi) = mc^2(\varphi - \chi), \tag{1.27}$$

$$\left[i\hbar\frac{\partial}{\partial t} - q\phi\right](\varphi - \chi) = \left[\frac{1}{m}\left(\hat{\boldsymbol{p}} - \frac{q}{c}\boldsymbol{A}\right)^2 + mc^2\right]\psi. \tag{1.28}$$

Subtracting and adding these two equations leads to a coupled system of differential equations, which both are of first order in time

$$i\hbar\frac{\partial\varphi}{\partial t} = \frac{1}{2m}\left(\hat{\boldsymbol{p}} - \frac{q}{c}\boldsymbol{A}\right)^2(\varphi + \chi) + (mc^2 + q\phi)\varphi, \tag{1.29}$$

$$i\hbar\frac{\partial\chi}{\partial t} = -\frac{1}{2m}\left(\hat{\boldsymbol{p}} - \frac{q}{c}\boldsymbol{A}\right)^2(\varphi + \chi) - (mc^2 - q\phi)\chi. \tag{1.30}$$

Combining φ and χ into a single two-component wave function

$$\Psi = \begin{pmatrix}\varphi\\ \chi\end{pmatrix} \tag{1.31}$$

leads to the final Klein-Gordon equation in the desired Hamiltonian form

$$i\hbar\frac{\partial\Psi}{\partial t} = \hat{H}\Psi, \tag{1.32}$$

with the new Klein-Gordon Hamiltonian

$$\hat{H} = \frac{\tau_3 + i\tau_2}{2m}\left(\hat{\boldsymbol{p}} - \frac{q}{c}\boldsymbol{A}\right)^2 + \tau_3 mc^2 + q\phi. \tag{1.33}$$

Here τ_1, τ_2 and τ_3 are the usual Pauli matrices

$$\tau_1 = \begin{pmatrix}0 & 1\\ 1 & 0\end{pmatrix}, \quad \tau_2 = \begin{pmatrix}0 & -i\\ i & 0\end{pmatrix}, \quad \tau_3 = \begin{pmatrix}1 & 0\\ 0 & -1\end{pmatrix}. \tag{1.34}$$

They obey the following algebra

$$\tau_i\tau_j = i\epsilon_{ijk}\tau_k + \delta_{ij}, \tag{1.35a}$$

$$[\tau_i, \tau_j] = 2i\epsilon_{ijk}\tau_k, \tag{1.35b}$$

$$\{\tau_i, \tau_j\} = 2\delta_{ij}. \tag{1.35c}$$

Note that this two-component wave function is not related to spin and is therefore not a spinor. To distinguish it explicitly from a spinor, we name this new two component quantity a "plexor". Also the Pauli matrices have in this framework no connection to spin.

It is an easy task to obtain the free solutions of the Klein-Gordon equation (1.32)

$$\Psi_{\boldsymbol{p}}^{(r)}(x) = \frac{1}{2\sqrt{mc^2 EV}} \begin{pmatrix} mc^2 + \epsilon_r E \\ mc^2 - \epsilon_r E \end{pmatrix} \exp\left[-i\epsilon_r \frac{p_\mu x^\mu}{\hbar}\right]. \tag{1.36}$$

The value of $r \in \{1, 2\}$ specifies the sign of the energy: $r = 1$ corresponds to a positive-energy solution ($\epsilon_1 = 1$), and $r = 2$ correspond to a negative-energy solution ($\epsilon_2 = -1$). They are normalized in the following way:

$$\int d^3 r \Psi_{\boldsymbol{p}}^{(r)\dagger}(x) \tau_3 \Psi_{\boldsymbol{p'}}^{(r')}(x) = \epsilon_r \frac{(2\pi)^3}{V} \delta_{rr'} \delta(\boldsymbol{p} - \boldsymbol{p'}), \tag{1.37}$$

which is in accordance with the charge density (1.46) below.

The Klein-Gordon Hamiltonian (1.33) is not Hermitian ($\hat{H}^\dagger \neq \hat{H}$) , because the matrix $\tau_3 + i\tau_2$ is not a Hermitian matrix. Instead, the Klein-Gordon Hamiltonian is a τ_3-pseudo-Hermitian operator [71, 72]. A linear operator $\hat{H}$ acting on a Hilbert space $\mathcal{H}$ is called $\hat{\eta}$-pseudo-Hermitian if there is a Hermitian operator $\hat{\eta}$ such that

$$\hat{\eta}^{-1} \hat{H}^\dagger \hat{\eta} = \hat{H}. \tag{1.38}$$

So let Ψ_1, $\Psi_2 \in \mathcal{H}$ and $\langle \Psi_1 | \Psi_2 \rangle$ be the inner product in $\mathcal{H}$. The operator $\hat{\eta}$ defines the pseudo-inner product

$$\langle \Psi_1 | \Psi_2 \rangle_{\hat{\eta}} = \langle \Psi_1 | \hat{\eta} | \Psi_2 \rangle. \tag{1.39}$$

Note, that the inner product (1.39) is not necessarily positive definite. The $\hat{\eta}$-pseudo-Hermitian operator $\hat{H}$ is Hermitian with respect to this inner product (1.39)

$$\begin{aligned} \langle \hat{H}\Psi_1 | \Psi_2 \rangle_{\hat{\eta}} &= \langle \Psi_1 | \hat{H}^\dagger \hat{\eta} | \Psi_2 \rangle \\ &= \langle \Psi_1 | \hat{\eta} \hat{H} | \Psi_2 \rangle \\ &= \langle \Psi_1 | \hat{H}\Psi_2 \rangle_{\hat{\eta}}. \end{aligned} \tag{1.40}$$

Having defined the notion of a pseudo-inner product and a pseudo-Hermitian operator, the next step is the definition of pseudo-unitarity. A linear invertible operator $\hat{U}$ acting on $\mathcal{H}$ is called $\hat{\eta}$-pseudo-unitary if

$$\hat{\eta}^{-1} \hat{U}^\dagger \hat{\eta} = \hat{U}^{-1}. \tag{1.41}$$

The inner product (1.39) is invariant under $\hat{\eta}$-pseudo-unitary transformations

$$\begin{aligned} \langle \hat{U}\Psi_1 | \hat{U}\Psi_2 \rangle_{\hat{\eta}} &= \langle \Psi_1 | \hat{U}^\dagger \hat{\eta} \hat{U} | \Psi_2 \rangle \\ &= \langle \Psi_1 | \hat{\eta} \hat{U}^{-1} \hat{U} | \Psi_2 \rangle \\ &= \langle \Psi_1 | \Psi_2 \rangle_{\hat{\eta}}. \end{aligned} \tag{1.42}$$

With regard to the split-operator method and the time evolution operator we show, that if $\hat{H}$ is an $\hat{\eta}$-pseudo-Hermitian operator, then the operator $\hat{U} = \exp[i\hat{H}]$ is $\hat{\eta}$-pseudo-

unitary:

$$\begin{aligned}
\hat{\eta}^{-1}\hat{U}^{\dagger}\hat{\eta} &= \hat{\eta}^{-1}\exp[-i\hat{H}^{\dagger}]\hat{\eta} \\
&= \sum_{n=0}^{\infty}\frac{(-i)^n}{n!}\hat{\eta}^{-1}(\hat{H}^{\dagger})^n\hat{\eta} \\
&= \sum_{n=0}^{\infty}\frac{(-i)^n}{n!}(\hat{\eta}^{-1}\hat{H}^{\dagger}\hat{\eta})^n \\
&= \sum_{n=0}^{\infty}\frac{(-i)^n}{n!}\hat{H}^n \\
&= \exp[-i\hat{H}] \\
&= \hat{U}^{-1}.
\end{aligned} \tag{1.43}$$

With these tools at hand, the pseudo-inner product of the Hamiltonian form of the Klein-Gordon theory is defined as

$$\langle\Psi_1|\Psi_2\rangle_{\tau_3} = \int d^3r\Psi_1^{\dagger}(x)\tau_3\Psi_2(x). \tag{1.44}$$

The pseudo-expectation value of an operator $\hat{O}$ is given by

$$\langle\hat{O}\rangle_{\tau_3} = \langle\Psi|\hat{O}|\Psi\rangle_{\tau_3} = \int d^3r\Psi^{\dagger}(x)\tau_3\hat{O}\Psi(x), \tag{1.45}$$

and the charge density (1.21) converts into the following instructive form

$$\rho(x) = \Psi^{\dagger}(x)\tau_3\Psi(x) = |\varphi(x)|^2 - |\chi(x)|^2. \tag{1.46}$$

From this it is quite obvious, that the density is not positive definite.

1.3 Application of the split-operator method to the Klein-Gordon equation

In section 1.1 we stated that the split-operator method is not applicable to the Schrödinger equation (1.1) for a particle in arbitrary electromagnetic potentials $\phi(t,\boldsymbol{r})$ and $\boldsymbol{A}(t,\boldsymbol{r})$, because there does not exist a splitting (1.9) of the Hamiltonian such that the operators $\hat{U}_{\hat{V}}(t_2,t_1,\kappa)$ and $\hat{U}_{\hat{K}}(t_2,t_1,\kappa)$ are diagonal in position space or in momentum space, respectively. The structure of the Klein-Gordon equation (1.32) is very similar to the Schrödinger equation (1.1). In fact, there is no appropriate splitting of the Klein-Gordon Hamiltonian (1.33) such that the operators $\hat{U}_{\hat{V}}(t_2,t_1,\kappa)$ and $\hat{U}_{\hat{K}}(t_2,t_1,\kappa)$ are diagonal in position or in momentum space, respectively. However, as shown below, it is possible to apply the split-operator method to the Klein-Gordon equation (1.32) without making $\hat{U}_{\hat{K}}(t_2,t_1,\kappa)$ diagonal in momentum space.
The Klein-Gordon Hamiltonian (1.33) is split into a kinetic energy part

$$\hat{K}(t,\boldsymbol{r}) = \frac{\tau_3 + i\tau_2}{2m}\left(-i\hbar\nabla - \frac{q}{c}\boldsymbol{A}(t,\boldsymbol{r})\right)^2, \tag{1.47}$$

and a potential energy part

$$\hat{V}(t,\boldsymbol{r}) = q\phi(t,\boldsymbol{r}) + \tau_3 mc^2. \tag{1.48}$$

With this splitting and the Pauli matrices (1.34), the operator $\hat{U}_{\hat{V}}(t_2,t_1,\kappa)$ becomes diagonal in position space and reduces to a simple multiplication operator

$$\begin{aligned} \hat{U}_{\hat{V}}(t+\Delta t,t,\kappa) &= \exp\left[-\kappa\frac{i}{\hbar}\int_t^{t+\Delta t} dt'\,\hat{V}(t',\boldsymbol{r})\right] \\ &= \exp\left[-\kappa\frac{i}{\hbar}\int_t^{t+\Delta t} dt'\,\left(q\phi(t',\boldsymbol{r})+\tau_3 mc^2\right)\right] \end{aligned} \tag{1.49}$$

$$= \begin{pmatrix} \exp\left[-\kappa\frac{i}{\hbar}\left(mc^2\Delta t + \int_t^{t+\Delta t} dt'\,q\phi(t',\boldsymbol{r})\right)\right] & 0 \\ 0 & \exp\left[\kappa\frac{i}{\hbar}\left(mc^2\Delta t - \int_t^{t+\Delta t} dt'\,q\phi(t',\boldsymbol{r})\right)\right] \end{pmatrix}.$$

The operator $\hat{U}_{\hat{K}}(t_2,t_1,\kappa)$ is neither diagonal in position space nor in momentum space. However this operator can be rewritten in position space by the Taylor series of the exponential function

$$\begin{aligned} \hat{U}_{\hat{K}}(t+\Delta t,t,\kappa) &= \exp\left[-\kappa\frac{i}{\hbar}\int_t^{t+\Delta t} dt'\,\hat{K}(t',\boldsymbol{r})\right] \\ &= \sum_{n=0}^{\infty}\frac{(\tau_3+i\tau_2)^n}{n!}\left[\frac{-i\kappa}{2m\hbar}\int_t^{t+\Delta t} dt'\,\left(-i\hbar\nabla - \frac{q}{c}\boldsymbol{A}(t',\boldsymbol{r})\right)^2\right]^n \end{aligned} \tag{1.50}$$

The infinite series comprises spatial derivatives of arbitrarily high order. However, the features of the Pauli algebra (1.35) allows to calculate (1.50) effortlessly, taking into account first- and second-order derivatives only. It turns out, that the matrix $(\tau_3+i\tau_2)$ is nilpotent

$$(\tau_3+i\tau_2)^2 = i\{\tau_2,\tau_3\} = 2i\delta_{23} = 0. \tag{1.51}$$

Therefore the series (1.50) reduces to

$$\hat{U}_{\hat{K}}(t+\Delta t,t,\kappa) = \mathbb{1} - i\kappa\frac{(\tau_3+i\tau_2)}{2m\hbar}\int_t^{t+\Delta t} dt'\,\left(-i\hbar\nabla - \frac{q}{c}\boldsymbol{A}(t',\boldsymbol{r})\right)^2. \tag{1.52}$$

In a numerical implementation of the split-operator method the wave function $\Psi(t,\boldsymbol{r})$ is discretized on a rectangular grid. It is propagated from time t to time $t+\Delta t$ by (1.11) where $\hat{U}_{\hat{V}}(t+\Delta t,t,\kappa)$ and $\hat{U}_{\hat{K}}(t+\Delta t,t,\kappa)$ are given by equations (1.49) and (1.52), respectively. The first- and second-order derivatives included in the operator (1.52) are approximated by a finite difference scheme. If the integrals over the potentials are not given analytically, they can be approximated numerically, e.g.

$$\int_t^{t+\Delta t} dt'\phi(t',\boldsymbol{r}) \approx \Delta t\phi(t,\boldsymbol{r}). \tag{1.53}$$

Note that in contrast to traditional split-operator methods, which operate alternately in position and momentum space, our split-operator scheme for the Klein-Gordon equation acts exclusively in position space. Thus, the application of (1.11) does not require the computation of a Fourier transform. This has two computational advantages:

- An elementary step of the split-operator method for the Klein-Gordon equation requires only $\mathcal{O}(N)$ operations, where N denotes the number of spatial grid points.

- The split-operator method for the Klein-Gordon equation can be parallelized efficiently on shared-memory parallel computers by domain decomposition.

1.4 The Klein-Gordon code in a nutshell

One of the main tasks of this work was to build up a computer code to propagate the Klein-Gordon equation. As the previous section described, the split-operator method is applicable to the Klein-Gordon equation in the Hamiltonian form. Using this numerical scheme has some essential advantages. It provides the possibility to circumvent the usual time consuming Fourier transformations from position into momentum space and vice versa, apparent in traditional split-operator schemes. Therefore arbitrary potentials with no further restrictions can be employed. As a second consequence, the algorithm can be parallelized on shared memory parallel computers by breaking the grid into smaller pieces. This is a huge advantage, because relativistic propagation methods suffer from the problem, that the time steps Δt have to be considerably smaller compared to nonrelativistic propagation schemes. For propagation schemes like the split-operator method, the requirement $\Delta t < \hbar/E$ has to be fulfilled. Due to the rest mass of the particle, the energy has a large numerical value, leading even for free particles to the condition $\Delta t < \hbar/mc^2$. Taking the electron as an example, the energy involved in the estimation of the time step for a nonrelativistic theory is of the order of several eV, whereas for the relativistic case one have $E \sim 511\,\mathrm{keV}$. This leads to a reduction of the time step size by approximately 4 to 5 orders of magnitude.

In the following, we present the main features of our numerical implementation of the Klein-Gordon theory.

Algorithm: An initial plexor-valued wave function $\Psi(t_i, \boldsymbol{r})$ is discretized on a one- or two-dimensional rectangular grid, with a constant grid increment. The propagation algorithm employed is similar to the one introduced in section 1.1 by equations (1.11) and (1.14). Applying successively the elementary propagation step from t to $t + \Delta t$

$$\Psi(t + \Delta t, \boldsymbol{r}) \approx \hat{U}_{\hat{V}}\left(t + \Delta t, t, \frac{1}{2}\right) \hat{U}_{\hat{K}}\left(t + \Delta t, t, 1\right) \hat{U}_{\hat{V}}\left(t + \Delta t, t, \frac{1}{2}\right) \Psi(t, \boldsymbol{r}), \qquad (1.54)$$

the initial wave function evolves in time under the influence of the given external electromagnetic potentials. Here the operators $\hat{U}_{\hat{V}}(t + \Delta t, t, \kappa)$ and $\hat{U}_{\hat{K}}(t + \Delta t, t, \kappa)$ are given by the equations (1.49) and (1.52), respectively. The propagation algorithm has the

following explicit form

$$\begin{aligned}\Psi(t_f,\boldsymbol{r}) &\approx \prod_{n=1}^{M}\left[\hat{U}_{\hat{V}}\left(t_i+n\Delta t,t_i+(n-1)\Delta t,\frac{1}{2}\right)\right. \\ &\times \left.\hat{U}_{\hat{K}}\left(t_i+n\Delta t,t_i+(n-1)\Delta t,1\right)\hat{U}_{\hat{V}}\left(t_i+n\Delta t,t_i+(n-1)\Delta t,\frac{1}{2}\right)\right]\Psi(t_i,\boldsymbol{r}) \\ &= \hat{U}_{\hat{V}}\left(t_f,t_f-\Delta t,\frac{1}{2}\right)\hat{U}_{\hat{K}}\left(t_f,t_f-\Delta t,1\right) \\ &\times \prod_{n=1}^{M-1}\left[\hat{U}_{\hat{V}}\left(t_i+(n+1)\Delta t,t_i+(n-1)\Delta t,\frac{1}{2}\right)\hat{U}_{\hat{K}}\left(t_i+n\Delta t,t_i+(n-1)\Delta t,1\right)\right] \\ &\times \hat{U}_{\hat{V}}\left(t_i+\Delta t,t_i,\frac{1}{2}\right)\Psi(t_i,\boldsymbol{r}),\end{aligned} \tag{1.55}$$

where M indicates the number of time steps $\Delta t=(t_f-t_i)/M$. Advantage was taken in the above propagation algorithm of the fact, that it is possible to combine two successive $\hat{U}_{\hat{V}}$-operators stemming from the left and right side of two neighboring elementary propagation steps (1.54).
The first- and second-order spatial derivatives in the operator $\hat{U}_{\hat{K}}(t+\Delta t,t,\kappa)$ are calculated by finite difference approximations. Here the accuracy can be improved by employing higher order formulae, which are implemented up to 9-point approximations. The accuracy of an n-point approximation is of the order $\mathcal{O}(h^{n-1})$, where h denotes the grid increment. The explicit formulas are given in Appendix A. It is also notable, that although the wave function has two components it suffices to calculate the derivatives of a single function, due to the explicit form of the matrix in (1.52)

$$\tau_3+i\tau_2=\begin{pmatrix}1 & 1\\ -1 & -1\end{pmatrix}. \tag{1.56}$$

Acting with this matrix on a plexor results in

$$(\tau_3+i\tau_2)\Psi=(\tau_3+i\tau_2)\begin{pmatrix}\varphi\\ \chi\end{pmatrix}=(\varphi+\chi)\begin{pmatrix}1\\ -1\end{pmatrix}. \tag{1.57}$$

So the differential operators act only on the former scalar wave function $\psi=\varphi+\chi$, equation (1.23).

Absorbing Boundary: During the propagation, there may be the possibility that parts of the wave packet hit the boundary, introducing reflection effects. To avoid these undesirable boundary effects, an absorbing boundary is employed. The wave function is damped to zero on the boundary by a successive application of the damping function

$$f(z)=\begin{cases}0 & , \text{ for } z\le a\\ \left(1+\exp\left[-2\tan\left(\frac{\pi}{2}-\frac{\pi(b-x)}{b-a}\right)\right]\right)^{-1} & , \text{ for } a<z<b\\ 1 & , \text{ for } b\le z\end{cases} \tag{1.58}$$

as shown in Figure (1.1). It is a smooth function $f\in\mathcal{C}^{\infty}$, meaning that it has continuous derivatives of all orders.

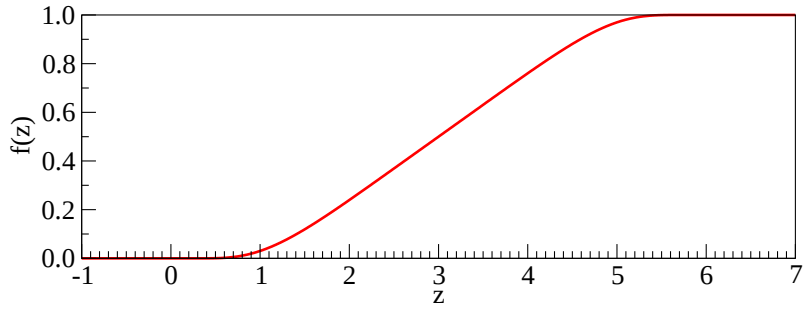

Figure 1.1: Shown is the boundary damping function (1.58) for the values $a = 0$ and $b = 6$. It is successively applied to the discretized wave packet in order to damp the function down to zero towards the boundary. This procedure avoids unwanted grid boundary effects, occurring otherwise whenever parts of the wave function move against the grid boundary.

Grid Adjustment: A crucial step to gain a highly efficient numerical code is to adjust the underlying grid to the propagated wave function in order to keep it as small as possible. The grid should follow the movement of the main part of the wave packet. It should also take into account the possibility that the wave packet changes its shape, becoming broader or narrower during the propagation. Adjusting the grid to a minimal required size will save valuable computing time. We implemented this idea by introducing two regions at the grid boundary, named "risk-zone" and "grey-zone", see Figure (1.2).

During the propagation of the wave function, the magnitude of the density (the density itself could be negative) is calculated after a specified number of time steps. Starting from the boundary, the positions are calculated where it reaches a pre-defined level height. In this way the "natural" boundary of the wave-packet is defined. The critical positions are those, which are nearest to the boundary. If these critical positions lie in the grey-zone, the grid has the optimal size. However, if a critical point lies in the

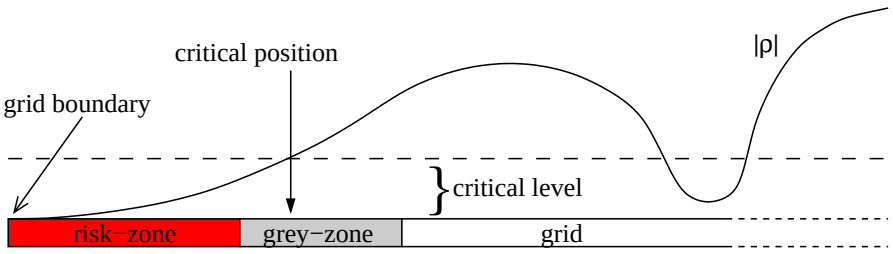

Figure 1.2: Schematic representation of the grid adjustment. The black solid curve represents the magnitude of the density, and the black dashed line corresponds to the critical level. The critical point is the position of the intersection of the former two, which lies nearest to the boundary. The grid is adjusted, depending on the location of the critical point compared to the two marked zones of the grid. In the example shown, the critical point lies in the grey-zone, meaning that the distance to the grid boundary has an optimal size on this side.

risk-zone, it is too close to the boundary. Therefore the grid is enlarged at this side until the critical position is in the middle of the grey-zone. On the contrary, if the critical point does not lie in the risk- or grey-zone, it is too far from the boundary, and the grid is too large at the investigated side. So it can be shrunk till the critical point lies again in the middle of the grey-zone. This grid adjusting method is schematically shown in Figure (1.2).

Parallelization: Due to the avoidance of Fourier transformations, the algorithm can be parallelized on shared-memory parallel computers by a grid decomposition. Here the grid is split into smaller ones, which are propagated individually. For the application of the operator $\hat{U}_{\hat{V}}(t+\Delta t, t, \kappa)$ this causes no difficulties. However the operator $\hat{U}_{\hat{K}}(t+\Delta t, t, \kappa)$ requires the calculation of derivatives. Therefore neighboring subgrids have to exchange the content of their boundary region, schematically shown in Figure (1.3). This was implemented by MPI (message passing interfaces) routines.
To test the parallel efficiency of our parallel Klein-Gordon code we examine how the computing time of the parallel code scales with the number of CPU's employed. For this reason we propagated freely a Gaussian wave packet over a fixed time interval, varying the number of CPU's. The purely computational time spend on each subgrid would scale in a perfectly linear manner. However the individual subgrids have to communicate with neighboring subgrids by sending and receiving data from their boundary regions. This data transfer is quite time consuming and the reason for a possible nonlinear behavior. The speed-up factor is given by $s = t_1/t_n$, where t_n denotes the running time of the program for n CPU's. The result is shown in Figure 1.4. It is notable that the speed-up factor follows almost the optimal linear behavior, showing the huge reduction of computational time via parallelization. All bumps belong to a prime number of CPU's employed, where the grid cannot be efficiently split. In fact in these cases, it is broken up into small stripes which causes a higher amount of exchanged data and therefore reduces the gain considerably.

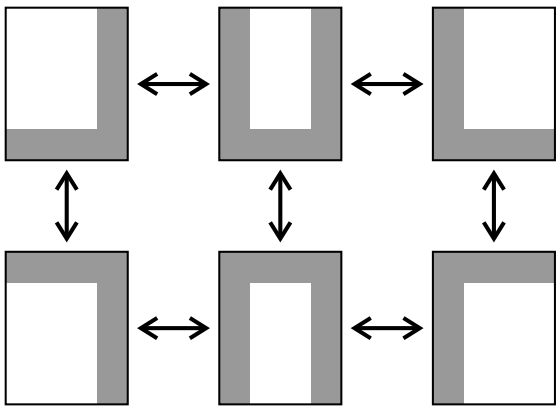

Figure 1.3: Splitting of the overall grid into smaller subgrids. During the application of the operator (1.52), neighboring subgrids have to exchange the content of their boundary regions (grey areas). This exchange is depicted by the black arrows.

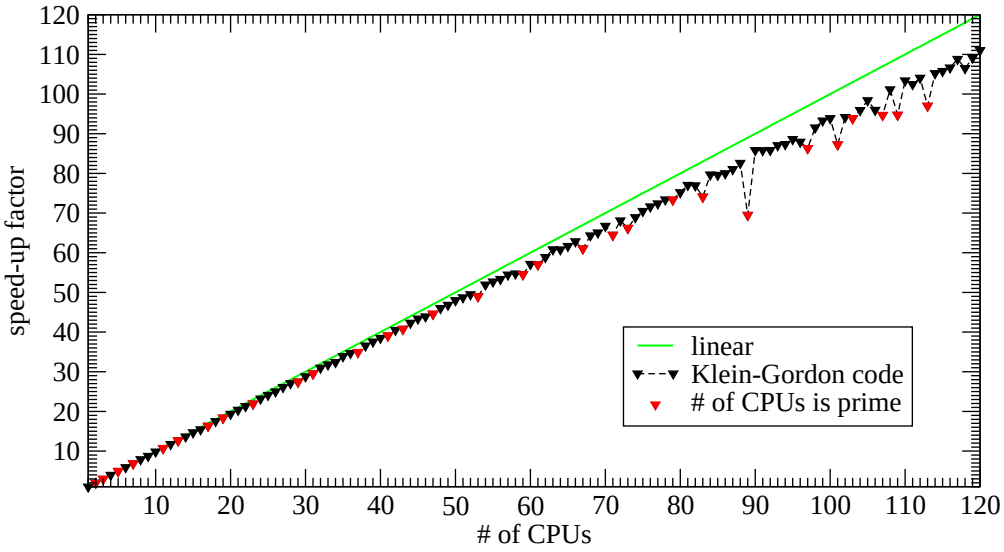

Figure 1.4: Speed-up factor versus the number of CPU's. The green solid curve represents the optimal linear behavior. The red triangles indicate that the number of CPU's is prime. At these points the grid cannot be split in an optimal fashion and therefore the data transfer is increased, which results in a breakdown of the speed-up factor.

1.5 Numerical examples of the Klein-Gordon code

Several instructive examples are presented in this section, serving two purposes: First to test, that the Klein-Gordon code yields correct results. At the same time, the examples are chosen in such a way, that relativistic effects become important. The first example considers the evolution of a free Gaussian wave packet, and introduces the concept of a Lorentz-boosted wave packet. For high values of the initial momentum and small spatial width, the results are substantially different compared to the nonrelativistic case. In the next example the propagation of an initially free particle under the influence of a plane-wave laser field is examined. The third example employs a two-dimensional harmonic oscillator potential. Here we focus on the relativistic influence on the motion along a circular orbit. After this, the potential step is investigated, which leads to the Klein paradox. We provide a slightly modified interpretation compared to the usual textbook explanation, e.g. [65–69]. Atomic units ($\hbar = |e| = m_e = 1$, $c = 137.036$) are employed throughout this section.

1.5.1 Evolution of a free Gaussian wave packet

A free Gaussian wave packet at rest is given in the scalar Klein-Gordon theory by

$$\psi^{(\pm)}_{\bar{\boldsymbol{p}}=0}(x) = \tilde{\mathcal{N}} \int d^3p \, \frac{1}{\sqrt{E}} \exp\left[-\frac{\boldsymbol{p}^2}{2\sigma^2}\right] \exp\left[\mp i p_\mu x^\mu\right], \tag{1.59}$$

with the normalization constant $\tilde{\mathcal{N}}$ and the width σ of the Gaussian distribution in momentum space. For nonzero momentum $\bar{\boldsymbol{p}} \neq 0$, the free particle wave packet should also have this Gaussian form in its rest frame. In order to find the wave function in

the laboratory frame, we need to apply a Lorentz transformation to the wave function (1.59):

$$\psi^{(\pm)}_{\bar{\boldsymbol{p}}=0}(x) \quad \rightarrow \quad \psi^{(\pm)}_{\bar{\boldsymbol{p}}}(x) = L(\bar{\boldsymbol{p}})\psi^{(\pm)}_{\bar{\boldsymbol{p}}}(\Lambda^{-1}(\bar{\boldsymbol{p}})x). \tag{1.60}$$

Here Λ denotes the boost into the laboratory frame. Because we have a scalar-valued function, the Lorentz transformation introduces just a constant phase factor $L(\bar{\boldsymbol{p}})$, which can be absorbed into the normalization constant. In this way we obtain the desired wave function in the laboratory frame:

$$\psi^{(\pm)}_{\bar{\boldsymbol{p}}}(x) = \mathcal{N}\int d^3p\,\frac{1}{\sqrt{E}}\exp\left[-\frac{\boldsymbol{p}^2}{2\sigma^2}\right]\exp\left[\mp ip_\mu(\Lambda^{-1})^\mu{}_\nu\,x^\nu\right]. \tag{1.61}$$

This may be rewritten, employing the substitution $p_\mu = \Lambda^\alpha{}_\mu\,p'_\alpha$

$$\begin{aligned}\psi^{(\pm)}_{\bar{\boldsymbol{p}}}(x) &= \mathcal{N}\int d^3p'\,\frac{\det(J)}{\sqrt{E(p')}}\exp\left[-\frac{\boldsymbol{p}^2(p')}{2\sigma^2}\right]\exp\left[\mp i\Lambda^\alpha{}_\mu\,p'_\alpha(\Lambda^{-1})^\mu{}_\nu\,x^\nu\right] \qquad (1.62)\\ &= \mathcal{N}\int d^3p'\,\frac{\det(J)}{\sqrt{E(p')}}\exp\left[-\frac{\boldsymbol{p}^2(p')}{2\sigma^2}\right]\exp\left[\mp ip'_\nu\,x^\nu\right].\end{aligned}$$

Here $\det(J)$ is the Jacobian of the above substitution. Because our code is two-dimensional, we restrict the Lorentz transformation to the x-y-plane. It can be decomposed into two rotations and a boost along the x-direction. The explicit form is given by

$$\Lambda = \begin{pmatrix} \gamma & \beta\gamma\cos(\theta) & \beta\gamma\sin(\theta) & 0\\ \beta\gamma\cos(\theta) & \gamma\cos^2(\theta)+\sin^2(\theta) & (\gamma-1)\cos(\theta)\sin(\theta) & 0\\ \beta\gamma\sin(\theta) & (\gamma-1)\cos(\theta)\sin(\theta) & \gamma\sin^2(\theta)+\cos^2(\theta) & 0\\ 0 & 0 & 0 & 1\end{pmatrix} \tag{1.63}$$

with $\gamma = \sqrt{1+\bar{\boldsymbol{p}}^2/(m^2c^2)}$, $\boldsymbol{\beta} = \bar{\boldsymbol{p}}/(mc\gamma)$, $\beta = |\boldsymbol{\beta}|$, and θ denotes the angle between $\bar{\boldsymbol{p}}$ and the x-axis. The inverse Lorentz transformation is given by $\Lambda^{-1}(\beta) = \Lambda(-\beta)$. The substitution from p to p' in the integral can be rewritten in matrix form as

$$\begin{pmatrix}\frac{E}{c}\\ \boldsymbol{p}\end{pmatrix} = \Lambda^{-1}\begin{pmatrix}\frac{E'}{c}\\ \boldsymbol{p}'\end{pmatrix}. \tag{1.64}$$

From this, the Jacobian determinant is easily obtained

$$\det(J) = \gamma\left(1-\frac{c\boldsymbol{\beta}\bar{\boldsymbol{p}}}{E'}\right). \tag{1.65}$$

The last step which remains to be done, is the transition from the scalar-valued function to the plexor-valued two-component representation. This is achieved by the transformations (1.25) and (1.26):

$$\begin{aligned}\Psi^{(\pm)}_{\bar{\boldsymbol{p}}}(x) &= \frac{1}{2mc^2}\begin{pmatrix}mc^2+i\frac{\partial}{\partial t}\\ mc^2-i\frac{\partial}{\partial t}\end{pmatrix}\psi^{(\pm)}_{\bar{\boldsymbol{p}}}(x) \qquad (1.66)\\ &= \mathcal{N}'\int\frac{d^3p'}{E'}\sqrt{E'-c\boldsymbol{\beta}\bar{\boldsymbol{p}}}\exp\left[-\frac{\boldsymbol{p}^2(p')}{2\sigma^2}\right]\begin{pmatrix}mc^2\pm E'\\ mc^2\mp E'\end{pmatrix}\exp\left[\mp ip'_\nu\,x^\nu\right].\end{aligned}$$

In the laboratory frame, these free Gaussian wave packets are Lorentz-contracted in the direction of their initial momentum $\bar{\boldsymbol{p}}$.

We turn now to the time evolution of such free Gaussian wave packets. As an example we consider propagations in one and two dimensions with an initial width $\sigma = 400$ a.u., an initial momentum $\bar{\boldsymbol{p}} = (100 \text{ a.u.}, 0)$ and positive energy. Due to the high value of σ, these wave packets are sharply peaked in position space $\Delta x \approx 0.002$ a.u..
The one-dimensional evolution is shown in Figure 1.5. From the nonrelativistic theory, one expects a broadening of the wave packet, accompanied by an additional movement in the direction of the initial momentum. However, instead of moving to the right in accordance with the initial momentum, the wave packet splits up in two parts, traveling into opposite directions. In addition, not shown in Figure 1.5, the initial wave packet has a negative charge density in the outer region.
Figure 1.6 shows the result for the two-dimensional calculation. Here even the initial wave packet in position space has not the expected Gaussian form. Although the initial state consists of a superposition of positive-energy states only, there are regions (the outer part around the main peak) where the charge density becomes negative. Similarly to the one-dimensional case, the behavior differs markedly from that of nonrelativistic theory. Instead of the usual broadening of the wave packet, a ring structure evolves with an inherent asymmetry with respect to the direction of the initial momentum.

The reason for the appearance of a partly negative charge density and the strange evolution behavior of the wave packet is provided by the following arguments. In a relativistic theory, it is not possible to measure the position of a particle to an arbitrary high precision. This is reflected in our case by the appearance of a negative charge density if the width in position space becomes smaller than a critical value $\Delta x_c \sim \lambda_C = 1/mc$, given by the Compton wave length λ_C of the particle. This critical value corresponds to a momentum uncertainty of $\Delta p_c \sim mc$, which corresponds to the lowest bound of pair creation. The approach to measure the position of a particle to a higher accuracy than Δx_c, would lead inevitably to particle-antiparticle pair creation, rendering the position measurement meaningless [73].
The deformation of the wave packet during the propagation from the usual Gaussian shape is due to the finite speed of light $c < \infty$. In order to keep the Gaussian shape, the portions with high momentum would have to move faster than the speed of light. This is of course impossible. Therefore, shock fronts build up which move approximately with the speed of light. In the one-dimensional simulation, these shock fronts correspond to the two parts traveling in opposite directions, whereas for the two-dimensional simulation the shock front occurs as the outward traveling ring.

These two examples of an extremely narrow Gaussian wave packet show rather drastically the difference between the nonrelativistic and relativistic theory. We point out that for a moderate width of the Gaussian distribution the differences become negligible.

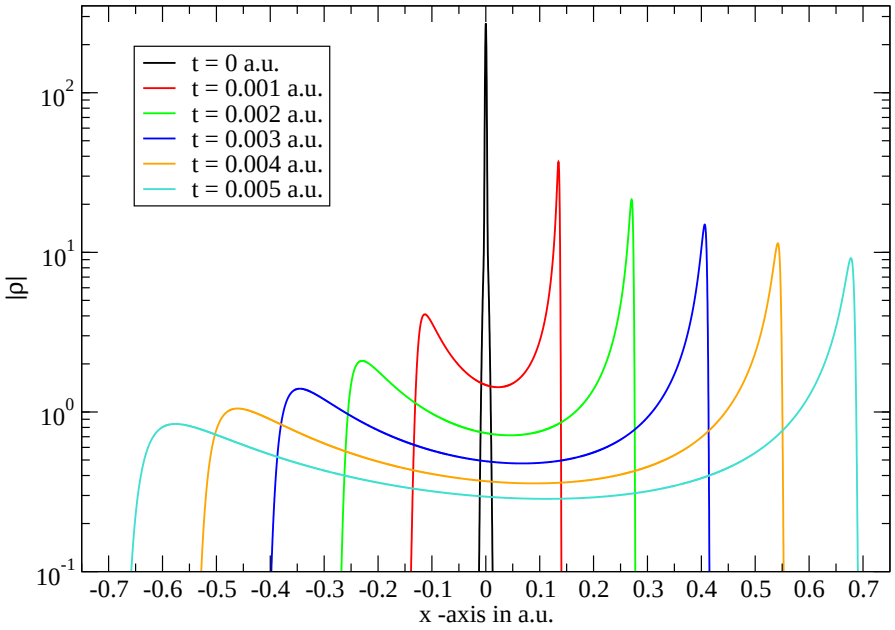

Figure 1.5: The time evolution of a narrow positive-energy Gaussian wave packet in one dimension with initial momentum $p = 100$ a.u. and a width in momentum space of $\sigma = 400$ a.u.. Plotted are the charge densities on a logarithmic scale. Instead of traveling along the initial momentum direction, the wave packet splits into two separating parts.

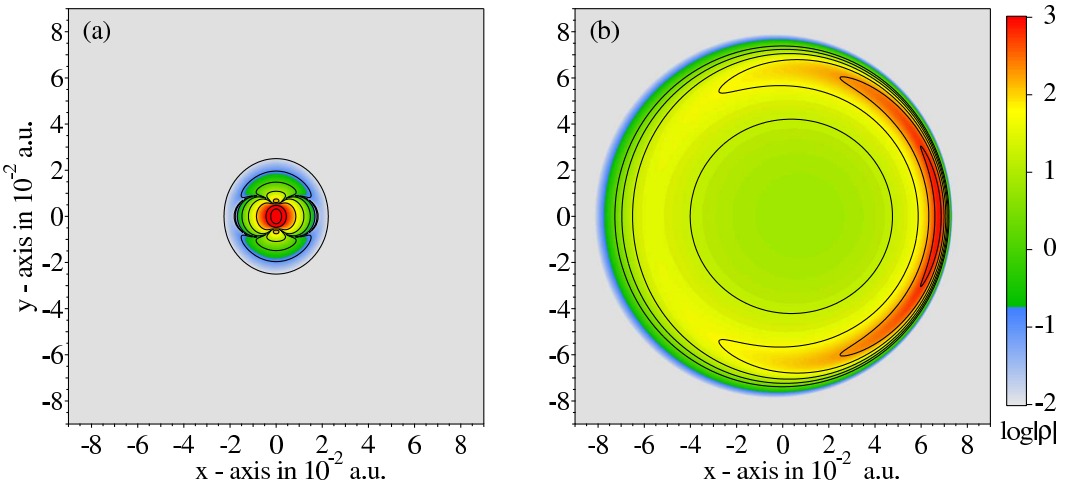

Figure 1.6: The time evolution of a narrow positive-energy Gaussian wave packet in two dimensions with initial momentum $\boldsymbol{p} = (100 \text{ a.u.}, 0)$ and a width in momentum space of $\sigma = 400$ a.u.. Plotted is the logarithm of the magnitude of the density. (a) Shown is the initial wave packet at $t = 0$ a.u., where the outer part around the main peak exhibits a negative charge density. The contour lines start at -2 with a spacing of 1. (b) Shown is the propagated state at $t = 0.0005$ a.u.. The contour lines drawn start at 0.5 with a spacing of 0.25. Instead of traveling along the initial momentum direction, a ring structure develops.

1.5.2 Motion in a relativistic laser field

During recent years, there has been an enormous progress in laser technology, reaching intensities of $10^{22} W/cm^2$. Even for much lower intensities, relativistic effects may become important for investigations of laser-matter interactions. A charged particle in a laser field represents a first step in this direction. A free electron in an external laser field enters the relativistic regime when the relativistic laser parameter $\xi = E_0/c\,\omega$ approaches or exceeds unity. Here ω and E_0 denote the laser frequency and field strength, respectively. We chose a linearly polarized plane-wave laser pulse, where the polarization axis corresponds to the y-direction and the pulse propagates from the left to the right in the x-direction. Introducing the laser phase $\eta = \omega(x/c - t)$, the vector potential is given by

$$\boldsymbol{A}(\eta) = \boldsymbol{e}_y \frac{cE_0}{\omega} \cos(\eta) g(\eta). \tag{1.67}$$

The pulse shape function $g(\eta)$ consists of a $\sin^2$-turn-on, followed by a constant plateau region and a $\sin^2$-turn-off.
For Figure 1.7 we took $\omega = 5\,\text{a.u.}$, $E_0 = 300\,\text{a.u.}$ and a pulse shape of the form (1|1|1), indicating that the turn-on, plateau and turn-off phases comprise one cycle each. With these field values we enter the weakly relativistic regime $\xi = 0.44 < 1$, and the signature of the relativistic Lorentz force becomes observable. This field is applied to a free positive-energy Gaussian wave packet at rest at the origin. The black curve depicts the center-of-charge trajectory and displays the typical zig-zag motion. The particle oscillates along the polarization axis with an amplitude [74]

$$\Delta y = \frac{E_0}{\omega^2}. \tag{1.68}$$

In addition it moves a distance Δx per cycle along the propagation direction

$$\Delta x = \frac{\pi E_0^2}{2c\omega^3}. \tag{1.69}$$

This second motion is due to the magnetic component of the Lorentz force, acting on the particle and pushing it along the laser propagation direction.

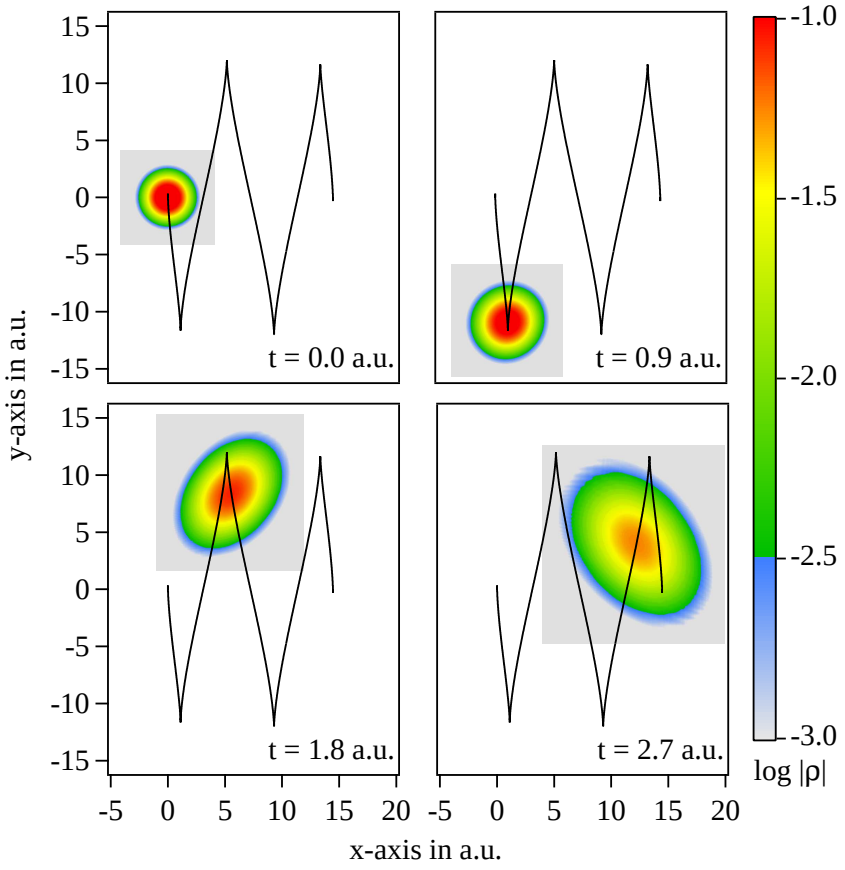

Figure 1.7: Example of the propagation of a free positive-energy Gaussian wave packet under the influence of an intense laser pulse ($E_0 = 300\,\text{a.u.}$, $\omega = 5\,\text{a.u.}$, (1|1|1) pulse shape). The black curve denotes the position expectation value, corresponding to the center of charge. Note how the grid moves along the particle trajectory and adjusts its size to the growing wave packet.

1.5.3 Harmonic oscillator

Here we investigate a circular orbit in a two dimensional harmonic oscillator potential. The initial position and momentum of the particle are $\boldsymbol{r}_i = (r_0, 0)$ and $\boldsymbol{p}_i = (0, p_0)$ in the x-y-plane. In nonrelativistic mechanics, this particle moves in an effective potential

$$V_{\text{eff}}(r) = V(r) + \frac{l^2}{2mr^2}, \tag{1.70}$$

where $l = r_0 p_0$ denotes the angular momentum. It is assumed that the potential $V(r)$ is invariant under rotations. For a harmonic oscillator the potential is given by $V(r) = \frac{1}{2}m\omega^2 r^2$. The position r_0 for which the trajectory is a circle depends on the initial momentum, and is found at the minimum of the effective potential

$$\left.\frac{\partial V_{\text{eff}}}{\partial r}\right|_{r=r_0} = 0, \tag{1.71}$$

resulting in a radius of the circular orbit of

$$r_0 = \frac{p_0}{m\omega}, \tag{1.72}$$

for our harmonic oscillator potential.

An effective potential may also be introduced in the relativistic case. Starting from the relativistic Lagrangian in polar coordinates (r, φ)

$$\mathcal{L} = -mc^2\sqrt{1 - \frac{1}{c^2}\left(\dot{r}^2 + r^2\dot{\varphi}^2\right)} - V(r), \tag{1.73}$$

one finds the conserved quantity

$$p_\varphi = l = \frac{\partial \mathcal{L}}{\partial \dot{\varphi}} = \frac{mr^2\dot{\varphi}}{\sqrt{1 - \frac{1}{c^2}\left(\dot{r}^2 + r^2\dot{\varphi}^2\right)}} = const., \tag{1.74}$$

and the Hamiltonian

$$\mathcal{H} = \frac{mc^2}{\sqrt{1 - \frac{1}{c^2}\left(\dot{r}^2 + r^2\dot{\varphi}^2\right)}} + V(r). \tag{1.75}$$

For a circular orbit, the condition $\dot{r} = 0$ has to be fulfilled. Inserting this in the Hamiltonian (1.75) and eliminating $\dot{\varphi}$ by equation (1.74), it is possible to define a relativistic effective potential

$$V_{\text{eff}}(r) = \sqrt{m^2c^4 + \frac{c^2 l^2}{r^2}} + V(r). \tag{1.76}$$

From the minimum of this effective potential one can again extract the relativistically modified radius of the circular orbit

$$\tilde{r}_0 = \frac{p_0}{m\omega}\left(1 + \left(\frac{p_0}{mc}\right)^2\right)^{-1/4} \tag{1.77}$$

$$= \frac{p_0}{m\omega}\left[1 - \frac{1}{4}\left(\frac{p_0}{mc}\right)^2 + \frac{5}{32}\left(\frac{p_0}{mc}\right)^4 + \mathcal{O}\left(\left(\frac{p_0}{mc}\right)^6\right)\right]. \tag{1.78}$$

The parameters have now to be chosen in such a manner, that the relativistic effect on the radius becomes visible. For this reason we take $\omega = 20\,\text{a.u.}$ and $p_0 = 150\,\text{a.u.}$, corresponding to a nonrelativistic radius of $r_0 = 7.5\,\text{a.u.}$. The relativistic radius turns out to be $\tilde{r}_0 \approx 6.16\,\text{a.u.}$. This is confirmed by our numerical propagation shown in Figure 1.8. The center of charge describes exactly a circle with a radius predicted by equation (1.77).

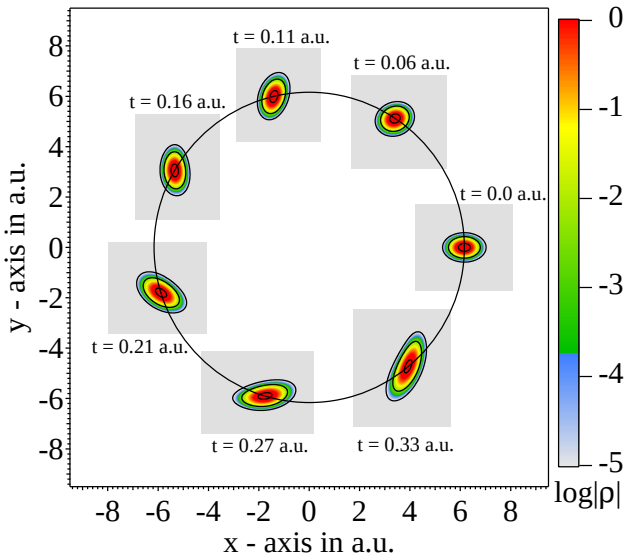

Figure 1.8: Time evolution of a wave packet in a harmonic oscillator potential with $\omega = 20\,\text{a.u.}$. The initial parameters are chosen in such a way, that the particle undergoes a circular motion. This is also an instructive example of the grid adjustment.

1.5.4 Potential step and the Klein paradox

The problem of a quantum particle impinging on a potential step is not only a toy system to check the numerical correctness of the Klein-Gordon code. It also leads to the famous Klein paradox [75]. This phenomenon, which is not known in nonrelativistic quantum mechanics, is connected to the phenomenon of pair creation due to the existence of negative-energy solutions. These, however, represent a major problem in the one-particle picture, which we have not met before. To elucidate this issue let us consider, for example, a pionic atom in its ground state, where the level scheme is schematically shown in Figure 1.9a. A radiation catastrophe would occur because there is no lowest allowed energy state. The particle could undergo transitions into lower and lower energy states by spontaneous emission of photons, resulting in unstable matter.
Not only the Klein-Gordon theory, describing spinless particles, is afflicted by this problem. The Dirac theory, describing spin-$\frac{1}{2}$ particles like the electron, has also the problem of negative-energy states. To resolve it, Dirac had the genius idea to postulate that all negative-energy states are occupied. Hence the vacuum is described by this so-called Dirac sea, Figure 1.9b. Because fermions satisfy the Pauli principle, transitions into negative-energy states would be prohibited, which solves the problem of the radiation catastrophe for the Dirac theory. This model leads also to an intuitive picture of the

concept of pair creation. Induced by the interaction of an external field, an electron from the Dirac sea may undergo a transition into a positive-energy state, Figure 1.9c, describing the creation process of an electron. The hole which is left behind behaves like a particle with opposite charge, opposite momentum and positive energy, thus representing a created positron. However this departs from the intended one-particle theory.

The problem still remains in the Klein-Gordon theory, because for bosons the Pauli principle is not valid. So, to postulate the occupation of all negative-energy states does not lead to a solution. However, for the one-particle theory one just postulates that transitions from positive- to negative-energy states or vice versa are not allowed, which leads to the same results as in the one-particle Dirac theory. Whenever such transitions occur, independent of the theory applied, one has to leave the one-particle picture, because pair creation processes become involved. One has to be very careful in interpreting such results from the one-particle theory which are composed of both, positive- and negative-energy states. We will encounter this issue later on when interpreting the Klein paradox.

We focus now on the potential step given by

$$\phi(\boldsymbol{r}) = \begin{cases} 0 & , \quad \text{for } x < 0 \\ \phi_0 & , \quad \text{for } 0 \leq x. \end{cases} \tag{1.79}$$

In all cases considered, a positive-energy particle approaches the potential step from the left under an angle of $\pi/4$, i.e., with the initial momentum $\boldsymbol{p}_0 = (p, p)$ in the x-y-plane. The magnitude of the initial momentum determines the energy of the incoming particle. Of course, the potential step is an analytically solvable problem, giving two different wave functions for the left side (region I) and the right side (region II) of the step. These two wave functions and also their derivatives have to match at the common boundary. If the step height is sufficiently low, meaning $\phi_0 < 2mc^2$, energies fulfilling

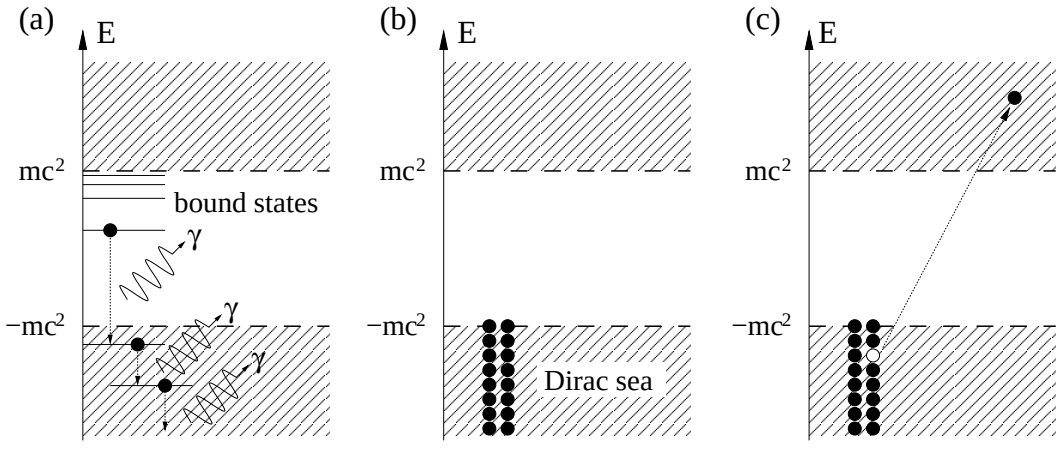

Figure 1.9: (a) Radiation catastrophe. The existence of negative energy states would lead to unstable matter. (b) Postulation of the Dirac sea: all negative-energy states are occupied, circumventing the radiation catastrophe. (c) Pair creation process in the framework of the Dirac sea. A particle undergoes a transition from the Dirac sea into a positive-energy state. The hole which is left behind, represents the antiparticle.

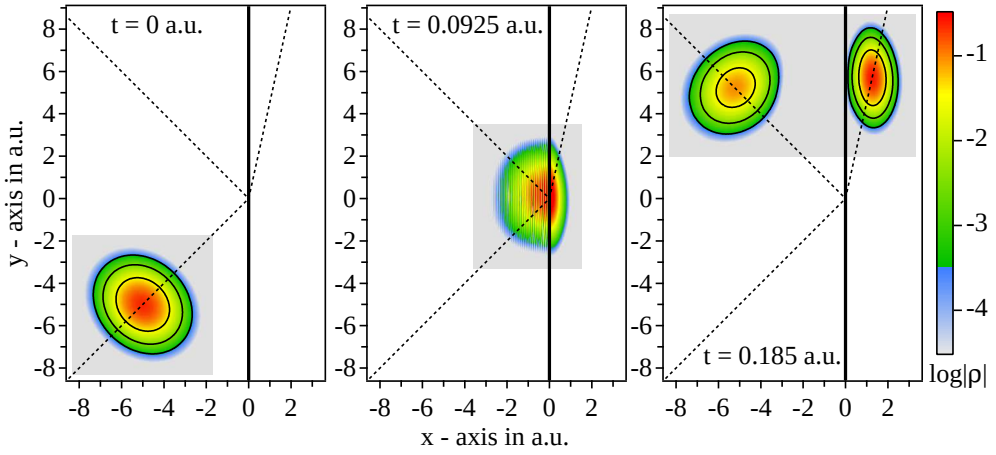

Figure 1.10: Time evolution of a wave packet approaching a potential step, indicated by the black solid line. Here the energy exceeds the height of the potential step. The black dashed lines depict the propagation directions for the individual parts of the wave packet in correspondence with equation (1.80). This is also a beautiful example of the grid adjustment indicated by the grey boxes.

$E > \phi_0 + mc^2$ result in oscillating functions in both regions. For lower energies, the wave function is exponentially damped in region II.
As a first example we consider an energy which is higher than the potential step. Thus a part of the wave packet propagates further to the right whereas a portion of it is reflected. A simple calculation gives the angle between the x-axis and the direction in which the transmitted part of the wave packet propagates

$$\tan(\theta) = \frac{p}{mc}\left[\left(\sqrt{1+2\left(\frac{p}{mc}\right)^2} - \frac{\phi_0}{mc^2}\right)^2 - \left(\frac{p}{mc}\right)^2 - 1\right]^{-1/2}. \tag{1.80}$$

For $\phi_0 < 2mc^2$, equation (1.80) delivers real values only for energies which are higher than $(\phi_0 + mc^2)$, with the limit

$$\lim_{p\to\infty} \theta = \frac{\pi}{4}. \tag{1.81}$$

The time evolution is shown in Figure 1.10 for a step height of $\phi_0 = 0.1mc^2 \approx 1877.9$ a.u. and an initial momentum of $p = 68$ a.u.. For these parameters equation (1.80) predicts an angle of $\theta = 77.6°$, which corresponds to the angle of the black dashed line on the right side of the pictures.
In the second example the step height is increased till it exceeds the critical value of $2mc^2$, taking $\phi_0 = 2.5mc^2$. Here the solution shows a different behavior than the one known from nonrelativistic theories. We have to examine three different energy regimes of the incoming particle. The solutions in region I are oscillating functions in all three cases. For region II one finds:

- For $\phi_0 + mc^2 < E$, the solutions are oscillating functions as expected. So the wave packet can propagate further to the right and splits up into a reflected and a transferred part.

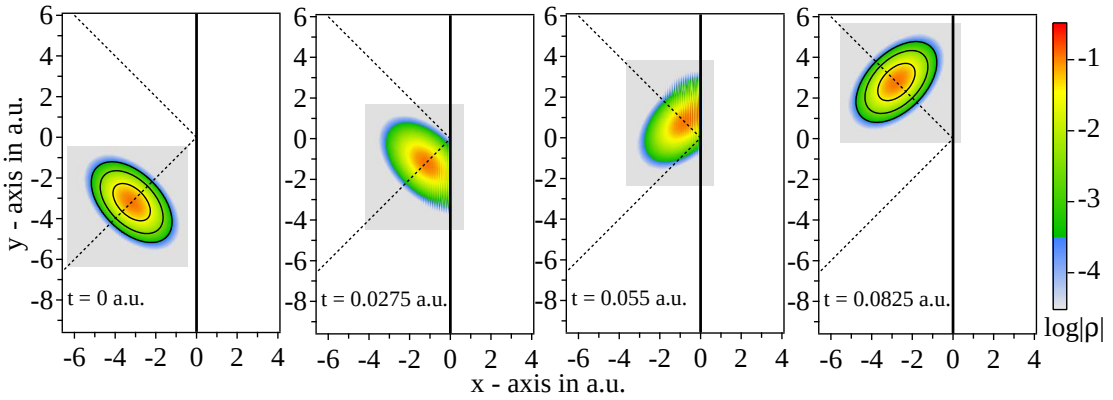

Figure 1.11: Time evolution of a wave packet approaching a supercritical potential step. The initial momentum is large, so the Klein paradox does not occur. The wave packet is totally reflected at the potential step.

- For $\phi_0 - mc^2 < E < \phi_0 + mc^2$, the solutions are again exponentially damped. Therefore the wave packet will be completely reflected in this case.
- A new situation arises for $mc^2 < E < \phi_0 - mc^2$. Here the solutions show again an oscillating behavior. Therefore a transmitted wave exists with an energy smaller than the step height. This phenomenon is known as the Klein paradox [75].

The last two cases are shown in Figure 1.11 and 1.12, respectively. First we chose $p = 133.2\,\text{a.u.}$, corresponding to an energy which lies in the second regime. Here the wave packet is totally reflected. If the momentum is decreased until it falls under a critical value, in our case $p = 80.5\,\text{a.u.} < p_c \approx 108.3\,\text{a.u.}$, one enters the regime of the Klein paradox. In addition to a reflected part, a portion of the wave packet propagates further into the normally forbidden region. This portion has negative density, and consists in fact of negative-energy states. So both negative- and positive-energy states are involved in this regime and one is forced to leave the one-particle picture.
The usual textbook argument [65–69] states, that the incoming particle is totally reflected at the potential step. However, during this reflection a particle antiparticle pair is created additionally. So the portion of the wave packet which propagates into the forbidden region to the right is interpreted as the created antiparticle. Coming from the one-particle picture this interpretation might seem correct. However, from a physical point of view the question arises, why there is only pair creation for small initial momenta and not for higher energetic ones?
To resolve this problem one has to leave the one-particle picture. In a quantum field theoretical treatment, it can be shown that a supercritical potential step produces intrinsically pairs out of the vacuum. Here it becomes obvious, that a one-particle interpretation cannot be correct. For the Dirac theory it was shown recently [38, 39] that the incoming particle actually suppresses this intrinsic pair creation process. This provides a slightly modified explanation of the Klein-Gordon paradox, which fits also quite well into the Dirac sea picture, shown in Figure 1.13. For subcritical ϕ_0 the incoming particle encounters an usual potential step (Figure 1.13a). However, if the potential step becomes supercritical, particles from the Dirac sea in region II can leak out into region

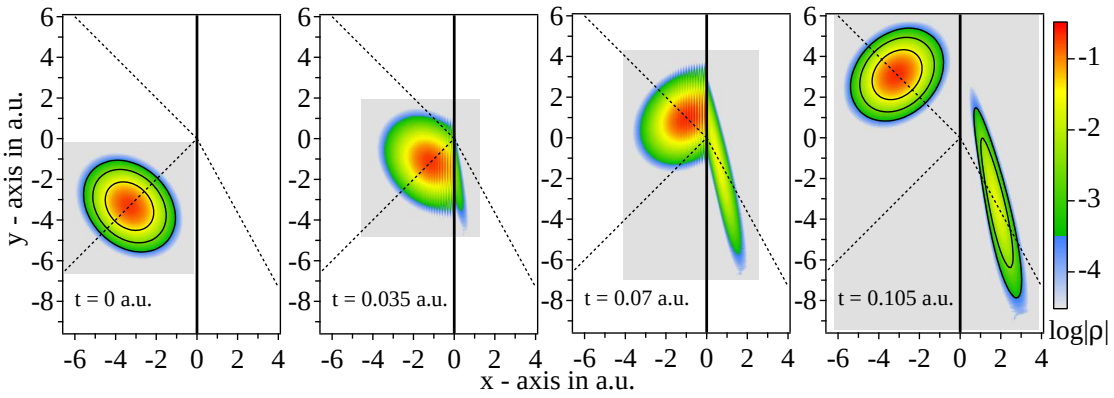

Figure 1.12: Time evolution of a wave packet approaching the same supercritical potential step as in Figure 1.11. In this case however, the initial momentum is low, leading to the Klein paradox. Although the main part is reflected, a small component of the wave packet propagates into the forbidden region, having negative density.

I, describing in this way the intrinsic pair creation process (Figure 1.13b). As one may see, only particles in the energy regime $mc^2 < E < \phi_0 - mc^2$ are created. If now a particle, which energy is also in this regime, approaches the potential step from the left, the particles leaking out from the Dirac sea can no longer occupy this energy state, due to the Pauli principle. Therefore the appearance of the external particle suppresses the intrinsic pair creation process. This explains also, why more energetic particles have no influence at all. Although this explanation works fine for the Dirac theory it is unclear yet, how it translates to the Klein-Gordon theory where no Pauli principle exists. It is clear, that a supercritical potential step produces pairs independent of the spin of the particles involved. However, the question remains, how an incoming boson influences this production process. This is of course one of the next steps which have to be tackled.

It is worth to note, that equation (1.80) agrees with the numerically found propagation directions even for the case of the Klein paradox; a minus sign has to be introduced to take the negative energy into account. An example of this is given in Figure 1.14, where final results are shown for three different initial momenta $p = 0.333\,mc$, $p = 0.505\,mc$ and $p = 0.582\,mc$, corresponding to the angles $\theta = 20°$, $\theta = 40°$ and $\theta = 60°$, respectively.

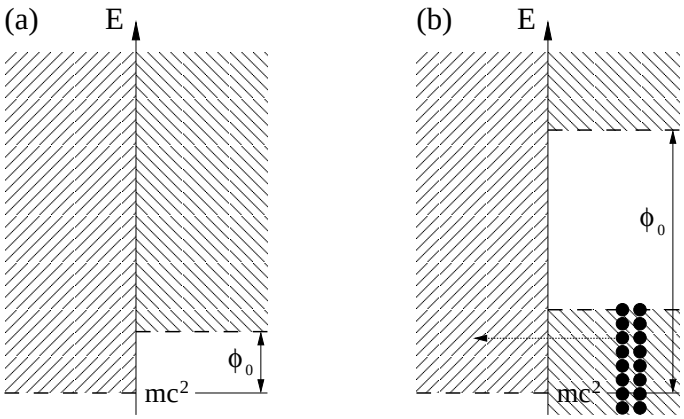

Figure 1.13: (a) Energy level scheme for a subcritical potential step. The shaded areas depict the free energy states. (b) For a supercritical potential step $\phi_0 > 2mc^2$, the field creates pairs out of the vacuum. Particles from the Dirac sea in region II (right) may leak out into region I (left), thus describing pair creation. The energy of the created pairs is bounded by $mc^2 \leq E \leq \phi_0 - mc^2$.

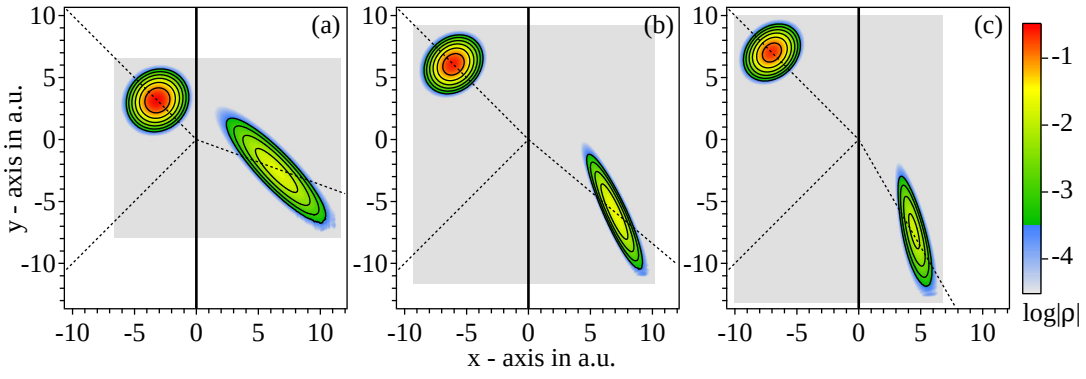

Figure 1.14: Klein paradox for different initial momenta, with $\phi_0 = 2.5mc^2$. A part of the wave function propagates into the normally forbidden region to the right along the direction predicted by equation (1.80). (a) $p = 0.333\,mc$, $\theta = 20°$; (b) $p = 0.505\,mc$, $\theta = 40°$; (c) $p = 0.582\,mc$, $\theta = 60°$.

1.6 The Dirac equation

The second main topic of this work was to investigate e^+e^- pair creation in counterpropagating laser fields. However, electrons are spin-$\frac{1}{2}$ particles and therefore not described properly by the Klein-Gordon equation. Therefore this section departs from the Klein-Gordon theory and introduces the Dirac equation,

$$i\hbar\frac{\partial\psi(x)}{\partial t} = \left[c\boldsymbol{\alpha}\left(\hat{\boldsymbol{p}} - \frac{q}{c}\boldsymbol{A}\right) + q\phi + mc^2\beta\right]\psi(x), \tag{1.82}$$

a relativistic wave equation describing fermions, discovered in 1928 by Dirac. It may be derived from the Lorentz group, enlarged by parity, as a connection between the fundamental $(\frac{1}{2},0)$ and $(0,\frac{1}{2})$ representations of the underlying $SU(2)\times SU(2)$ Lie algebra [76]. Here $\boldsymbol{\alpha}$ and β denote four-by-four matrices, which obey the following algebra

$$\{\alpha_i,\alpha_j\} = 2\delta_{ij}, \quad \{\alpha_i,\beta\} = 0, \quad \beta^2 = \mathbb{1}. \tag{1.83}$$

In the Dirac representation they are given by

$$\alpha_i = \begin{pmatrix} 0 & \sigma_i \\ \sigma_i & 0 \end{pmatrix} \quad \text{and} \quad \beta = \begin{pmatrix} \mathbb{1} & 0 \\ 0 & -\mathbb{1} \end{pmatrix}, \tag{1.84}$$

with the identity $\mathbb{1}$ and the Pauli matrices

$$\sigma_1 = \begin{pmatrix} 0 & 1 \\ 1 & 0 \end{pmatrix}, \quad \sigma_2 = \begin{pmatrix} 0 & -i \\ i & 0 \end{pmatrix}, \quad \sigma_3 = \begin{pmatrix} 1 & 0 \\ 0 & -1 \end{pmatrix}. \tag{1.85}$$

By introducing the four γ-matrices

$$\gamma^0 = \beta, \quad \gamma^i = \beta\alpha_i, \tag{1.86}$$

satisfying the Clifford algebra

$$\{\gamma^\mu,\gamma^\nu\} = 2g^{\mu\nu}, \tag{1.87}$$

the Dirac equation (1.82) may be written in a manifestly covariant form

$$\left[\gamma^\mu\left(\hat{p}_\mu - \frac{q}{c}A_\mu\right) - mc\right]\psi(x) = 0. \tag{1.88}$$

Like in the Klein-Gordon theory, the spectrum of solutions contains positive- and negative-energy states. The free solutions are given by

$$\psi^r_{\boldsymbol{p}} = \sqrt{\frac{E_{\boldsymbol{p}}+mc^2}{2VE_{\boldsymbol{p}}}}\begin{pmatrix} \varphi_r \\ \frac{c\boldsymbol{\sigma p}}{E_{\boldsymbol{p}}+mc^2}\varphi_r \end{pmatrix}\exp\left[-i\frac{p_\mu x^\mu}{\hbar}\right], \text{ for } r\in\{1,2\} \tag{1.89a}$$

$$\psi^r_{\boldsymbol{p}} = \sqrt{\frac{E_{\boldsymbol{p}}+mc^2}{2VE_{\boldsymbol{p}}}}\begin{pmatrix} \frac{c\boldsymbol{\sigma p}}{E_{\boldsymbol{p}}+mc^2}\varphi_r \\ \varphi_r \end{pmatrix}\exp\left[+i\frac{p_\mu x^\mu}{\hbar}\right], \text{ for } r\in\{3,4\}, \tag{1.89b}$$

with $\varphi_{1,3} = (1,0)^T$ and $\varphi_{2,4} = (0,1)^T$, specifying the two possible spin states, and $E_{\boldsymbol{p}} = c\sqrt{\boldsymbol{p}^2+m^2c^2}$ denoting the relativistic energy. The spinors (1.89a) with $r\in\{1,2\}$ represent particles (electrons) with positive energy, whereas the spinors (1.89b) with

$r \in \{3, 4\}$ represent particles with negative energy.

The Dirac equation (1.82) is already in a Hamiltonian form. Therefore, the split-operator method is directly applicable. The Hamiltonian can be split into

$$\begin{aligned} \hat{H}(x) &= c\boldsymbol{\alpha}\left(\hat{\boldsymbol{p}} - \frac{q}{c}\boldsymbol{A}(x)\right) + q\phi(x) + mc^2\beta && (1.90)\\ &= \left[-i\hbar c\boldsymbol{\alpha}\nabla + mc^2\beta\right] + \left[q\phi(x) - q\boldsymbol{\alpha}\boldsymbol{A}(x)\right] && (1.91)\\ &= \hat{K} + \hat{V}(x). && (1.92) \end{aligned}$$

Here the problem of mixing space dependent terms with spatial derivatives does not occur. Therefore arbitrary potentials may be examined. The numerical implementation follows the steps described in the Schrödinger theory in section 1.1. Here one cannot avoid the necessity of time consuming Fourier transformations as in the case of the Klein-Gordon equation. Details to the Dirac code (D++) utilized in our numerical calculations can be found in [55, 56].

Chapter 2

Electron-positron pair creation by counterpropagating laser fields

In the presence of very strong electromagnetic fields the quantum electrodynamic vacuum may become unstable and decay into e^+e^- pairs. The characteristic field strength for vacuum instability is the Schwinger field $E_c = m^2c^3/|e|\hbar = 1.3 \times 10^{16}\mathrm{V/cm}$ [1–3]. Due to the enormous progress in laser technology during recent years [10–12], the question arises wether this vacuum instability can be tested by laser fields. As a well known result, a single plane-wave laser field cannot extract pairs out of the vacuum, due to energy and momentum conservation. However, with the additional assistance of a Coulomb field [81–87] or a high energy γ-photon [88–91] the pair creation process becomes possible. Until now, pair creation by pure laser light has not been observed. The most simple field configuration for a realization of this pair creation process consists of two counterpropagating laser pulses of equal frequency and intensity [23, 24, 27–29, 31, 32, 34, 35, 47–49, 92–96].

This chapter is dedicated to the pair creation process in such a field configuration, with the vector potential

$$\begin{aligned} \boldsymbol{A} &= \frac{1}{2}A_0\left[\boldsymbol{e}_x\cos\omega(z+t)+\theta\boldsymbol{e}_y\sin\omega(z+t)\right]+\frac{1}{2}A_0\left[\boldsymbol{e}_x\cos\omega(z-t)-\theta\boldsymbol{e}_y\sin\omega(z-t)\right] \\ &= A_0\cos(\omega z)\left[\boldsymbol{e}_x\cos(\omega t)+\theta\boldsymbol{e}_y\sin(\omega t)\right] \\ &\approx A_0\left[\boldsymbol{e}_x\cos(\omega t)+\theta\boldsymbol{e}_y\sin(\omega t)\right]. \end{aligned} \tag{2.1}$$

Note that natural units ($\hbar = c = 1$) are employed throughout this chapter. The laser frequency is denoted by ω, the field strength is given by $E_0 = \omega A_0$ and the ellipticity parameter θ distinguishes between linear ($\theta = 0$) and circular ($\theta = 1$) polarization. In the last step of equation (2.1) the dipole-approximation was employed. Here the spatial dependence of the potential and thus the magnetic field is neglected, resulting in an oscillating electric field. This is justified when the characteristic length of the process (l_c) is less than the laser wave length λ: $l_c \ll \lambda$. In the pair creation process the characteristic length can be evaluated as a length on which the laser field imparts an electron with the characteristic energy $\varepsilon_c = m$: $l_c = \varepsilon_c/|e|E_0 = E_c/mE_0$, where in the last step the Schwinger field strength E_c has been employed. This leads to the condition $\omega \ll mE_0/E_c$, for which the dipole approximation is valid. The influence of the magnetic

field for high frequencies is investigated in the next chapter.

By introducing the relativistic laser parameter

$$\xi = \frac{|e|E_0}{m\omega}, \tag{2.2}$$

different interaction regimes of pair creation in laser fields may be distinguished [8]. For $\xi \ll 1$, the process probability follows a perturbative power law:

$$W \sim \xi^{2n}, \tag{2.3}$$

where n is the number of absorbed photons. While for $\xi \gg 1$, the probability shows a tunneling behavior:

$$W \sim \exp\left(-\pi \frac{E_c}{E_0}\right). \tag{2.4}$$

Because we are mostly interested in the intermediate regime, where no simple asymptotic formulas exist, we restrict the following discussions to $\xi = 1$ in almost all of our calculations.

The first section establishes the theoretical fundament, how numerical solutions of the Dirac equation can be utilized for the investigation of the pair production process. We present an intuitive approach based on the Dirac sea picture, and show that it is in accordance with a rigorous QED calculation for unstable vacuum in external fields. Before presenting the numerical results, the next chapter represents a detour employing a quasiclassical calculation. Here, the important notion of the quasi-energy of a particle in a periodic external field is introduced. The third section presents and compares numerical results, like transition probabilities and resonances, obtained from the Dirac and Klein-Gordon equation. Moreover, as explained in this section, it seems impossible to obtain the momentum distribution of the created electrons from these calculations. However, due to a numerical trick, presented in the fourth section, it is possible to run the code in a nonstandard mode, which enables us to obtain the momentum distributions in a single numerical propagation. For linear polarization, a remarkably good agreement is found with the results obtained from the quasiclassical calculation. However, for circular polarization the particular spin state of the electron becomes crucial. Therefore the final section describes a modification of the quasiclassical approach including the spin degree of freedom.

2.1 Theoretical fundament - from the Dirac sea to QFT

In the one-particle Dirac theory, pair creation is described as the transition of an electron from a negative-energy state out of the Dirac sea, into a positive-energy state, see section 1.5.4. Thereby, the hole which is left behind is interpreted as the created positron. In our calculations we employ an advanced computer code which solve the Dirac equation in an arbitrary external potential on a two dimensional grid. An initial free wave packet in the negative-energy continuum, representing an electron in the Dirac sea, is propagated via the split-operator algorithm. Under the influence of the external field an e^+e^- pair may be produced. The transition amplitude of this process is determined by

projection of the wave function onto positive-energy states after the external field has been turned off.
In this approach an intuitive graphical interpretation for the creation process is possible. As an example, Figure 2.1 shows the time evolution of an initially negative-energy Gaussian wave packet at rest under the influence of an oscillating electric field. When the e^+e^- pair is produced, a droplet is separated from the wave packet which moves opposite to the initial one. The droplet is a positive-energy state and represents the created electron. The change of the sign of energy is evidenced by the change of the droplet group velocity.

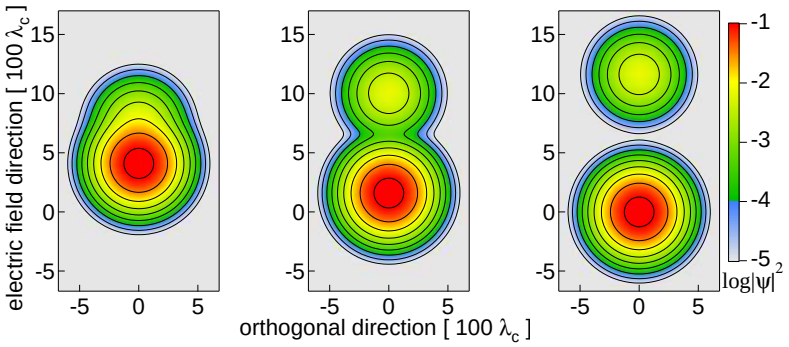

(a) $t = 800\ m^{-1}$ (b) $t = 1050\ m^{-1}$ (c) $t = 1300\ m^{-1}$

Figure 2.1: Pair creation in an oscillating electric field with $\omega = m/200$ and the critical Schwinger field strength $E_0 = E_c = m^2/|e|$. Three snapshots of the probability distribution are taken at times as indicated from the evolution of an initially negative-energy Gaussian wave packet at rest at the origin. The length is scaled in multiples of the Compton wave length $\lambda_C = 1/m$.

This intuitive picture based on the framework of the one-particle time-dependent Dirac equation finds its rigorous foundation in the well-established revised version of Furry's formulation of QED in external fields with unstable vacuum [54, 77], outlined now.

The Dirac Hamiltonian (1.82) is given by

$$\mathcal{H} = \boldsymbol{\alpha}\left(-i\nabla - q\boldsymbol{A}(x)\right) + q\phi + m\beta. \tag{2.5}$$

We assume that the potentials are nonzero only during a finite time interval, and thus vanishing in the remote past $t \to -\infty$ and in the distant future $t \to \infty$. Therefore one obtains two complete and orthonormal sets of solutions $\{{}_{(\pm)}\varphi_p\}$ and $\{{}^{(\pm)}\varphi_p\}$, of the Dirac equation

$$\left[i\frac{\partial}{\partial t} - \mathcal{H}\right]\varphi_p(x) = 0, \tag{2.6}$$

where p denotes a generalized index, e.g., the momentum of the particle. The difference between these sets, lies in the asymptotic limit for $t \to \pm\infty$. The basis $\{{}_{(\pm)}\varphi_p\}$ corresponds to free positive- and negative-energy solutions in the remote past $(t \to -\infty)$, whereas the basis $\{{}^{(\pm)}\varphi_p\}$ corresponds to free positive- and negative-energy solutions in

the distant future ($t \to \infty$). The Heisenberg field operator can be decomposed in these basis sets as

$$\hat{\psi}(x) = \sum_p \hat{a}_p(\text{in})\,{}_{(+)}\varphi_p(x) + \hat{b}_p^\dagger(\text{in})\,{}_{(-)}\varphi_p(x), \tag{2.7}$$

$$= \sum_p \hat{a}_p(\text{out})\,{}^{(+)}\varphi_p(x) + \hat{b}_p^\dagger(\text{out})\,{}^{(-)}\varphi_p(x). \tag{2.8}$$

Note, that the time dependence of the creation and annihilation operators is not shown explicitly. The equal-time anticommutation relations follow from the equal-time anticommutation relations of the field operator, and are given for the IN operators by

$$\{\hat{a}_p(\text{in}), \hat{a}_{p'}^\dagger(\text{in})\} = \{\hat{b}_p(\text{in}), \hat{b}_{p'}^\dagger(\text{in})\} = \delta_{pp'}, \tag{2.9}$$

with all other equal-time anticommutators equal to zero. The same relations follow for the OUT operators:

$$\{\hat{a}_p(\text{out}), \hat{a}_{p'}^\dagger(\text{out})\} = \{\hat{b}_p(\text{out}), \hat{b}_{p'}^\dagger(\text{out})\} = \delta_{pp'}, \tag{2.10}$$

where again all other equal-time anticommutators are equal to zero.

The IN creation and annihilation operators define the vacuum state in the remote past via

$$\hat{a}_p(\text{in})\,|0, \text{in}\rangle = 0, \quad \hat{b}_p(\text{in})\,|0, \text{in}\rangle = 0, \tag{2.11}$$

whereas the OUT creation and annihilation operators define the vacuum state in the distant future via

$$\hat{a}_p(\text{out})\,|0, \text{out}\rangle = 0, \quad \hat{b}_p(\text{out})\,|0, \text{out}\rangle = 0. \tag{2.12}$$

The IN- and OUT-vacua may differ from each other. So if the vacuum-to-vacuum amplitude is not equal to unity, $\langle 0, \text{out}|\, 0, \text{in}\rangle \neq 1$, the vacuum is unstable under the influence of the external field, meaning that pairs are created from the vacuum.
To find the amount of electrons and positrons produced, one has to find a connection between the IN and OUT creation and annihilation operators. Therefore, the next step is to introduce the Dirac propagator in external fields, defined through

$$\left[i\frac{\partial}{\partial t} - \mathcal{H}\right] G(x, y) = 0, \tag{2.13}$$

with the initial condition

$$G(x, y)\Big|_{x^0 = y^0} = \delta(\boldsymbol{x} - \boldsymbol{y}). \tag{2.14}$$

It satisfies the following relations:

$$\int d^3x'\, G(x, x')G(x', y) = G(x, y) \tag{2.15}$$

$$G^\dagger(x, y) = G(y, x) \tag{2.16}$$

$$G(x, y) = \sum_p \varphi_p(x)\varphi_p^\dagger(y) \tag{2.17}$$

The propagator relates the solutions of the Dirac equation, and thus the spinor field operators, at different spatiotemporal points according to

$$\hat{\psi}(x) = \int d^3y\, G(x,y)\hat{\psi}(y). \tag{2.18}$$

We are now able to find the connection between the IN and OUT creation and annihilation operators.

$$\begin{aligned}\int d^3x\, {}^{(+)}\varphi_p^\dagger(x)\hat{\psi}(x) &= \sum_{p'} \hat{a}_{p'}(\text{out}) \underbrace{\int d^3x\, {}^{(+)}\varphi_p^\dagger(x)\, {}^{(+)}\varphi_{p'}(x)}_{=\delta_{pp'}} + \hat{b}_{p'}^\dagger(\text{out}) \underbrace{\int d^3x\, {}^{(+)}\varphi_p^\dagger(x)\, {}^{(-)}\varphi_{p'}(x)}_{=0} \\ &= \hat{a}_p(\text{out}). \end{aligned} \tag{2.19}$$

Simultaneously one finds

$$\begin{aligned}\int d^3x\, {}^{(+)}\varphi_p^\dagger(x)\hat{\psi}(x) &= \int d^3x\, d^3x'\, {}^{(+)}\varphi_p^\dagger(x) G(x,x')\hat{\psi}(x') \qquad (2.20)\\ &= \int d^3x\, d^3x'\, {}^{(+)}\varphi_p^\dagger(x) G(x,x') \sum_{p'} \left(\hat{a}_{p'}(\text{in})\, {}_{(+)}\varphi_{p'}(x') + \hat{b}_{p'}^\dagger(\text{in})\, {}_{(-)}\varphi_{p'}(x') \right) \\ &= \sum_{p'} \left(\int d^3x\, d^3x'\, {}^{(+)}\varphi_p^\dagger(x) G(x,x')\, {}_{(+)}\varphi_{p'}(x') \right) \hat{a}_{p'}(\text{in}) \\ &\quad + \sum_{p'} \left(\int d^3x\, d^3x'\, {}^{(+)}\varphi_p^\dagger(x) G(x,x')\, {}_{(-)}\varphi_{p'}(x') \right) \hat{b}_{p'}^\dagger(\text{in}) \\ &= \sum_{p'} G_{pp'}({}^+|_+)\hat{a}_{p'}(\text{in}) + G_{pp'}({}^+|_-)\hat{b}_{p'}^\dagger(\text{in}). \end{aligned}$$

This may be written in matrix notation as

$$\hat{a}(\text{out}) = G({}^+|_+)\hat{a}(\text{in}) + G({}^+|_-)\hat{b}^\dagger(\text{in}), \tag{2.21}$$

$$\hat{b}(\text{out}) = \hat{a}^\dagger(\text{in})G({}_+|^-) + \hat{b}(\text{in})G({}_-|^-), \tag{2.22}$$

$$\hat{a}(\text{in}) = G({}_+|^+)\hat{a}(\text{out}) + G({}_+|^-)\hat{b}^\dagger(\text{out}), \tag{2.23}$$

$$\hat{b}(\text{in}) = \hat{a}^\dagger(\text{out})G({}^+|_-) + \hat{b}(\text{out})G({}^-|_-). \tag{2.24}$$

The last three relations, stated for completeness, are obtained in the same way as the first one.

Starting from an initial vacuum, the external field may create e^+e^- pairs. The mean number of the created electrons with momentum p is given by

$$\begin{aligned} n_p &= \langle 0, in|\, \hat{a}_p^\dagger(\text{out})\hat{a}_p(\text{out})\, |0, in\rangle \qquad (2.25)\\ &= \sum_{p'} \left| G_{pp'}({}^+|_-) \right|^2. \end{aligned}$$

Evidently, the mean number of created positrons is equal to the mean number of created electrons. The sum of equation (2.25) over all states p gives the total number of created electrons, and thus of created pairs

$$n = \sum_{p\,p'} \left| G_{pp'}({}^{+}|{}_{-}) \right|^2 . \tag{2.26}$$

This final result yields now the connection to the Dirac sea approach, because the quantity

$$\begin{aligned} G_{pp'}({}^{+}|{}_{-}) &= \lim_{t\to\infty} \lim_{t'\to-\infty} \int d^3x\, d^3x'\, {}^{(+)}\varphi_p^\dagger(x) G(x,x')\, {}_{(-)}\varphi_{p'}(x') && (2.27)\\ &= \lim_{t\to\infty} \int d^3x\, {}^{(+)}\varphi_p^\dagger(x)\psi(x), && (2.28) \end{aligned}$$

coincides with the projection of the exact solution $\psi(x)$ of the time-dependent Dirac equation, which evolves from an initial negative-energy state, onto a final free positive-energy solution ${}^{(+)}\varphi_p(x)$. Our numerical approach, outlined at the beginning, utilizes the result of this rigorous second-quantized QED calculation in external fields. At this step, no approximation is employed, apart from the well-justified assumption that the given external field is not substantially modified due to the interaction.

2.2 Quasiclassical approach

To gain a qualitative understanding of the e^+e^- pair creation process, we first apply a quasiclassical method, in which the phase of the Dirac wave function is approximately given by the classical action, satisfying the Hamilton-Jacobi equation [58, 78, 79],

$$\psi_\pm(t,\boldsymbol{r}) \sim \exp\left(iS_\pm(t,\boldsymbol{r})\right). \tag{2.29}$$

The $(\pm)$ sign takes the two possible signs of energy into account. This quasiclassical description is valid if the conditions

$$\omega \ll m \quad \text{and} \quad E_0 \ll E_c \tag{2.30}$$

are fulfilled. These stem from the two requirements, that the Compton wavelength has to be smaller than the characteristic length of the process (l_c): $\lambda_C \ll l_c$, and that the photon energy has to be less than the characteristic energy of the process (ε_c): $\omega \ll \varepsilon_c$. The characteristic energy of the pair creation process is given by the mass of the electron: $\varepsilon_c = m$, and the characteristic length may be obtained as the length along which the laser field (E_0) imparts an electron with the characteristic energy: $l_c = \varepsilon_c/|e|E_0$. By taking the Schwinger field $E_c = \varepsilon_c/\lambda_C|e|$ into account, this leads to the conditions of equation (2.30).

The Hamilton-Jacobi equation is given by

$$H(\boldsymbol{r}, \nabla S(t,\boldsymbol{r}), t) + \frac{\partial S(t,\boldsymbol{r})}{\partial t} = 0, \tag{2.31}$$

where the classical relativistic Hamiltonian reads

$$H(\boldsymbol{r},\boldsymbol{q},t) = H(\boldsymbol{q},t) = \pm\sqrt{m^2 + (\boldsymbol{q} - e\boldsymbol{A}(t))^2}. \tag{2.32}$$

We introduced here the possibility of positive and negative energies explicitly. Because we employ the dipole approximation, the vector potential and therefore the Hamiltonian does not depend on the spatial coordinate. In fact, the vector potential $\boldsymbol{A}$ is only a function of the phase $\eta = \omega t$. An ansatz for the action S, fulfilling the Hamilton-Jacobi equation (2.31), is given by

$$\begin{aligned} S_\pm &= \boldsymbol{qr} \mp S_0(\eta) \\ &= \boldsymbol{qr} \mp \frac{1}{\omega}\int_{\eta_0}^{\eta} d\eta' \sqrt{m^2 + (\boldsymbol{q} - e\boldsymbol{A}(\eta'))^2}. \end{aligned} \tag{2.33}$$

It separates into a spatial and a time dependent part $S_0(\eta)$. Due to the periodicity of the vector potential $\boldsymbol{A}(\eta + 2\pi) = \boldsymbol{A}(\eta)$, the time dependent portion may be split further into a linear and a periodic part.
In order to see this, let $f(\eta)$ be a 2π-periodic function. Then the function

$$F(\eta) = \frac{\eta}{2\pi}\int_0^{2\pi} d\eta'\, f(\eta') - \int_{\eta_0}^{\eta} d\eta'\, f(\eta') \tag{2.34}$$

is also 2π-periodic:

$$\begin{aligned} F(\eta + 2\pi) &= \frac{\eta}{2\pi}\int_0^{2\pi} d\eta'\, f(\eta') + \int_0^{2\pi} d\eta'\, f(\eta') - \int_{\eta_0}^{\eta} d\eta'\, f(\eta') - \int_{\eta}^{\eta+2\pi} d\eta'\, f(\eta') \\ &= F(\eta), \end{aligned} \tag{2.35}$$

as the second and forth term on the right hand side cancel each other. Applying this to the time dependent part of the action S_0 ,we may rewrite (2.33) as

$$S_\pm = \boldsymbol{qr} \mp q_0 t \pm S_p(\eta). \tag{2.36}$$

Introducing in this way the quasi-energy q_0, which is just the instantaneous energy (2.32) averaged over a field oscillation.

$$q_0 = \frac{\omega}{2\pi}\int_0^{2\pi} d\eta\, \frac{\partial S}{\partial \eta} = \frac{1}{2\pi}\int_0^{2\pi} d\eta\, \sqrt{m^2 + (\boldsymbol{q} - e\boldsymbol{A}(\eta))^2} \tag{2.37}$$

Therefore the time dependent portion of the action separates into a quasi-energy part, which is linear in time, and a 2π-periodic part S_p.

Due to the pure time dependence of the external potential, the momentum is conserved. Therefore only transitions between negative- and positive-energy states with the same momentum are permitted in the pair creation process. According to this, the transition amplitude is given by

$$\psi_-^\dagger \psi_+ \sim \exp\big(2i\,(S_p(\eta) - q_0 t)\,\big). \tag{2.38}$$

Now we can employ the fact, that S_p is 2π-periodic and expand the equation (2.38) into a Fourier series

$$\psi_-^\dagger \psi_+ \sim \sum_{n=-\infty}^{\infty} \mathcal{C}_n \exp\big(i\,(n\omega - 2q_0)\,t\big). \tag{2.39}$$

Here $\mathcal{C}_n$ denote the Fourier coefficients from the expansion. The index n has a physical meaning, it indicates the number of photons involved in the process. In an exact treatment, this amplitude would be time independent, leading in our case to the energy conservation condition

$$n_0\omega = 2q_0. \tag{2.40}$$

So, n_0 photons are required to overcome the energy gap of $2q_0$. One should note that the laser-dressed energy enters here instead of the free energy. The other summands in equation (2.39), not fulfilling the resonance condition (2.40), are oscillatorily damped.

The Fourier coefficients

$$\mathcal{C}_n = \frac{1}{2\pi}\int_0^{2\pi} d\eta \, \exp\left(i\left(2S_p(\eta) - n\eta\right)\right) \tag{2.41}$$

are related to the probability of the pair creation process involving n-photons

$$W_n \sim |\mathcal{C}_n|^2. \tag{2.42}$$

As a first example, we chose a rather large frequency of $\omega = 0.49072m$ and $\xi = 1$ in order to compare these results with the one obtained by the Dirac code in the next section. Although these parameters lie at the boundary of the region of validity (see equation (2.30)), the resemblance to results obtained in later sections is remarkably well. The scaled quasi-energy $2q_0/\omega$ is shown in Figure 2.2 for linear polarization (blue line) and circular polarization (red line). At the momenta, where it coincides with an integer (drawn as black lines), the resonance condition (2.40) is fulfilled. These momenta will show up as resonances in the momentum spectrum of the created electrons. The reason why the quasi-energy for circular polarization is larger than for linear polarization is the fixed value of ξ, which we set in both cases equal to one. Therefore, the particle encounters a larger effective field in the circular case than in the linear one, resulting in a larger quasi-energy. Figure 2.3 shows the magnitude squared of the Fourier coefficients belonging to these resonant momenta. As stated by equation (2.42), the probability for the multiphoton process of pair creation is essentially determined by these functions. The dashed lines have been inserted to guide the eye and have no physical meaning.

As a second example we decrease the frequency to $\omega = 0.2m$, keeping $\xi = 1$. The results are shown in Figure 2.4 and Figure 2.5. One should note, that the maximum of the probability for linear polarization appears always at the minimal resonant momentum, whereas the maximum for circular polarization is shifted to higher resonant momentum values. This feature is similar to the one encountered in above-threshold ionization of atoms [97]. In both cases, the electron driven by a strong oscillatory electromagnetic field has to travel through a classically forbidden region to reach the continuum. The momentum of the electron after the tunneling is determined by the value of the vector potential. the maximal tunneling probability occurs at maximal field strength. For a linear polarized laser, this happens when the vector potential vanishes, leading therefore to a vanishing electron momentum. On the other hand, for circular polarized lasers the magnitude of the field and the vector potential is constant, leading to a nonzero momentum of the electron.

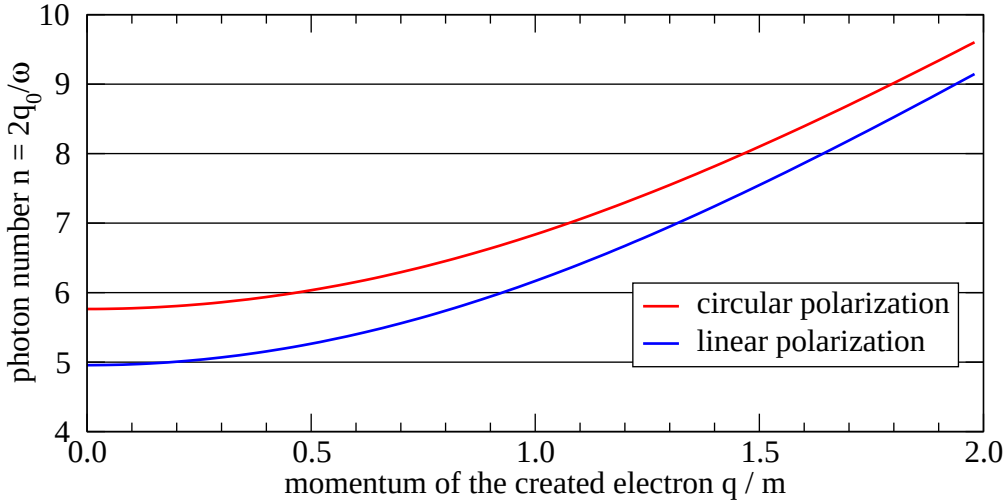

Figure 2.2: Shown is the scaled quasi-energy $2q_0/\omega$ versus the momentum of the created electron for circular and linear laser polarization with a laser frequency of $\omega = 0.49072m$ and $\xi = 1$. The crossings with the black integer lines denote the momenta which fulfill the resonance condition (2.40). At these momenta an n-photon resonance occur in the momentum distribution of the created electron.

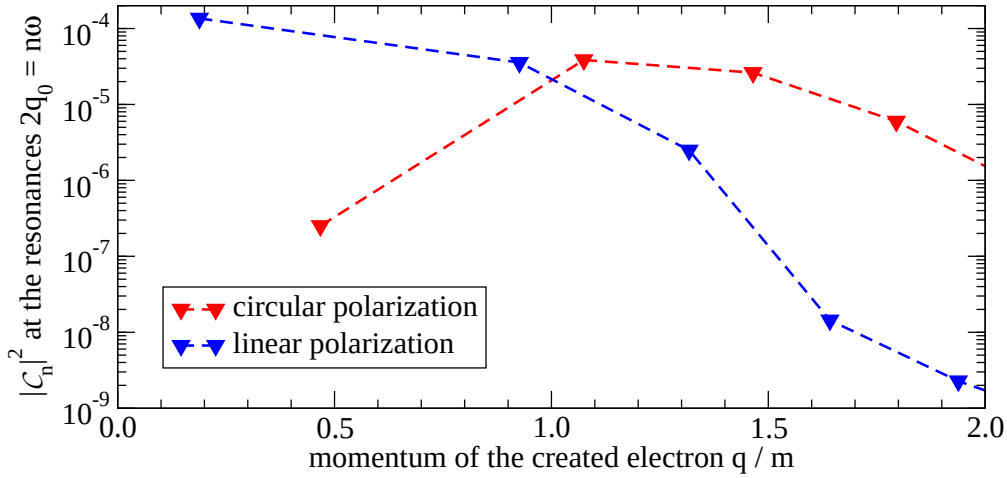

Figure 2.3: The triangles show the magnitude of the Fourier coefficients squared at the resonant momenta, proportional to the creation probability. The dashed lines have been drawn to guide the eye and have no physical meaning.

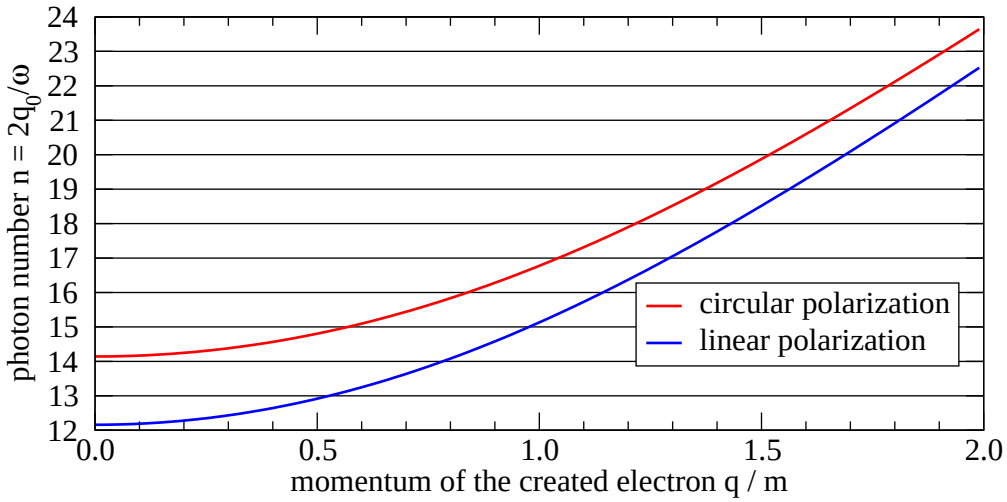

Figure 2.4: Shown is the scaled quasi-energy $2q_0/\omega$ versus the momentum of the created electron for circular and linear laser polarization, similar to Figure 2.2, with a decreased laser frequency $\omega = 0.2m$ and $\xi = 1$. The crossings with the black integer lines denote the momenta which fulfill the resonance condition (2.40). At these momenta an n-photon resonance occur in the momentum distribution of the created electron.

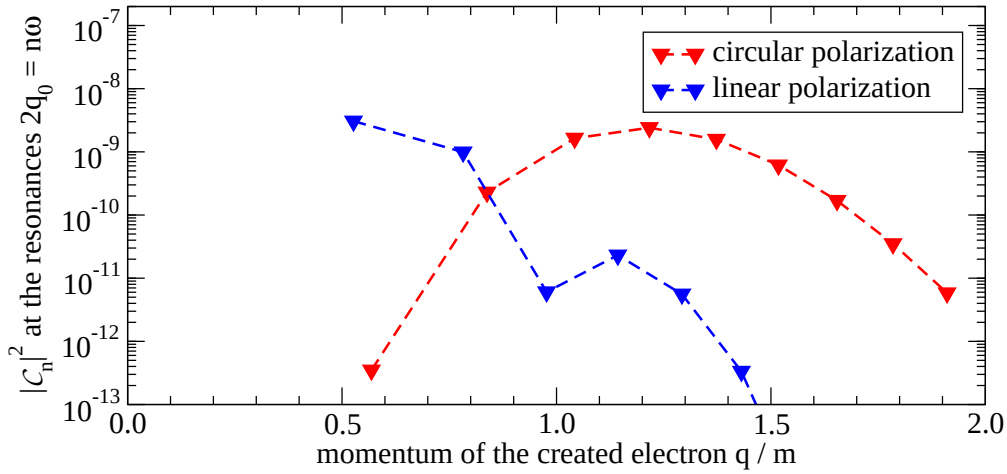

Figure 2.5: The magnitude of the Fourier coefficients squared at the resonant momenta, proportional to the creation probability. The dashed lines drawn are to guide the eye and have no physical meaning.

The shown results have been obtained by numerical integration of equations (2.37) and (2.41). For much lower frequency values, the numerical integration becomes more involved, because of accumulating roundoff errors. However, it is possible to apply the saddle point approximation, and thus to obtain the scaling behavior of the creation probability in the multiphoton regime [80]. It can be shown, that in the strong field limit $\xi \gg 1$ the probability at the maximal contributing resonance scales in accordance to the known tunneling behavior [8, 80]:

$$W \sim \exp\left(-\pi \frac{E_c}{E_0}\right). \tag{2.43}$$

In the weak field limit where $\xi \ll 1$, the probability shows a perturbative power law dependence [8, 80]:

$$W \sim \xi^{2n_0}. \tag{2.44}$$

For the intermediate regime $\xi = 1$, the probability exhibits an exponential behavior [80]:

$$W \sim \exp\left(-\alpha \frac{E_c}{E_0}\right), \tag{2.45}$$

with $\alpha \approx 3$, in close similarity to equation (2.43).

2.3 Numerical results on the pair creation process

The starting point of our numerical calculations, as explained in section 2.1, is a free negative-energy Gaussian wave packet with initial momentum $\boldsymbol{p}_i$, representing an electron in the Dirac sea. The width of the wave packet in momentum space is taken to be $\Delta p \approx m\alpha$, with the fine structure constant α. It is chosen sufficiently narrow to closely approximate a momentum eigen-state. The wave packet is propagated in time under the influence of the external field (2.1). If the field is sufficiently strong, an e^+e^- pair can be produced. The transition amplitude is determined by projection of the wave function onto all positive-energy states after the external field has been switched off. In the numerical implementation the potential (2.1) is modified by a pulse shape function consisting of a $\sin^2$ turn-on, followed by a plateau region and a final $\sin^2$ turn-off. In order to examine the influence of the pulse length onto the process, the duration of the plateau region is variable whereas the fixed turn-on and turn-off last half a cycle each. The ellipticity parameter θ is set to zero, so only linearly polarized laser light is investigated in this section. In addition, the relativistic laser parameter is fixed to $\xi = 1$. We examine the outcome of both the Dirac and Klein-Gordon equation, where the second case treats spinless boson pair creation. We will find fundamental differences due to the underlying spin statistics. For the Dirac case, the spin is always chosen perpendicular to the x-y-plane of interaction.

The first observation is connected to the dipole approximation employed. Due to the pure time dependence of the vector potential, the problem is translational invariant, which leads to the conservation of momentum. Therefore only transitions from a negative-energy state with momentum p into a positive-energy state with the same momentum p are allowed. This reduces the problem essentially to a two level system, where the

two states are coupled via the external oscillating electric field. As a well known result, such a system under resonant driving undergoes Rabi oscillations [98], which are also discovered in the pair creation process [27–29, 31, 32]. Figure 2.6 shows the dependence of the creation probability on the pulse duration for three different frequencies. Here and in the following results, we set the initial momentum $p_i = 0$, and thus restrict ourselves to the transition with the smallest energy gap. We return to nonzero initial momenta at the end of this section, leading us to a modified numerical approach introduced in the next section.

The creation probability in Figure 2.6 shows a characteristic oscillating behavior, where the amplitude depends on the laser frequency. At $\omega = 0.49072m$, a resonance occurs in correspondence to the multiphoton resonance condition (2.40). The quasienergy (2.37) entering the resonance condition is analytically computable and equates to $q_0(0) \approx 1.21m$. So the maximal frequency shown, corresponds to an $n = 5$ photon resonance named ω_5. The numerically obtained value of $\omega_5 = 0.49072m$ differs slightly from the analytical one, given by $\omega_5' = 2q_0(0)/5 = 0.484m$, as a result of the finite pulse length not incorporated in the analytical calculation. Taking for each frequency the maximum of the creation probability as a function of the laser pulse duration, one arrives at the spectrum given in Figure 2.7. This way, the normally superimposed pulse length dependent oscillations of the probability are omitted, and the resonances are clearly visible.

Note that the even-n resonances are suppressed. For zero momentum, the final e^+e^- state is odd under charge-conjugation [99]. This can only be achieved by the absorption of an odd number of photons so that even-n resonances are forbidden in this case. However, the Gaussian wave packet employed comprises nonzero momentum components for which the charge conjugation argument does not hold, and thus lead to suppressed resonances.

We turn now from the Dirac equation to the Klein-Gordon equation, starting with the same initial negative-energy state and propagate it under the influence of the oscillating electric field. After the interaction we project onto all positive-energy states and integrate over their contributions. If we would have a single momentum state instead of a Gaussian momentum distribution, this integration would be unnecessary. The pulse length dependent result of this projection is shown in Figure 2.8 for different frequencies. Note that it is plotted on a logarithmic scale. The highest frequency given corresponds again to a resonance. For off-resonant frequencies it shows an oscillating behavior similarly as in the Dirac case. However, for near-resonant frequencies it becomes exponentially growing. This is directly related to the bosonic character of the particle. Fermionic particles coming out of the vacuum are not allowed to fill already occupied states, due to the Pauli exclusion principle. Therefore the occupation number of a particular state cannot exceed unity. However, no such restriction holds for bosonic particles, and the occupation number is not limited.

Taking the maximum of the projection for different frequencies yields the resonance spectrum Figure 2.9. Due to the parallelization of the Klein-Gordon code, the limitation on the examined frequency range is much lower compared to the one given by the Dirac code. However there would be no further physical insight for smaller frequencies.

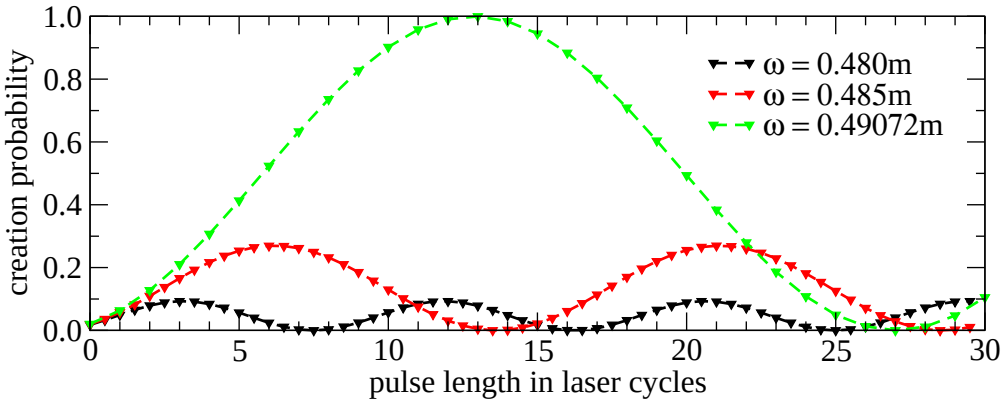

Figure 2.6: Pair creation probability versus pulse length in the Dirac theory for three different frequencies and $\xi = 1$. The considered initial electron momentum was taken to be $p_i = 0$. The highest frequency shown by the green triangles corresponds to a 5-photon resonance and exhibits the characteristic Rabi oscillation pattern.

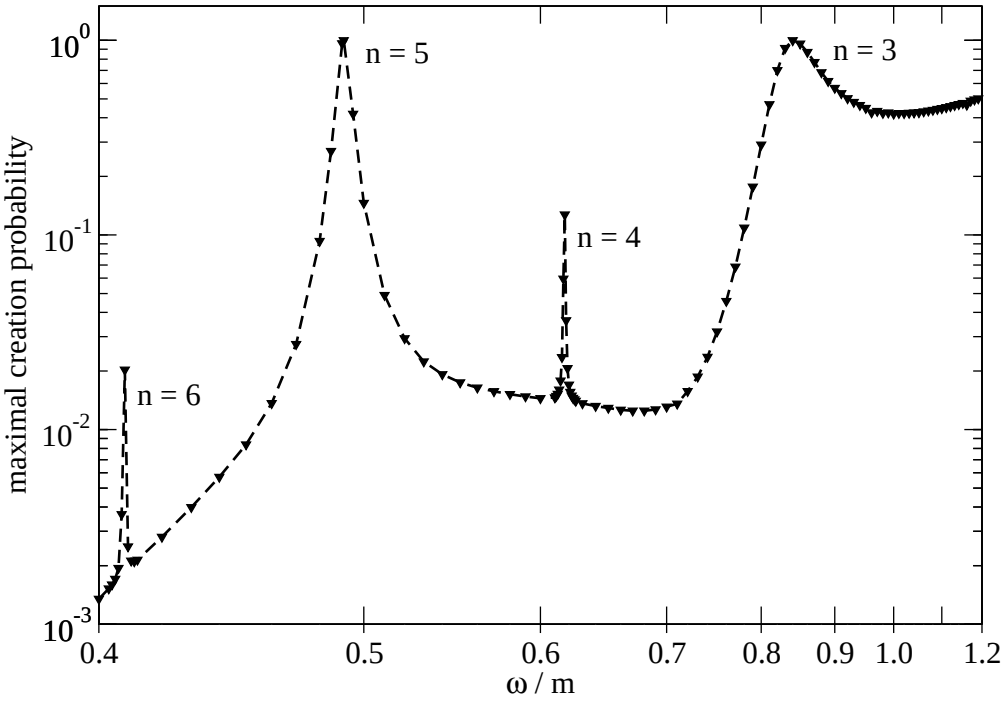

Figure 2.7: Resonant probability spectrum in the Dirac theory: Maximal value of the pair creation probability during Rabi oscillations at $\xi = 1$, varying the pulse length up to 200 cycles. The peak labels denote the absorbed photon number. The frequency is plotted reciprocally so the distance between the resonances is constant (2.40). The applied Dirac code gives a limitation on the smallest frequency examined in the simulations, due to the enormous computational time consumption. We therefore restrict the frequency range to $\omega \geq 0.4m$.

Therefore we restricted the calculations to $\omega \geq 0.2m$. Because there is no upper bound for the occupation number, we limited the pulse length to twenty cycles. Compared to the fermionic case, the pattern of pronounced and suppressed resonances is reversed. The reason is, that for vanishing momentum the final bosonic state is even under charge conjugation, which can only be achieved by absorption of an even number of photons.

In the calculations above, we have focused on a single electron with vanishing initial momentum. The question arises how one may obtain the momentum distribution of the produced electrons or even total rates out of these calculations. Applying the one-particle approach would be quite tedious, because it would require a propagation for every initial momentum. However, due to the momentum conservation one can employ a mathematical trick which yields the entire momentum distribution in a single numerical propagation. This trick is presented in the next section, along with the resulting momentum distributions.

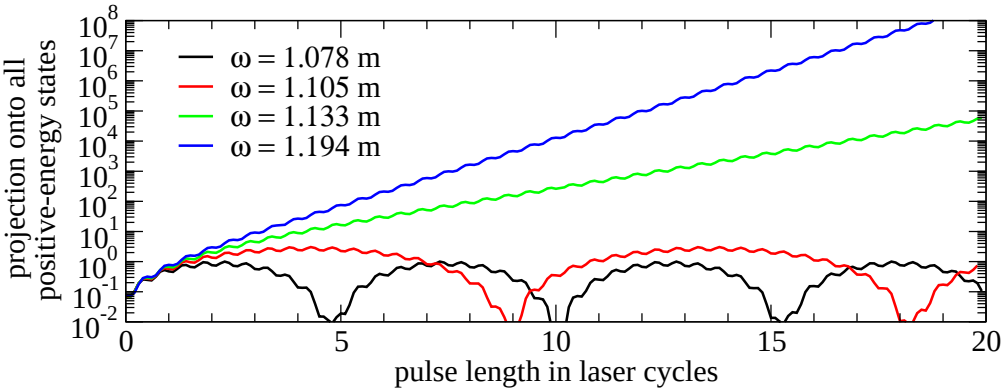

Figure 2.8: Projection onto positive-energy states versus pulse length in the Klein-Gordon theory for four different frequencies and $\xi = 1$ on a logarithmic scale. The initial electron momentum was taken to be $p_i = 0$. For off-resonant frequencies an oscillating pattern was found, whereas reaching a resonance it becomes exponentially growing. The highest frequency shown by the blue curve corresponds to a 2-photon resonance.

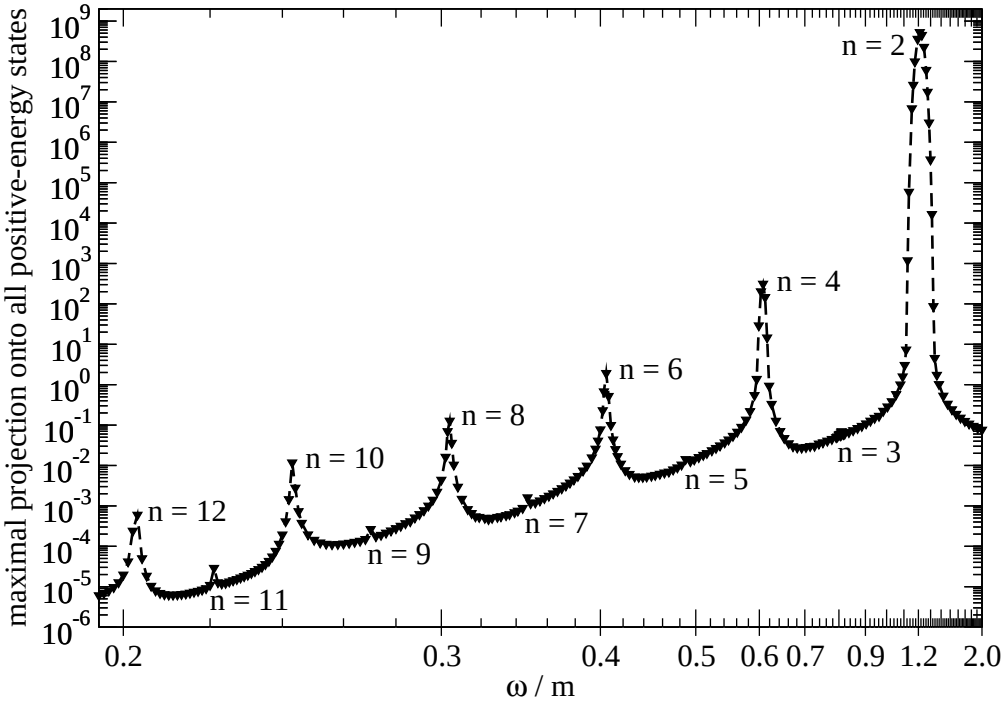

Figure 2.9: Resonant spectrum in the Klein-Gordon theory: Maximal value of the projection at $\xi = 1$, varying the pulse length up to 20 cycles. The peak labels denote the required photon number to overcome the energy gap. The frequency is plotted reciprocally so the distance between the resonances is constant (2.40).

2.4 Momentum distribution and total creation probability

The calculations presented in this section are for fermions and thus based on the Dirac theory. In order to obtain the presented results for the Klein-Gordon theory, one has to follow the same steps, neglecting the spin degree of freedom whenever it occurs. One of the final goals is to obtain the momentum distribution of the created pairs. With the numerical method employed so far, this is in principle possible but tedious, since each propagation yields only a single point of the (p_x, p_y) momentum distribution. Therefore we employ a different approach, which allows the inclusion of all particle momenta in a single calculation due to the purely time-dependent nature of the external field. In order to see this, we first consider the general expression for the momentum distribution

$$\sum_{r=3}^{4} \int \frac{V d^3p}{(2\pi)^3} \left| \left\langle \phi_{\boldsymbol{p}'}^{r'} \middle| \psi_{\boldsymbol{p}}^{r} \right\rangle \right|^2, \tag{2.46}$$

where $\phi_{\boldsymbol{p}'}^{r'}$ are the free positive-energy ($r' \in \{1, 2\}$) solutions (1.89) of the Dirac equation with momentum $\boldsymbol{p}'$, and $\psi_{\boldsymbol{p}}^{r}$ is the propagated state initially given by an electron with negative energy and momentum $\boldsymbol{p}$, i.e. $\psi_{\boldsymbol{p}}^{r}(t < 0) = \phi_{\boldsymbol{p}}^{r}$, with $r \in \{3, 4\}$. We assume, that the external field acts on the vacuum only during a finite time range between $t = 0$ and $t = T$. Here T denotes the interaction time, which is equal to the pulse duration.

A special feature of the linear polarization case, is the symmetry of the potential. The system is invariant under rotations around the polarization axis, which we chose to be the y-axis. The dynamics of an electron therefore stays in the plane containing this axis and the direction of the initial momentum. By virtue of this rotational symmetry, the matrix element in expression (2.46) is also rotationally invariant about the field axis. It is therefore possible to choose a system of coordinates such that the momentum of the electron is given by $\boldsymbol{p}_1 = (p_x, p_y, 0)$. This will enable us, to obtain 3-dimensional total probabilities per volume from our 2-dimensional simulations. For the circular case, no such symmetry exists. In order to keep the dynamics 2-dimensional here, we have to restrict the direction of the initial momentum to the plane spanned by the rotating field vector, corresponding to the x-y-plane. In either case, we may introduce a spin-like operator

$$\tilde{\Sigma} = -i\beta\alpha_1\alpha_2 = \begin{pmatrix} \sigma_3 & 0 \\ 0 & -\sigma_3 \end{pmatrix}, \tag{2.47}$$

which commutes with the Hamiltonian, and is thus conserved. Therefore, an initial negative-energy spin state couples only to one, out of the two possible positive-energy spin states, i.e., the spin state $r = 3$ couples to $r = 2$ and the spin state $r = 4$ couples to $r = 1$. As always assumed, the spin lies along the axis perpendicular to the computational plane (along the z-axis).

Starting from an initially free negative-energy momentum eigen-state

$$\psi_{\boldsymbol{p}}^{r}(t < 0) = \phi_{\boldsymbol{p}}^{r}, \tag{2.48}$$

and taking the spin flipping and the momentum conservation into account, the final state after the interaction is of the form

$$\psi_{\boldsymbol{p}}^{r}(t > T) = c_1(\boldsymbol{p}, r)\phi_{\boldsymbol{p}}^{5-r} + c_2(\boldsymbol{p}, r)\phi_{\boldsymbol{p}}^{r}, \tag{2.49}$$

where T denotes the interaction time. Inserting this into expression (2.46) yields

$$\begin{aligned}\sum_{r=3}^{4}\int\frac{Vd^3p}{(2\pi)^3}\left|\left\langle\phi_{\boldsymbol{p}'}^{r'}\middle|\,\psi_{\boldsymbol{p}}^{r}\right\rangle\right|^2 &= \sum_{r=3}^{4}\int\frac{Vd^3p}{(2\pi)^3}\left|c_1(\boldsymbol{p},r)\frac{(2\pi)^3}{V}\delta_{r',5-r}\delta(\boldsymbol{p}'-\boldsymbol{p})\right|^2\\ &= \sum_{r=3}^{4}\int d^3p\,|c_1(\boldsymbol{p},r)|^2\,\delta_{r',5-r}\delta(\boldsymbol{p}'-\boldsymbol{p})\\ &= \left|c_1(\boldsymbol{p}',5-r')\right|^2. \end{aligned}\tag{2.50}$$

Here we employed the following normalization condition, satisfied by the free solutions (1.89) of the Dirac equation:

$$\left\langle\phi_{\boldsymbol{p}'}^{r'}\middle|\,\phi_{\boldsymbol{p}}^{r}\right\rangle = \frac{(2\pi)^3}{V}\delta_{r'r}\,\delta(\boldsymbol{p}'-\boldsymbol{p}),\tag{2.51}$$

where V denotes a normalization volume. Moreover, we utilized the relation

$$\delta(\boldsymbol{p}'-\boldsymbol{p})^2 = \frac{V}{(2\pi)^3}\delta(\boldsymbol{p}'-\boldsymbol{p}).\tag{2.52}$$

Now we establish the mathematical trick, which allows us to calculate the whole momentum distribution in a single propagation. So far, we approximated the negative-energy momentum eigenstate by a Gaussian distribution normalized to one, representing a single particle in the Dirac sea. To obtain the whole momentum distribution of the created electrons one has to integrate over all initial momenta after the propagation. However, it is possible to do the integration beforehand. Instead of employing a Gaussian momentum distribution, we may start the calculation from a very different negative-energy state that includes all possible electron momenta within the x-y-plane up to a certain maximum magnitude. The new initial state reads

$$\psi_{\Upsilon}^{r}(t<0) = \frac{V^{1/3}}{2\pi}\int d^3p\,\delta(p_z)\Theta(\Upsilon^2-\boldsymbol{p}^2)\phi_{\boldsymbol{p}}^{r},\tag{2.53}$$

where $r\in\{3,4\}$, Θ denotes the usual step function and Υ stands for the maximum momentum as imposed by the spatial grid resolution. Note that ψ_{Υ}^{r} is not normalized to one, instead the norm is given by $\sqrt{\pi}\Upsilon$. It may be viewed as a state that represents essentially the whole Dirac vacuum. Note however, that this is only an intuitive picture, ψ_{Υ}^{r} does not represent a multi-particle wave function. Employing equation (2.49), the new wave function is given after the propagation by

$$\psi_{\Upsilon}^{r}(t>T) = \frac{V^{1/3}}{2\pi}\int d^3p\,\delta(p_z)\Theta(\Upsilon^2-\boldsymbol{p}^2)\left(c_1(\boldsymbol{p},r)\phi_{\boldsymbol{p}}^{5-r}+c_2(\boldsymbol{p},r)\phi_{\boldsymbol{p}}^{r}\right).\tag{2.54}$$

Projection onto positive-energy states and summation over the initial spin variable after the interaction yields

$$\begin{aligned}\sum_{r=3}^{4}\left|\left\langle\phi_{\boldsymbol{p}'}^{r'}\middle|\,\psi_{\Upsilon}^{r}\right\rangle\right|^2 &= \sum_{r=3}^{4}\left|\frac{V^{1/3}}{2\pi}\int d^3p\,\delta(p_z)\Theta(\Upsilon^2-\boldsymbol{p}^2)c_1(\boldsymbol{p},r)\frac{(2\pi)^3}{V}\delta_{r',5-r}\delta(\boldsymbol{p}'-\boldsymbol{p})\right|^2\\ &= \frac{(2\pi)^4}{V^{4/3}}\sum_{r=3}^{4}\left|\delta(p_z')\Theta(\Upsilon^2-\boldsymbol{p}'^2)c_1(\boldsymbol{p}',r)\delta_{r',5-r}\right|^2\\ &= \frac{(2\pi)^3}{V}\delta(p_z')\Theta(\Upsilon^2-\boldsymbol{p}'^2)\left|c_1(\boldsymbol{p}',5-r')\right|^2. \end{aligned}\tag{2.55}$$

In comparison with equation (2.50), we obtain essentially the two dimensional momentum spectrum $|c_1(\boldsymbol{p}', 5 - r')|^2 \big|_{p'_z=0}$ in the region $\sqrt{{p'_x}^2 + {p'_y}^2} < \Upsilon$.

Figure 2.10 and Figure 2.11 show two examples of momentum distributions for linear polarization, $\xi = 1$ and frequency $\omega = \omega_5 = 0.49072m$ which corresponds to a 5-photon resonance for $\boldsymbol{p} = 0$. The results are independent of the specific spin state, chosen perpendicular to the interaction plane. In Figure 2.10 a (0.5|13.0|0.5) cycle pulse was applied; the pulse length corresponds to the first maximum in the Rabi oscillation of the transition probability for $\boldsymbol{p} = 0$. To show the ensuing minimum in the Rabi oscillation a longer pulse length of (0.5|27.5|0.5) cycles was applied in Figure 2.11. The momentum distributions display a characteristic resonance-ring structure, originating from the momentum dependence of q_0 (see equation (2.37)). It arises from higher photon number contributions, where the condition in equation (2.40) can be satisfied for certain momentum values and photon numbers $n > n_0$ with $n = 2q_0(\boldsymbol{p})/\omega \in \mathbb{N}$. Here n_0 is defined as the lowest possible photon number fulfilling the resonance condition. The finite width of the resonance-rings and the suppressed structure between them arise from the finite pulse length and the resultant spectral width. For longer pulse duration the width of the rings becomes sharper and the intermediate structure flattens out.

Moreover, the resonance-rings show a regular substructure of minima. For even photon numbers (e.g. $n = 6$) the minima are located at positions where p_y is an integral multiple of the photon frequency. In contrast to that, for odd photon numbers (e.g. $n = 7$) minima arise at odd multiples of half the field frequency. This superimposed substructure is a consequence of the periodicity of the applied field. Each cycle contributes coherently to the momentum distribution. Due to a phase shift between these contributions, there is an interference effect causing the aforementioned minima [100]. For an infinite pulse length these interferences lead, for $\xi = 1$, to the appearance of a factor

$$\left[1 + (-1)^{n+2s} \cos(2\pi p_y/\omega)\right], \tag{2.56}$$

in the resonant pair creation probability[1]. The number s takes the spin statistics into account, for bosons $s = 0$ and for fermions $s = 1/2$. So the position of the maxima and minima on the resonance-rings is reversed for bosonic systems. One should mention, that even a few-cycle pulse is enough to establish this pronounced substructure.

[1]It seems to us, that in equation (17) of [100] a factor of 2 is missing in the definition of β. There the function β reduces for $\xi = 1$ to $\beta = \pi p_y/\omega$. For other values of ξ the numerical factor in β would be different, leading to a correspondingly modified substructure.

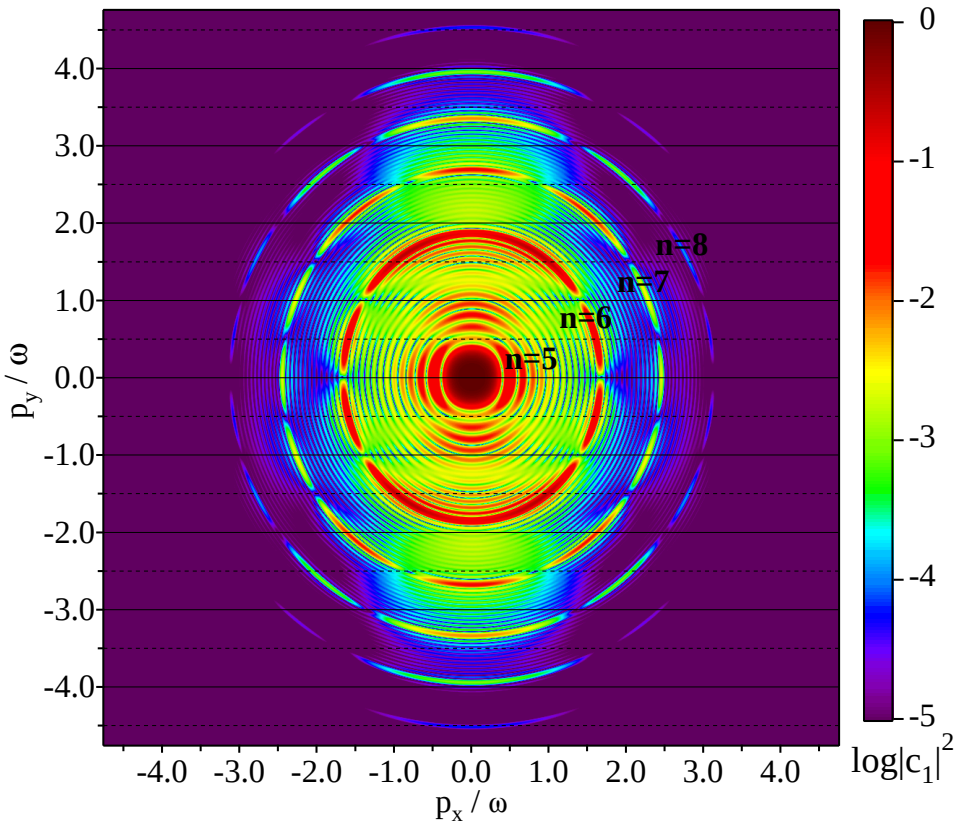

Figure 2.10: Momentum distribution of the created electrons for linear laser polarization, a pulse shape of (0.5|13.0|0.5), and a laser frequency of $\omega = 0.49072m$, corresponding to a five photon resonance at $\boldsymbol{p} = 0$. The polarization direction corresponds to the p_y-axis. In order to show the Rabi oscillation, the pulse length was chosen in such a way, that this Figure and the following Figure 2.11 show a maximum and a minimum for $\boldsymbol{p} = 0$, respectively. The ring structure originates from higher photon resonances representing in this case $n = 6, 7, 8, \ldots$ photon absorption. Solid lines corresponding to $p_y = l\omega$ and dashed lines corresponding to $p_y = (2l+1)\omega/2$ for $l \in \mathbb{Z}$ are drawn to show the position of the maxima and minima in the substructure of the resonance-rings more clearly.

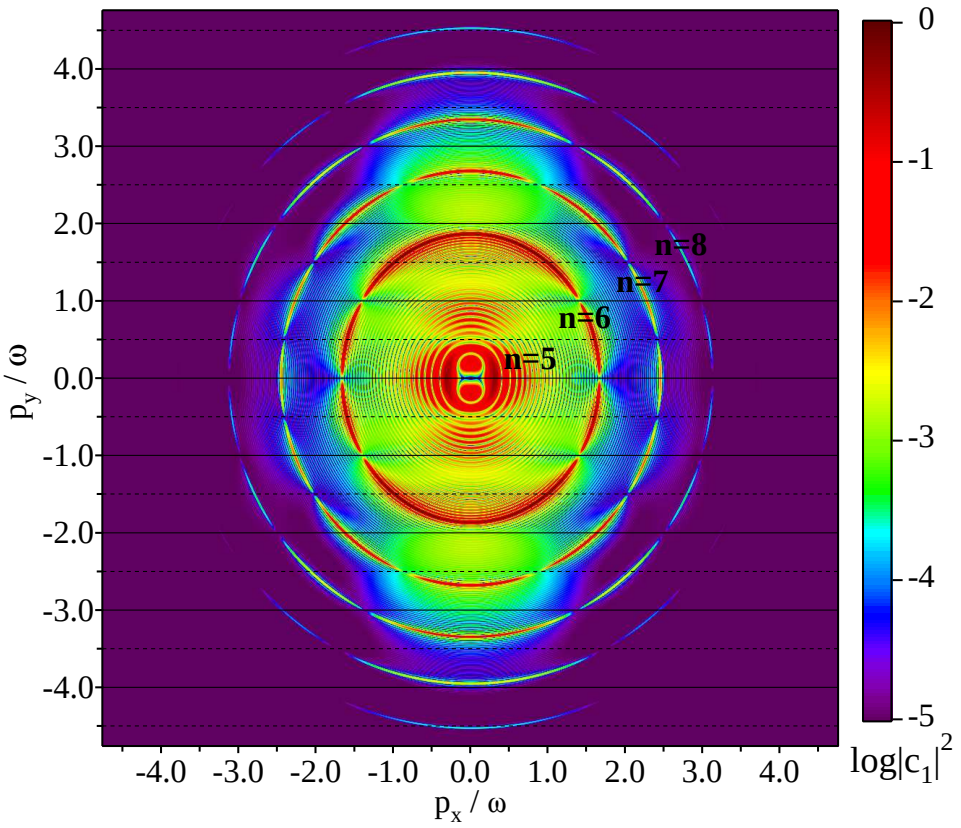

Figure 2.11: Same as Figure 2.10 but for a longer pulse length of (0.5|27.5|0.5). The latter was chosen such that the Rabi oscillation passes through a minimum at $\boldsymbol{p} = 0$. Note that for longer pulse duration, the width of the resonance-rings becomes sharper.

To compare the positions of the resonance-rings obtained with the results found in the quasiclassical approach, we consider a cut of the momentum distribution from Figure 2.10 along the p_y-axis. This cut is shown in Figure 2.12 with the frequency-scaled quasi-energy from Figure 2.2. The agreement of the resonance positions is almost perfect. The small deviations are due to the finite pulse length, not included in the quasiclassical calculation.

Figure 2.13 shows the momentum spectrum obtained by the same field configuration as in Figure 2.10, but for the case of a bosonic system. Here the momentum $\boldsymbol{p} = 0$ corresponds to a stationary minimum, explained by the charge conjugation argument given before. The notion stationary means, that the minimum is independent of the applied pulse duration. In contrast to this, the minima at $\boldsymbol{p} = 0$ in Figure 2.11 corresponds to a minimum of the Rabi oscillation and occurs therefore only for specific pulse durations. The substructure of the resonance-rings is switched in accordance with equation (2.56).

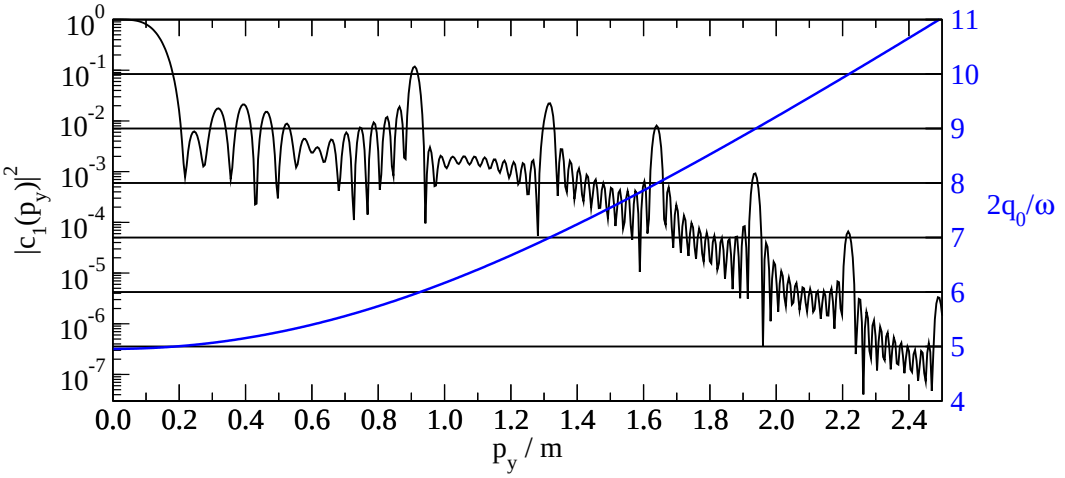

Figure 2.12: The black line denotes a cut along the p_y-axis of the momentum distribution from Figure 2.10. The laser is linearly polarized with $\omega = 0.49072m$ and $\xi = 1$. The blue curve shows the frequency-scaled quasi-energy. Crossings of this curve with the integer lines (black) indicate momenta that meet the resonance condition.

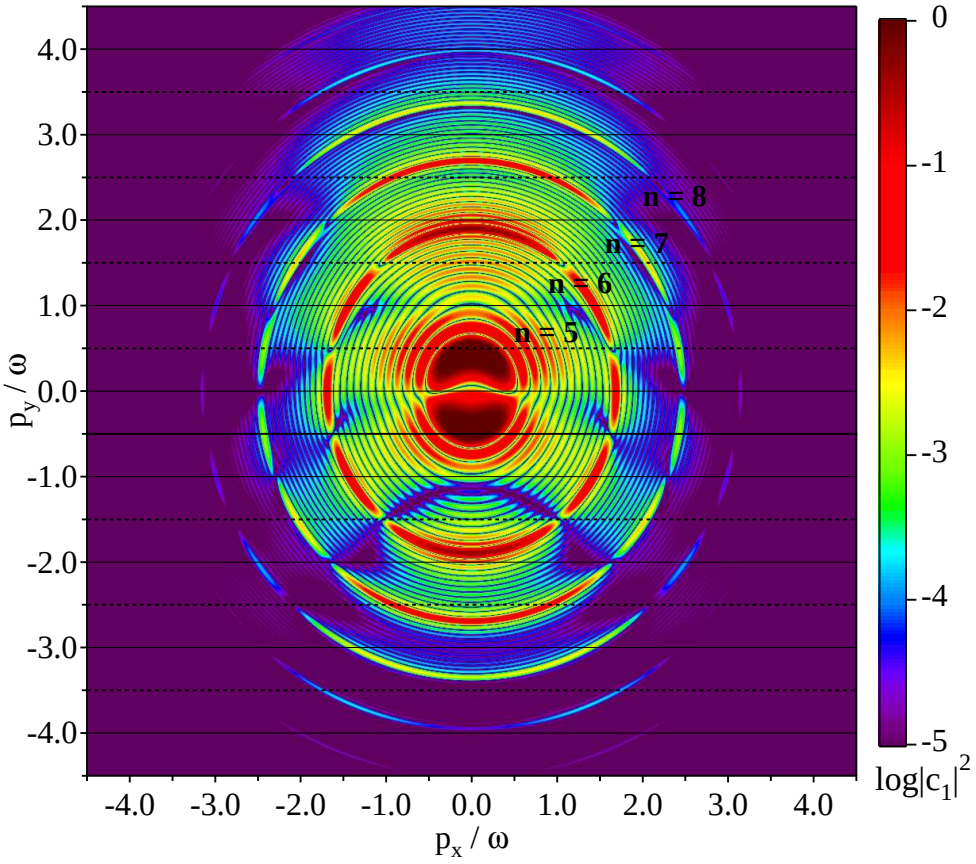

Figure 2.13: Momentum distribution of the created Klein-Gordon particles for linear laser polarization, a pulse shape of $(0.5|13.0|0.5)$, and a laser frequency of $\omega = 0.49072m$, corresponding to a five photon resonance at $\boldsymbol{p} = 0$. The polarization direction corresponds to the p_y-axis. Due to charge conjugation symmetry, the momentum $\boldsymbol{p} = 0$ corresponds to a stationary minimum here (cp. Figure 2.10 for the Dirac case). The ring structure originates from higher photon resonances representing in this case $n = 6, 7, 8, \ldots$ photon absorption. Solid lines corresponding to $p_y = l\omega$ and dashed lines corresponding to $p_y = (2l+1)\omega/2$ for $l \in \mathbb{Z}$ are drawn to show the position of the maxima and minima in the substructure of the resonance-rings more clearly. The positions of the minima and maxima are interchanged compared to the Dirac case shown in Figure 2.10, in accordance to equation (2.56).

A special feature of the linear polarization case is the possibility to obtain 3-dimensional total probabilities per volume, due to the aforementioned symmetry of the potential. The total probability is given by the sum over all final spin states followed by an integration over all final momenta of the density distribution (2.46)

$$W_{tot} = \sum_{r'=1}^{2}\sum_{r=3}^{4}\int \frac{Vd^3p'}{(2\pi)^3}\int \frac{Vd^3p}{(2\pi)^3}\left|\left\langle \phi_{\boldsymbol{p}'}^{r'}\right|\psi_{\boldsymbol{p}}^{r}\right\rangle\right|. \tag{2.57}$$

By virtue of the rotational symmetry of the problem, the matrix element is rotationally invariant around the field axis. Introducing cylindrical coordinates (ρ,φ,y) with respect to the field axis, equation (2.57) therefore becomes

$$\begin{aligned}
W_{tot} &= \frac{V^2}{(2\pi)^6}\sum_{r'=1}^{2}\sum_{r=3}^{4}\int_0^{2\pi}dp'_\varphi\int_{-\infty}^{\infty}dp'_y\int_0^{\infty}dp'_\rho\,p'_\rho\int d^3p\left|\left\langle \phi_{\boldsymbol{p}'}^{r'}\right|\psi_{\boldsymbol{p}}^{r}\right\rangle\right| \qquad (2.58)\\
&= \frac{V^2}{(2\pi)^5}\sum_{r'=1}^{2}\sum_{r=3}^{4}\int_{-\infty}^{\infty}dp'_y\int_0^{\infty}dp'_\rho\,p'_\rho\int d^3p\left|c_1(\boldsymbol{p},r)\frac{(2\pi)^3}{V}\delta_{r',5-r}\delta(\boldsymbol{p}'-\boldsymbol{p})\right|^2\Bigg|_{p'_\varphi=0}\\
&= \frac{V}{(2\pi)^2}\sum_{r'=1}^{2}\sum_{r=3}^{4}\int_{-\infty}^{\infty}dp'_y\int_0^{\infty}dp'_\rho\,p'_\rho\int d^3p\,|c_1(\boldsymbol{p},r)|^2\,\delta_{r',5-r}\delta(\boldsymbol{p}'-\boldsymbol{p})\Big|_{p'_\varphi=0}\\
&= \frac{V}{(2\pi)^2}\int_{-\infty}^{\infty}dp'_y\int_0^{\infty}dp'_\rho\,p'_\rho\left(\left|c_1(\boldsymbol{p}',3)\right|^2+\left|c_1(\boldsymbol{p}',4)\right|^2\right)\Big|_{p'_\varphi=0}.
\end{aligned}$$

This leads to the total probability per volume

$$\frac{W_{tot}}{V} = \frac{1}{(2\pi)^2}\int_{-\infty}^{\infty}dp'_y\int_0^{\infty}dp'_\rho\,p'_\rho\left(\left|c_1(\boldsymbol{p}',3)\right|^2+\left|c_1(\boldsymbol{p}',4)\right|^2\right)\Big|_{p'_\varphi=0}. \tag{2.59}$$

Taking the modified wave function into account, we define

$$\tilde{W}_{tot}(\Upsilon) = \frac{V}{2(2\pi)^2}\sum_{r'=1}^{2}\sum_{r=3}^{4}\int d^3p'|p'_x|\left|\left\langle \phi_{\boldsymbol{p}'}^{r'}\right|\psi_{\Upsilon}^{r}\right\rangle\right|^2. \tag{2.60}$$

By employing equation (2.55) this may be written as

$$\begin{aligned}
\tilde{W}_{tot}(\Upsilon) &= \frac{V}{2(2\pi)^2}\sum_{r'=1}^{2}\int d^3p'|p'_x|\delta(p'_z)\Theta(\Upsilon^2-\boldsymbol{p}'^2)\left|c_1(\boldsymbol{p}',5-r')\right|^2 \qquad (2.61)\\
&= \frac{V}{2(2\pi)^2}\sum_{r'=1}^{2}\int_{-\infty}^{\infty}dp'_y\int_{-\infty}^{\infty}dp'_x|p'_x|\Theta(\Upsilon^2-\boldsymbol{p}'^2)\left|c_1(\boldsymbol{p}',5-r')\right|^2\Big|_{p'_z=0}\\
&= \frac{V}{(2\pi)^2}\int_{-\infty}^{\infty}dp'_y\int_0^{\infty}dp'_x|p'_x|\Theta(\Upsilon^2-\boldsymbol{p}'^2)\left(\left|c_1(\boldsymbol{p}',3)\right|^2+\left|c_1(\boldsymbol{p}',4)\right|^2\right)\Big|_{p'_z=0}.
\end{aligned}$$

By comparing equation (2.59) with equation (2.61), it follows that

$$\frac{W_{tot}}{V} = \lim_{\Upsilon\to\infty}\frac{\tilde{W}_{tot}(\Upsilon)}{V}. \tag{2.62}$$

In the above, we have exploited the fact, that within the x-y-plane we have

$$\left|c_1(p'_x,p'_y,p'_z,r')\right|^2\Big|_{p'_z=0} = \left|c_1(-p'_x,p'_y,p'_z,r')\right|^2\Big|_{p'_z=0} = \left|c_1(p'_\rho,p'_y,p'_\varphi,r')\right|^2\Big|_{\substack{p'_\rho=|p'_x|\\ p'_\varphi=0}}. \quad (2.63)$$

In practical considerations, we cannot perform the infinite limit as in (2.62), because Υ is limited by the momentum-space grid size. Instead we pick a value $\Upsilon \simeq 3m$ that is large enough to cover all relevant contributions of $|c_1(p_x,p_y,0)|^2$ [cf. Figure (2.10)]. We also replace the step function by a sine-squared smoothed version, where the finite width of $0.2m$ helps to avoid numerical instabilities.

In performing the integral (2.61) one arrives at total probability densities, as shown in Figure 2.14 for a (0.5|13|0.5) cycle pulse in comparison with the theoretical prediction from [8]. We note that the latter was derived under the assumption $\omega \ll m$. Our numerical results agree with the analytical prediction within an order of magnitude. The pair creation probability density shows an exponential increase with the electric field frequency. At the lowest frequency shown ($\omega = 0.2m$), the total probability density amounts roughly to $5 \cdot 10^{-8}/\lambda_C^3$. This means that in a typical interaction volume $V = (10\lambda)^3$, with the laser wavelength $\lambda = 2\pi/\omega$, about one pair is produced. The step-like behavior of the numerical result is a vestige from the multiphoton regime ($\xi \ll 1$) where such characteristic jumps in the probability $W_{\mathrm{tot}} \sim \xi^{2n_0}$ are expected whenever the minimal number n_0 of required photons changes by one.

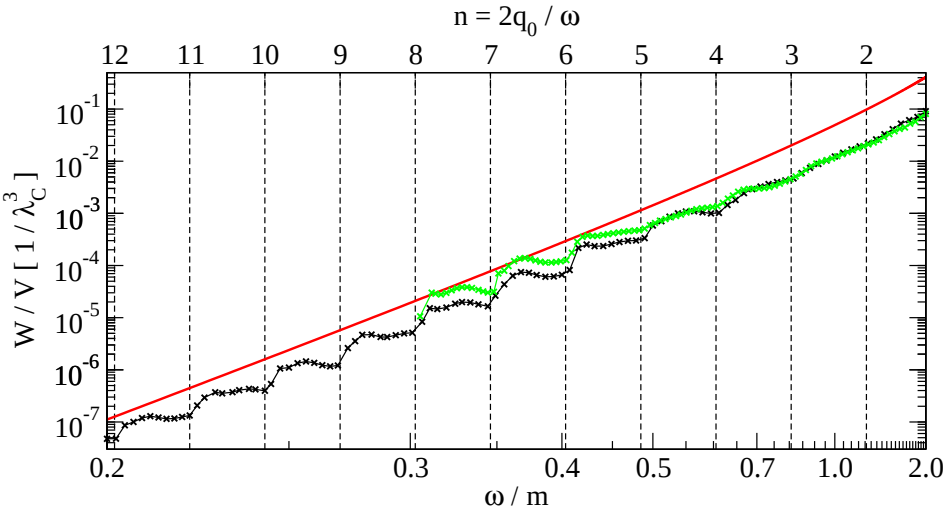

Figure 2.14: Total pair creation probabilities per volume for linear polarization and $\xi = 1$. The black crosses correspond to a (0.5|13.0|0.5) cycle pulse and the green crosses correspond to a (0.5|27.5|0.5) cycle pulse. The red curve denotes a theoretical prediction from [8] which was derived under the assumption $\omega \ll m$. In our numerical calculation, we set $\Upsilon \simeq 7m$.

Total rates are given by dividing the total probability per volume through the pulse duration. It is notable, that the Rabi oscillation has a negligible influence on these total rates for the examined frequency range $\omega \in (0.3m, 0.5m)$. The red crosses correspond to a pulse duration in accordance with the first maximum in the Rabi oscillation for the mainly contributing resonance at $\boldsymbol{p} = 0$, whereas the green crosses correspond to a pulse duration which is twice as large in accordance with a minimum in the Rabi oscillation. There is approximately a factor of 2 difference between the two, therefore the total rates are almost equal. So the Rabi oscillation may only be experimentally observable in the momentum distribution, but not in the total rates.

Turning now to circular polarized fields, Figure 2.15 and Figure 2.16 show the momentum distributions for $\omega = 0.49072m$, $\xi = 1$ and a $(0.5|13.0|0.5)$ cycle pulse. As expected, the substructure of the resonance-rings disappears and the momentum distribution becomes rotationally symmetric about the spin-axis, because the field introduces no preferential direction in the interaction plane. The small deviations from a perfect rotational symmetry originate from the finite pulse duration.

The difference between the two figures is given by the spin orientation. In contrast to the linear polarization case, where the particular spin orientation has no influence on the momentum distribution, pronounced differences are encountered here. The resonance positions appear at different momentum values, and additionally the overall height is reduced by approximately one order of magnitude for the spin-up state (Figure 2.16), compared to the spin-down state (Figure 2.15). The last observation is most obviously seen by Figure 2.17, where we compare the integral over the momentum distribution for different values of ω. This is a striking result, meaning that in the plane of investigation counterpropagating circularly polarized laser fields extract electrons from the vacuum with an imbalance of the spin orientation of approximately one order of magnitude, independent of the laser frequency.

The reason for the difference between linear and circular polarization is explained by the scheme shown in Figure 2.18, where the red lines denote the field. Although a linear-polarized field introduces a preferential direction in the interaction plane (x-y-plane), there is no such direction along the spin orientation axis. Therefore it does not break the symmetry between spin-up and spin-down states, they are indistinguishable for the field. On the contrary, the circular polarization introduces no preferential direction in the interaction plane but a rotational direction along which the electron spin may be oriented parallel or antiparallel, thus breaking the symmetry between the two different spin states.

For circular polarization the quasiclassical result of the resonance positions differs from the numerically found values especially for low momenta as seen in Figure 2.19. This is because the quasiclassical calculation has not taken the spin degree of freedom into account. Therefore the next section explains how the quasiclassical approach has to be modified in order to fix this discrepancy.

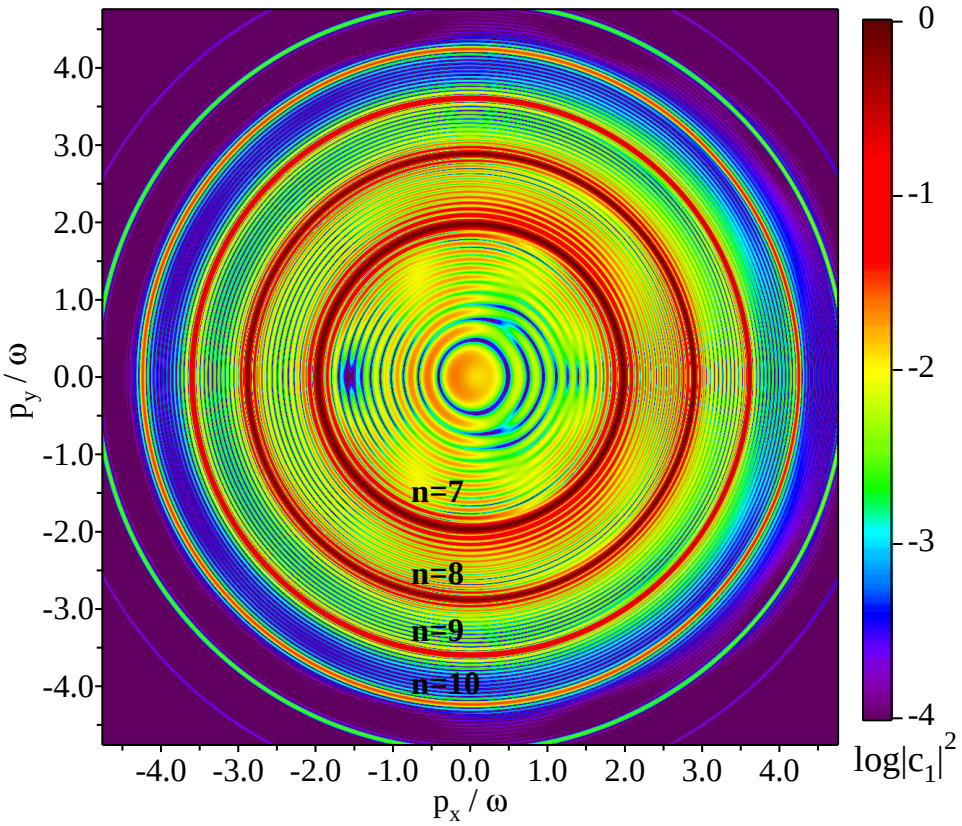

Figure 2.15: Momentum distribution of the created electrons for circular laser polarization, a pulse shape of (0.5|13.0|0.5), a laser frequency of $\omega = 0.49072m$, and an initial spin-down state along the field rotational direction. The ring structure originates from higher photon resonances representing in this case $n = 7, 8, 9, \ldots$ photon absorption, where the photon number was deduced by the spin-modified quasiclassical approach of section 2.5. The substructure of the resonance-rings encountered for linear polarization has disappeared (see Figure 2.10).

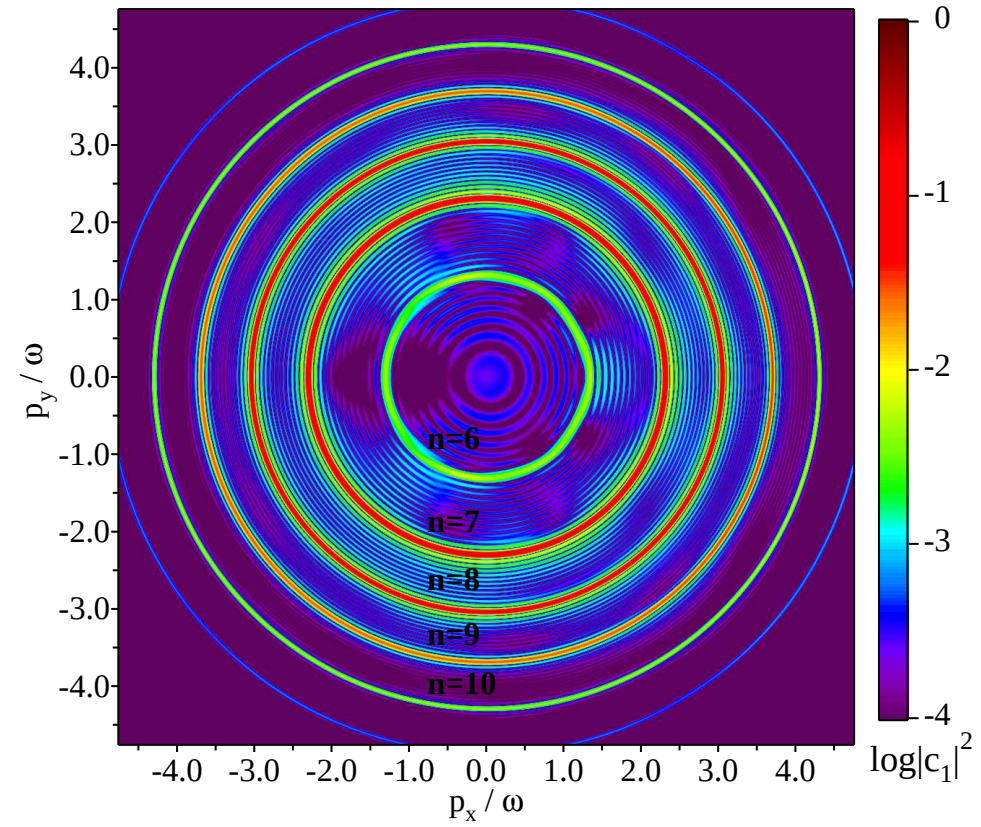

Figure 2.16: Same as Figure 2.15 but for a spin-up state along the laser field rotational direction.

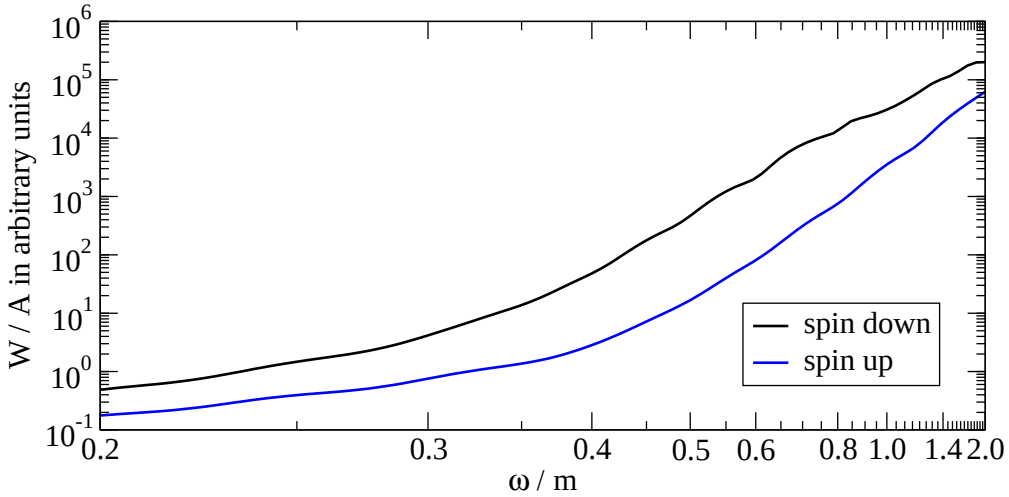

Figure 2.17: Integrated momentum distribution for the spin-up (blue curve) and spin-down (black curve) states for various laser frequencies and circular polarization. The difference is approximately independent of frequency and amounts to one order of magnitude.

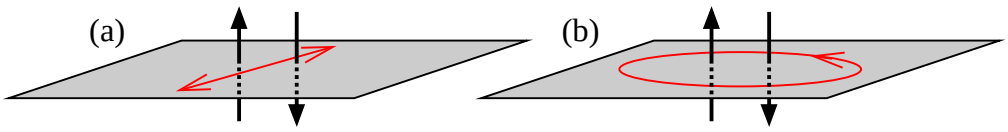

Figure 2.18: Schematic diagram illustrating the relation between the electron spin and the polarization of the laser field inducing the pair creation. The grey plane indicates the interaction plane, the two different spin orientations are denoted by the black arrows, and the red lines correspond to the laser field polarizations. (a) Linear polarization: the field does not break the symmetry between the two different spin states. (b) Circular polarization: the field introduces a preferential direction along which the electron spin may be oriented parallel or antiparallel, thus breaking the symmetry between the two different spin states.

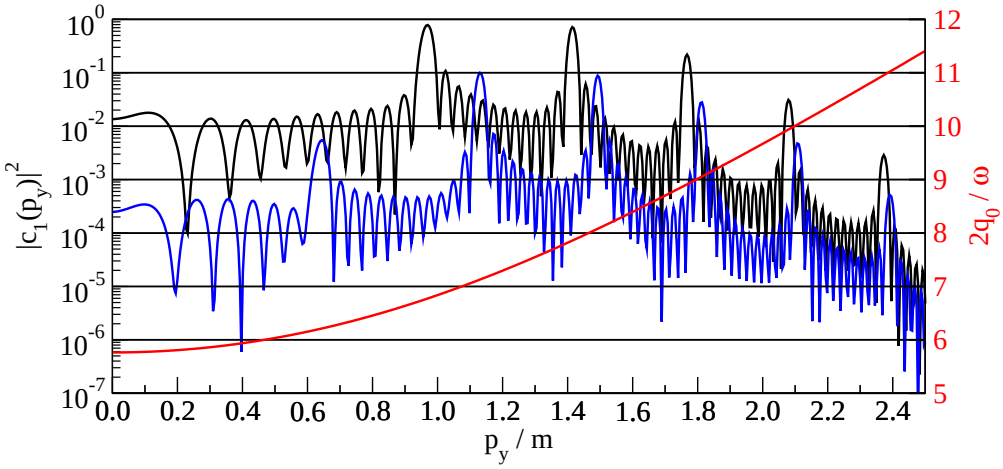

Figure 2.19: Comparison of the numerically found resonance positions and the result obtained from the quasiclassical consideration for circular polarization. The black curve corresponds to a cut through the spin-down momentum distribution (Figure 2.15), whereas the blue curve corresponds to a cut through the spin-up momentum distribution (Figure 2.16). The red line denotes the frequency scaled quasi-energy obtained by the quasiclassical approach in section 2.2. Every time it crosses an integer line the resonance condition is fulfilled. However, the quasiclasically found resonances do not agree with the observed ones.

2.5 Spin-modified quasiclassical approach

As seen in the previous section, the spin orientation plays a crucial role in the e^+e^- pair creation process for circular laser polarization. However, the quasiclassical calculation presented in section 2.2 has not taken the spin degree of freedom into account. The quasiclassical approach was based on the classical relativistic Hamiltonian

$$H(\boldsymbol{q},t) = \sqrt{m^2 + (\boldsymbol{p} - e\boldsymbol{A}(t))^2}. \tag{2.64}$$

This has to be supplemented by the electron spin interaction energy. Although the magnetic field vanishes identically in the laboratory frame, due to the pure time dependence of the vector potential, the electron encounters a magnetic field in its rest frame leading to a nonvanishing spin interaction energy. The equation of motion for the spin vector $\boldsymbol{s}$ is given by the Thomas equation [101]

$$\frac{d\boldsymbol{s}}{dt} = \frac{e}{m}\boldsymbol{s} \times \left[\left(\frac{g}{2} - 1 + \frac{1}{\gamma} \right) \boldsymbol{B} - \left(\frac{g}{2} - 1 \right) \frac{\gamma}{\gamma+1} (\boldsymbol{\beta}\cdot\boldsymbol{B})\boldsymbol{\beta} - \left(\frac{g}{2} - \frac{\gamma}{\gamma+1} \right) \boldsymbol{\beta} \times \boldsymbol{E} \right], \tag{2.65}$$

where $\boldsymbol{\beta}$ is the velocity of the electron, $\gamma = (1-\boldsymbol{\beta}^2)^{-1/2}$, g is the Landé-g factor, and $\boldsymbol{E}$ and $\boldsymbol{B}$ denote the magnetic and electric field, respectively. Taking $\boldsymbol{B} = \nabla \times \boldsymbol{A} = 0$ and $g = 2$ into account yields

$$\frac{d\boldsymbol{s}}{dt} = -\frac{e}{m} \left(1 - \frac{\gamma}{\gamma+1} \right) \boldsymbol{s} \times (\boldsymbol{\beta} \times \boldsymbol{E}). \tag{2.66}$$

Equation (2.66) corresponds to a spin interaction energy of

$$U = \frac{e}{m} \left(1 - \frac{\gamma}{\gamma+1} \right) \boldsymbol{s} \cdot (\boldsymbol{\beta} \times \boldsymbol{E}). \tag{2.67}$$

We now employ the approximation, that $\boldsymbol{\beta}$ and γ are given via the unperturbed Hamiltonian (2.64)

$$\boldsymbol{\beta} \approx \frac{\boldsymbol{p} - e\boldsymbol{A}}{m\gamma}, \tag{2.68}$$

$$\gamma \approx \frac{H}{m}. \tag{2.69}$$

With $\boldsymbol{E} = -\dot{\boldsymbol{A}} = -\partial\boldsymbol{A}/\partial t$, this leads to a spin interaction energy of

$$U = -\frac{e}{H(H+m)} \boldsymbol{s} \cdot \left(\boldsymbol{p} \times \dot{\boldsymbol{A}} - e\boldsymbol{A} \times \dot{\boldsymbol{A}} \right). \tag{2.70}$$

Employing the specific form of the vector potential (2.1) and the fact that $\boldsymbol{p}$ lies in the x-y-plane, leads finally to

$$U = -\sigma \frac{m\omega\xi}{2H(H+m)} \left[\theta\xi + \theta p_x \cos(\eta) + p_y \sin(\eta) \right], \tag{2.71}$$

where $\sigma = 1$ for spin-up and $\sigma = -1$ for spin-down. This spin interaction energy has to be added to the Hamiltonian (2.64), leading to a new spin modified Hamiltonian

$$H \to H^\sigma = H + U. \tag{2.72}$$

Now one may follow the same path as in section 2.2 to obtain the quasiclassical approximation for the Dirac wave function

$$\psi_{\pm}^{\sigma} \sim \exp(iS_{\pm}^{\sigma}), \tag{2.73}$$

where the $(\pm)$ sign indicates the two possible signs in energy, and σ denotes explicitly the dependence on the spin orientation.

The first step is to find the classical action $S_{\pm}^{\sigma}$ obeying the Hamilton-Jacobi equation (2.31), but now with respect to the new spin-modified Hamiltonian (2.72). It separates again into a spatial and a temporal part, where the temporal part may be further decomposed into a linear and a periodic component, according to

$$\begin{aligned} S_{\pm}^{\sigma} &= \boldsymbol{qr} \mp \frac{1}{\omega}\int_{\eta_0}^{\eta} d\eta'\, H^{\sigma}(\eta') && (2.74)\\ &= \boldsymbol{qr} \mp q_0^{\sigma} t \pm S_p^{\sigma}(\eta). && (2.75) \end{aligned}$$

This results in an explicitly spin dependent quasi-energy q_0^{σ}, given by

$$q_0^{\sigma} = \frac{1}{2\pi}\int_0^{2\pi} d\eta'\, H^{\sigma}(\eta'). \tag{2.76}$$

According to the conservation of momentum and additionally the conservation of the spin like-operator (2.47), the transition amplitude for pair creation is given by

$$\psi_{-}^{\sigma\dagger}\psi_{+}^{\sigma} \sim \exp\big(2i(S_p^{\sigma}(\eta) - q_0^{\sigma} t)\big). \tag{2.77}$$

Due to the 2π-periodicity of S_p^{σ} this can be expanded into a Fourier series

$$\psi_{-}^{\sigma\dagger}\psi_{+}^{\sigma} \sim \sum_{n=-\infty}^{\infty} \mathcal{C}_n^{\sigma} \exp\big(i(n\omega - 2q_0^{\sigma})t\big), \tag{2.78}$$

where the index n indicates the number of photons involved in the process, and the Fourier coefficients

$$\mathcal{C}_n^{\sigma} = \frac{1}{2\pi}\int_0^{2\pi} d\eta \, \exp\big(i\left(2S_p^{\sigma}(\eta) - n\eta\right)\big) \tag{2.79}$$

are related via

$$W_n^{\sigma} \sim |\mathcal{C}_n^{\sigma}|^2 \tag{2.80}$$

to the n-photon e^+e^- pair creation probability. The energy conservation condition is recovered as

$$n_0\omega = 2q_0^{\sigma}, \tag{2.81}$$

leading to different resonance conditions for the two spin orientations.

The spin modification is now illustrated on the example of the last section, in which the discrepancy between the numerical and former quasiclassical results appeared. Figure 2.20 shows the influence of the two spin orientations on the quasi-energy for circular polarization and $\omega = 0.49072m$. The red curve denotes the former spin independent result obtained in section 2.2. Due to the spin, it is split into two different quasi-energies, corresponding to spin up (blue curve) and spin down (black curve), respectively. This leads to different resonance positions for the two different spin orientations.

The comparison of these new spin-dependent resonance positions and the numerically found momentum distributions is shown in Figure 2.21. Here the blue curves correspond to the spin-up state, whereas the black curves correspond to the spin-down state. With the spin degree of freedom included, the resonance positions now agree satisfactorily.

Moreover, Figure 2.22 shows the magnitude of the Fourier coefficients, which exhibit the same decrease in probability as encountered in the momentum distributions.

One should note, that although the spin-interaction energy (2.71) does not vanish for linear polarization, it has no influence on the resonance positions in this case, because the additional term disappears when integrated over. Therefore the quasi energy and the Fourier coefficients stay the same for linear polarization, so that the spin-modified calculation gives the same results obtained before in accordance with our observations.

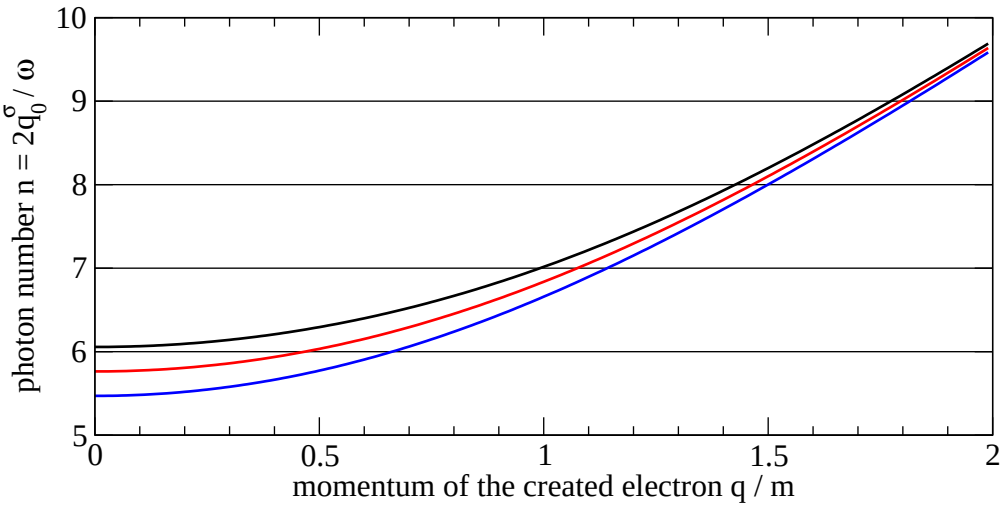

Figure 2.20: Spin modification of the quasi-energy q_0 for circular polarization, $\xi = 1$, and $\omega = 0.49072m$. The red curve denotes the spin-independent quasi-energy obtained in section2.2. The spin introduces a shift in energy with opposite sign for the two possible spin orientations along the field rotational axis. The black curve corresponds to spin-down, and the blue curve corresponds to spin-up. The crossings with the black integer lines denote the positions of the resonance momenta, which occur now at different positions for the two different spin states, in accordance with the results obtained in the last section.

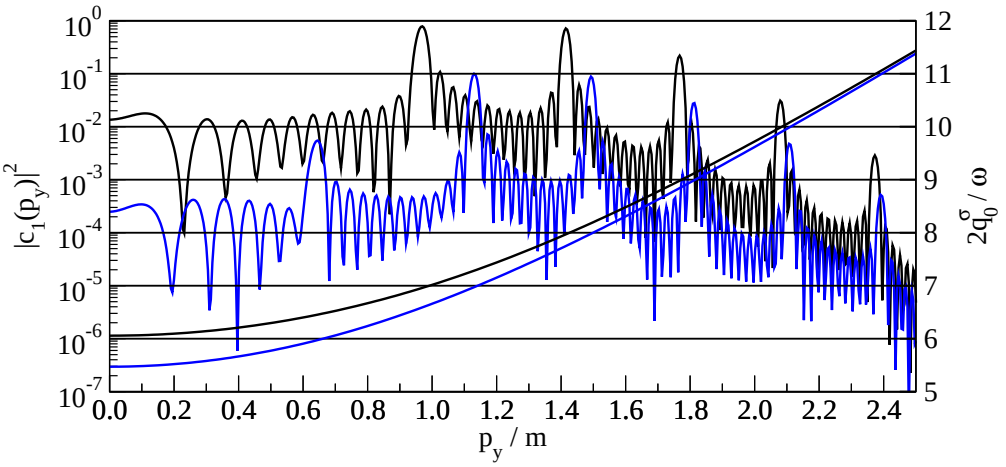

Figure 2.21: Same as Figure 2.19, but with the new spin-modified quasi-energies. The new obtained resonance positions agree satisfactorily with the numerically found resonances of the momentum distributions.

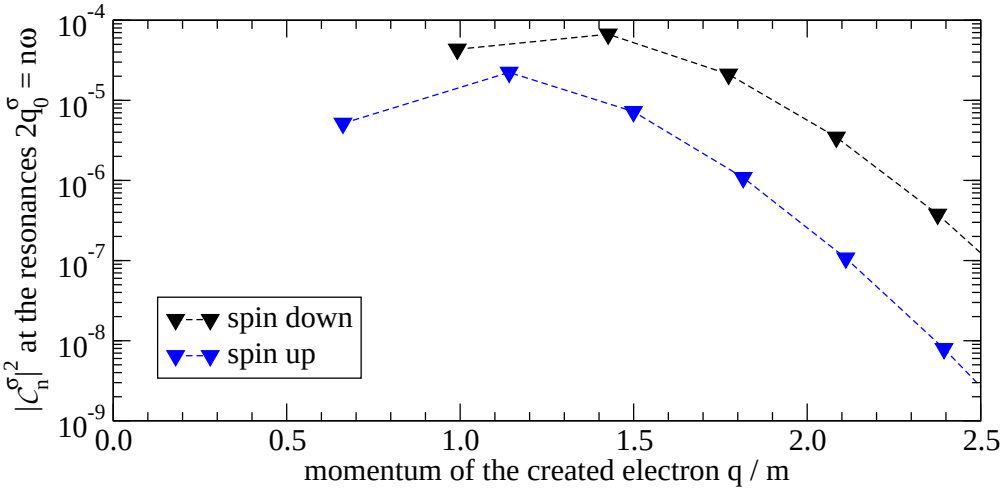

Figure 2.22: Spin corrected Fourier coefficients at the resonance momenta for circular polarization, $\xi = 1$, and $\omega = 0.49072m$. The same difference in probability of approximately one order of magnitude between the spin-up (blue curve) and the spin-down (black curve) states is recovered.

Chapter 3

Magnetic field effects

In the last chapter we investigated purely laser-induced pair creation for two counterpropagating laser pulses of equal frequency and intensity, resulting in a standing wave. This standing laser wave has been approximated by a spatially homogeneous electric field oscillating in time. So far, all theoretical investigations have employed this dipole approximation [8, 23, 24, 27–29, 31, 32, 34, 35, 47–49, 92–96]. In optical laser fields, where the wavelength is much larger than the typical length scale of the process: $\lambda \gg l_c = m/(|e|E)$, this dipole approximation is expected to be well-justified. In terms of the relativistic parameter ξ, this relation corresponds to $\xi \gg 1$. Nowadays the experimental realization of laser-induced pair production is also extensively discussed in connection with upcoming x-ray free-electron laser (XFEL) facilities [24, 95, 96]. In this case, however, the laser frequency is high, $\xi \lesssim 1$ and the magnetic field component is not negligible. The latter, in general, can have an important influence on the pair creation process. This is most evidently demonstrated by the fact that a single plane laser wave cannot extract pairs from vacuum, whereas a purely electric field can. The investigation of fields, which are both inhomogeneous in time and space represents a formidable task for the nonperturbative quantum field theory, see e.g. [51–53]. However, employing the numerical approach, presented in the last chapter, enables us in principle to examine pair creation in external potentials independently of their specific form.

This chapter continues the numerical study of e^+e^- pair creation by two counterpropagating strong laser pulses (CLP) of high frequency, taking into account explicitly the spatiotemporal dependence of the laser fields and their magnetic components. This limits our considerations to the case of linear polarized laser fields, because circular polarization would automatically lead to 3-dimensional dynamics. Due to the space dependence of the fields, the momentum is no longer conserved. This means, that the mathematical trick for obtaining the momentum distributions of the created electrons, presented in section 2.4, is not applicable. Therefore we have to investigate the transition from an initially negative-energy state under the influence of the external field, into the positive continuum, for each individual initial momentum. This renders the task to gain momentum distributions impossible, irrespectively of the enormous computer capacity available. For this reason, our calculations assume an initially narrow Gaussian wave-packet centered around $\boldsymbol{p} = 0$ of width $\Delta p \approx \alpha m$, lying in the negative-energy continuum. The width is chosen sufficiently narrow to closely approximate a momentum

eigen-state and to exclude unphysical interference effects between different momentum components as $\Delta p \ll \omega$ always holds. A particular spin state along the magnetic field direction (normal to the plane of calculation) is chosen; the opposite spin orientation would give identical results. The wave-packet is exposed to two linearly polarized plane-wave laser pulses counterpropagating along the z-axis, with fixed $\xi = 1$ (taken for both laser pulses together), and featuring $\sin^2$ turn-on and turn-off phases of half a cycle each. The number of plateau cycles with constant intensity is variable. To save computing time the fields are switched off when they do not overlap anymore.

The first section presents the results of the obtained transition probabilities and the corresponding resonance spectrum. The magnetic component of the laser field strongly affects the creation process: the resonant Rabi oscillation pattern is distorted and the resonances are shifted, multiplied and split. The origin of the observed resonance peak splitting is explained in the second section.

3.1 Modified Rabi oscillations and multiplied resonances

The pair production probability is expected to depend on the pulse length as known from the oscillating electric field case in section 2.3, where resonant Rabi oscillations were encountered. In order to depict the influence of the magnetic component of the laser field, the red curve in Figure 3.1 (a) shows the found Rabi oscillation in an oscillating electric field for $\omega = \omega_5 = 0.49072m$ corresponding to an $n = 5$ photon resonance. To compare this with the results obtained in the CLP case one has to find the $n = 5$ resonance frequency for the latter. However, for the CLP case the quasi-energy q_0 is no longer analytically computable. Figure 3.1 (b) shows therefore the transition probabilities for various frequencies starting from $\omega = 0.46m$. The closest obtained resonance frequency, compared to ω_5, is given by $\omega = 0.4721m$. Actually, this corresponds to an $n = 5$ photon transition. The identification of the photon numbers n for the resonances in the CLP case will be explained below. The oscillation pattern is strongly modified by inclusion of the laser magnetic field, which is seen most clearly in Figure 3.1 (b). The probability oscillates around a plateau value with a frequency five times smaller than the Rabi frequency Ω in an oscillating electric field. Note that the pair production rate at small times $t \ll \Omega^{-1}$ scales as Ω^2 [27–29, 31, 32] and is therefore reduced due to the magnetic field effect by 1-2 orders of magnitude. The question arises, if this reduces the probability for an observation of this process at facilities like the XFEL considerably. For $\xi \lesssim 1$ the answer is yes. However, some of the more favorable and principally feasible regimes of the XFEL for pair production requires $\xi \sim 10$ [24], where the reduction of the process probability by the laser magnetic field is not significant.

Taking for each frequency the maximum of the production probability as a function of the laser pulse duration, one arrives at the resonance spectrum shown in Figure 3.2. This way the normally superimposed pulse length-dependent oscillations of the probability are omitted, and the resonances are clearly visible. The picture changes significantly when real laser fields are applied: The height of the probability spectrum is reduced by approximately one order of magnitude, the resonances are shifted, several new resonances occur, and the resonance lines are split.

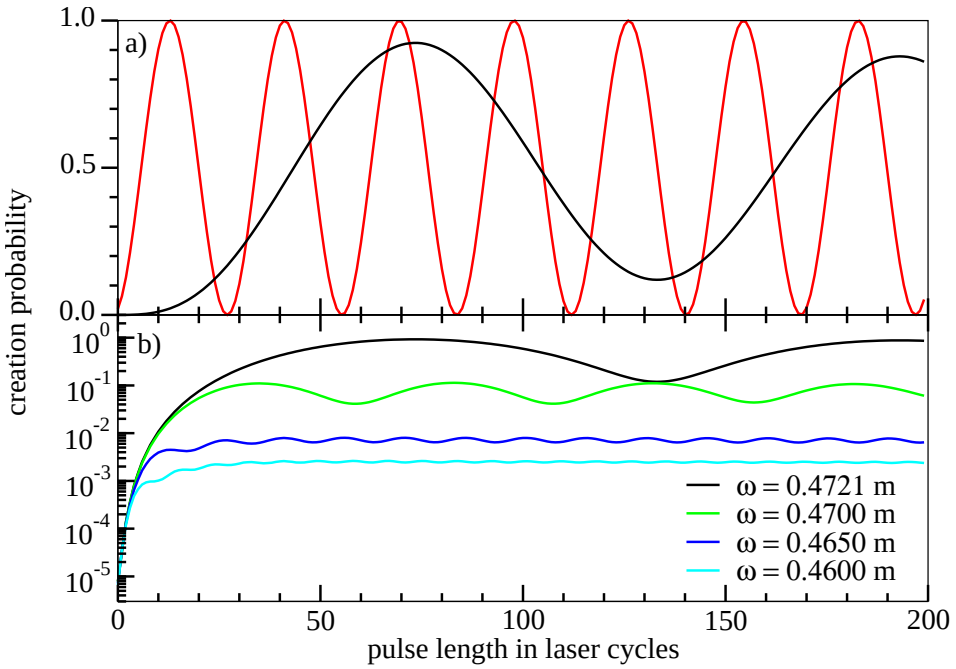

Figure 3.1: Distorted Rabi oscillations: Pair production probability versus pulse length at $\xi = 1$. (a) The red and the black curve show the case for an oscillating electric field with $\omega = 0.49072m$ and the CLP case for $\omega = 0.4721m$, respectively, each corresponding to a 5-photon resonance. (b) CLP case for various frequencies on a logarithmic scale. The black solid curve coincides with the resonant case in part (a), while the others correspond to off resonant situations.

In order to explain these modifications, we examined the corresponding momentum distributions of the created electron as shown in Fig. 3.3 for the peaks labeled by (3-1), (4-1), (2-2) and (3-2). In contrast to the oscillating electric field, the photons in the CLP carry momentum along the beam propagation axis, which is transferred to the electron wave-packet upon absorption. Only the transversal momentum components are conserved here. By energy-momentum conservation, a number of n_+ (n_-) photons absorbed from the beam propagating to the right (left) determine the laser-dressed final particle 4-quasi-momenta:

$$q'_0 = (n_+ + n_-)\,\omega - q_0 \tag{3.1a}$$
$$q'_3 = (n_+ - n_-)\,\omega - q_3 \tag{3.1b}$$

where q and q' are the electron initial and final 4-quasi-momenta, respectively. Our numerical calculations of the final momentum distribution after the laser fields have passed in Figure 3.3 confirm equation (3.1): the mainly contributing region for each peak corresponds to $p'_3 = (n_+ - n_-)\omega$, for example $p'_3 \approx 2\omega$ at $\omega = 0.735m$. The latter means that the final dressed momenta q'_3 do not differ essentially from the momenta outside the laser field p'_3. In order to determine the resonance frequencies, we assume that the effective mass m_*, defined via $q^2 = m_*^2$, depends only on ξ as for an oscillating electric field, and that the initial quasi-momentum vanishes ($\mathbf{q} = 0$) because of the initial

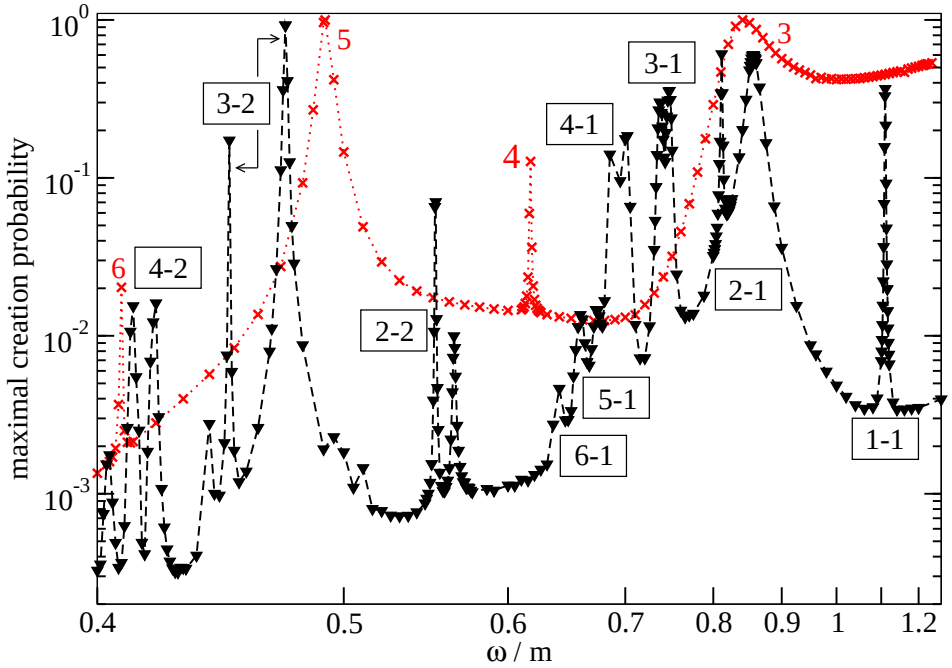

Figure 3.2: Resonant probability spectrum: Maximal value of the pair creation probability during Rabi oscillation at $\xi = 1$, varying the pulse length up to 200 cycles. The red crosses show the spectrum for an oscillating electric field; the peak labels denote the absorbed photon number. The black triangles show the CLP spectrum. Here the labeling signifies the number of absorbed photons from the right-left propagating waves. A splitting occurs, as indicated by arrows for the example of the (3-2) peak. The frequency axis is plotted reciprocally.

vanishing momentum $\mathbf{p} = 0$. Taking these assumptions into account, the resonance frequencies are given by

$$\omega = \frac{m_*}{2} \frac{n_+ + n_-}{n_+ n_-}. \tag{3.2}$$

This should be compared with the resonance condition obtained for an oscillating electric field [see equation (2.40)]. One may determine the laser dressed mass m_* with the aid of the highest frequency resonance peak at $\omega = 1.1m$ in Figure 3.2. The main contribution to the momentum spectrum for this peak comes from $p_3' = 0$, therefore the number of absorbed photons from the left and right laser beam are the same. This peak belongs to the lowest possible photon number $n_+ = n_- = 1$, resulting in $m_* = 1.11m$. For a certain multiphoton order there are now multiple resonance frequencies, e.g., for an $n = n_+ + n_- = 5$ photon transition there are two different resonance frequencies $\omega_{3,2}$ and $\omega_{4,1}$. The number of resonance lines is enhanced correspondingly. For the $n = 3$ photon resonance equation (3.2) predicts a unique frequency $\omega_{2,1}$, which however is not confirmed by the numerical results. Instead, for $n_+ \neq n_-$ the resonant peaks are always split into doublets, leading to a further enhancement of the number of resonance lines. This effect is not covered by equation (3.2) which rather predicts the center of the split lines.

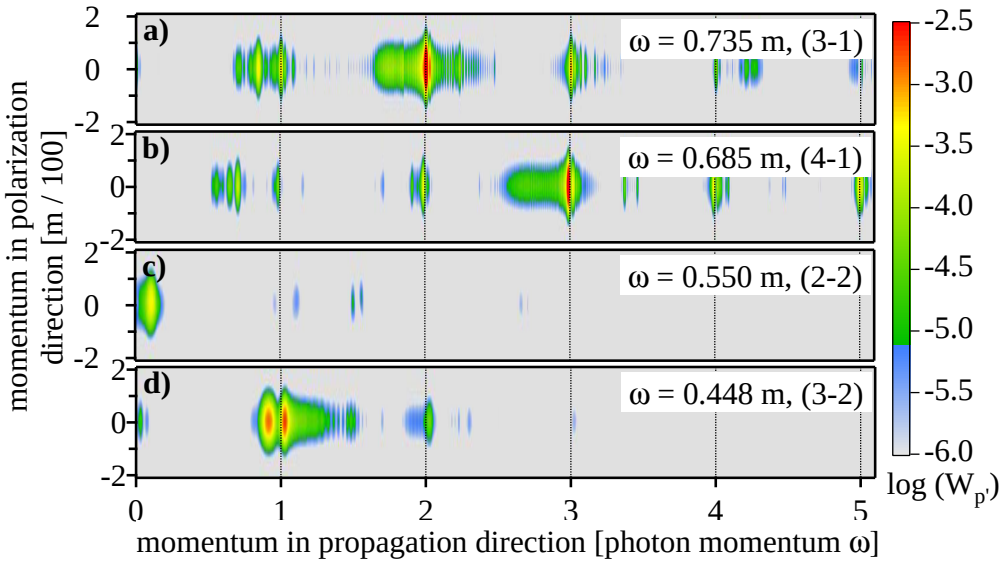

Figure 3.3: Final positive-energy momentum distributions $W_{p'} = |<\Phi^{(+)}_{\mathbf{p}'}|\Psi(T)>|^2$ after the interaction with two counterpropagating laser pulses ($\xi = 1$, $T = 150\pi/\omega$). Due to its magnetic component the field transfers longitudinal momentum to the wave packet. Shown are the results for four different frequencies corresponding to four peaks in the resonance spectrum in Fig. 3.2. Due to the symmetry of the spectra under momentum inversion $p'_3 \to -p'_3$, we only show the positive half of them.

Neglecting the splitting, which is explained in the next section, all peaks encountered in the resonance spectrum Figure 3.2 can be explained by equation (3.2) and correspond to the given labeling (n_+ - n_-). The interchange of $n_+ \leftrightarrow n_-$ gives the same resonant frequency, therefore we chose $n_+ \geq n_-$ for the labeling. All resonances with $n_- = 1$ lie above $\omega = m_*/2$, according to equation (3.2), which have been found up to a photon number of $n_+ + 1 = 7$. Their height decreases with increasing photon number.

The anticipated bandwidth of x-ray-free-electron lasers [102] would be sufficient to resolve the influence of the magnetic field component onto the resonance spectrum, due to a change of the relative resonance line separation: While, like in equation (2.40), a relative separation of $\sim 1/n$ remains between the most probable ($n_+ \simeq n_-$) resonance lines of different $n = n_+ + n_-$ values, the relative distance between the newly occurred resonance lines belonging to the same n value follows a $\sim 1/n^2$ behavior [see equation (2.40)].

So far we have explained the overall structure of the resonance spectrum in Fig. 3.2. There is however a substructure inherent to all resonance peaks with $n_+ \neq n_-$. The resonances are split into doublets which do not occur for an oscillating electric field. The origin of this splitting is explained in the following section.

3.2 The origin of the peak splitting

In the last section, the appearance of new resonances has been explained by the non-vanishing momentum of the laser photons, leading to different resonance frequencies for the absorption of different numbers of photons from the left and right coming laser pulse. There is however an additional substructure inherent to all resonance peaks with $n_+ \neq n_-$. The resonances are split into doublets which do not occur for an oscillating electric field. The keypoint to understand this splitting is again the photon momentum. In the case of CLP, the negative-energy electron can absorb n_+ photons from the left beam and n_- from the right, or vice versa, reaching two different final positive energy states with equal energy but opposite momentum. Therefore, the former two-level system in the case of an oscillating electric field is broken into a V-type three-level system (if $n_+ \neq n_-$) for CLP, depicted in Figure 3.4. The upper two levels have the same positive-energy but opposite momentum and are coupled via Compton scattering. This leads to a splitting of these levels and, consequently, to a splitting $\Delta\omega$ of the resonant transition frequency, analogous to the Autler-Townes effect [103].

We investigated the splitting for the (2 - 1) resonance more closely. For this $n = 3$ photon transition, the emergence of the splitting is shown in Figure 3.5 for increasing values of ξ. Figure 3.6 shows the found quadratic dependence of the splitting width $\Delta\omega \sim \xi^2$, leading to an increase of the splitting from $\xi = 0.5$ to $\xi = 1.0$ by a factor of 3.5. In addition we investigated the Compton oscillation between the two positive-energy states for two different ξ values. For this purpose, we started the calculation with an initial wave function in one of the upper levels, and examined the transition into the mirror state with the same energy but opposite momentum, shown in Figure 3.7. The Rabi frequency Ω_C due to Compton scattering increases by a factor of 3.6 when ξ is varied from 0.5 to 1. This indicates that the observed peak fine structure of the spectra is indeed an Autler-Townes-like effect. An equivalent explanation of the peak splitting can also be offered: The spatial periodicity of the field induces a band structure of the electron energies [104] which inhibits electron creation in certain energy regions. The splitting becomes larger with increasing ξ, following the energy gap behavior.

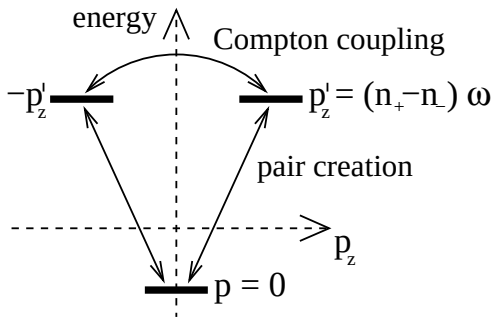

Figure 3.4: The two-level scheme of the oscillating electric field is broken into a V-type three-level scheme. The upper two levels have the same positive-energy but opposite momentum and are coupled via Compton scattering.

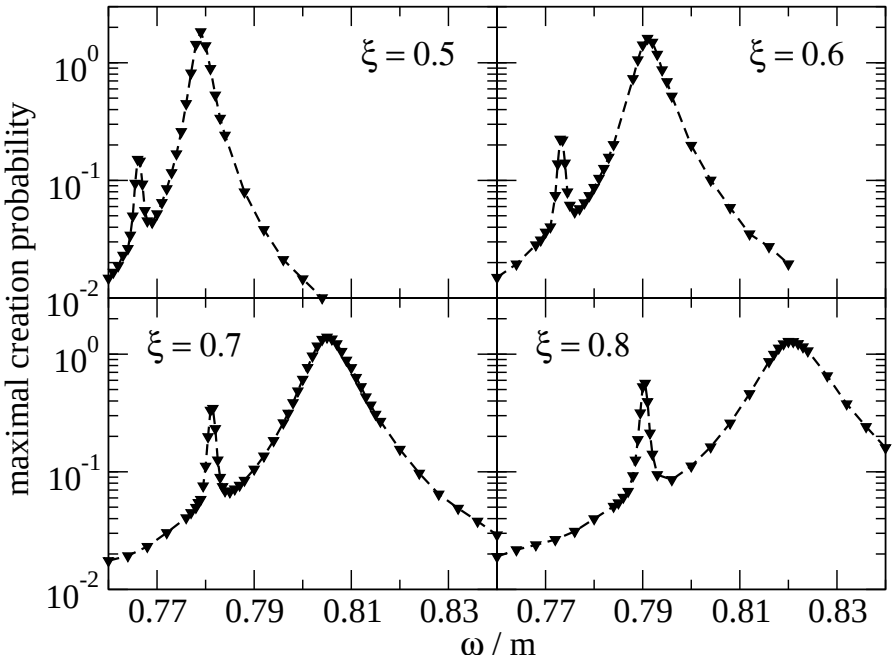

Figure 3.5: Splitting of the $n = 3$ photon resonance peak for various values of ξ. Note that the position of the main resonance increases, in accordance with the ξ dependent enhancement of m_*.

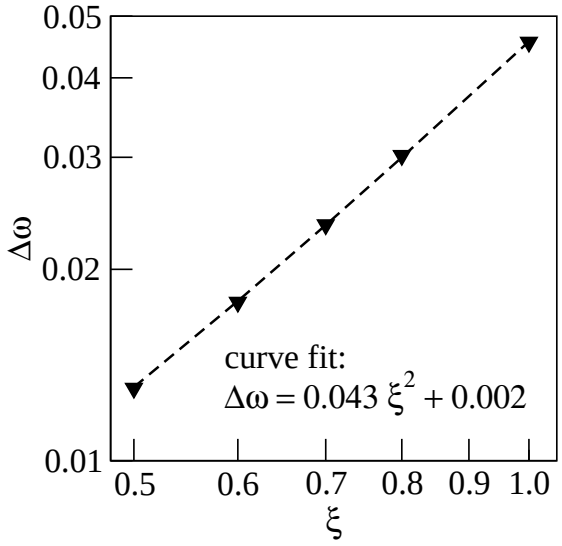

Figure 3.6: ξ dependence of the peak splitting shown in Figure 3.5, $\Delta\omega \sim \xi^2$.

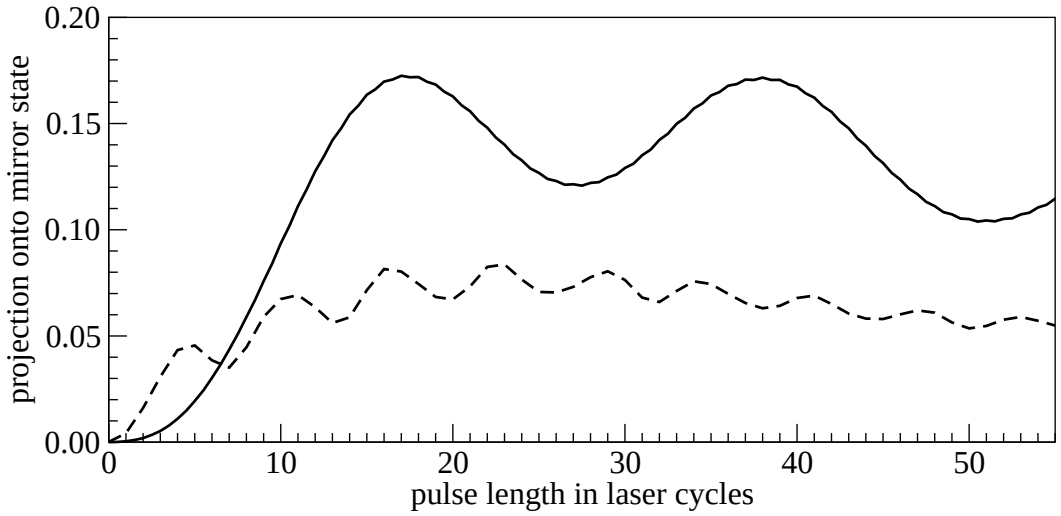

Figure 3.7: Coupling between the two upper states of the V-type system via Compton-scattering for the (2-1) peak. Shown is the population of the initially empty mirror state with $p_3' = -p_{\text{initial}} = -\omega$: (solid line) $\omega = 0.766m$ and $\xi = 0.5$, resulting in the Rabi frequency of $\Omega_C = 0.018m$ due to Compton scattering; (dashed line) $\omega = 0.812m$ and $\xi = 1.0$ resulting in $\Omega_C = 0.066m$. In both cases $\Omega \ll \Omega_C$, where Ω is the associated Rabi frequency due to pair creation.

Chapter 4

Conclusion

Employing the split-operator method to the Klein-Gordon equation in the two-component representation, enabled us to develop a highly efficient parallel computer code, propagating the Klein-Gordon equation on a one- or two- dimensional grid in arbitrary external potentials. The most noteable feature is the scaling behavior of the code for different numbers of employed CPU's; the speedup factor follows almost an optimal linear behavior. This program was applied to several toy systems to test the performance and the correctness of the results. Although simple but still especially interesting is the potential step, where a new physical interpretation of the Klein paradox was presented, different to the usual textbook arguments.

Furthermore we investigated e^+e^- pair creation in counterpropagating laser fields. The employed approach based on the intuitive picture of the Dirac sea. However, it has been shown, that this is in accordance to the field theoretical approach to vacuum decay in external fields with unstable vacuum [54]. In intuitive terms, this procedure is equivalent to describing the pair production as an electron transition from an initial negative-energy state (which corresponds to a positron in the final state) to a final positive-energy state. In the dipole approximation, a mathematical trick was established, enabling us to obtain the momentum distributions of the created particles in a single propagation. For circular polarization we encountered a crucial dependence on the spin orientation, which leads to an imbalance on the spin states of the produced electrons of approximately one order of magnitude. This difference has been explained by a spin-modified quasiclassical calculation.

Nowadays the experimental realization of laser-induced pair production is extensively discussed in connection with upcoming x-ray free-electron laser (XFEL) facilities. In this case, however, the laser frequency is high, $\xi \lesssim 1$ and the magnetic field component is not negligible. The latter, in general, can have an important influence on the pair creation process. Therefore we departed from the dipole approximation. This strongly influences the pair creation process for high laser frequencies. One of the most fundamental changes is the appearance of new resonances, due to the nonvanishing momentum of the laser photons. The anticipated bandwidth of x-ray-free-electron lasers [102] would be sufficient to resolve this new resonance structure.

The second important difference to the dipole approximation, is the splitting inherent to resonances where different numbers of photons are absorbed from each laser pulse. The simple two-level system of the oscillating electric field is broken into a V-type three-level system. A coupling of the upper two levels, due to Compton scattering gives rise to the observed peak doubling.

Appendix A

Numerical differentiation by finite differences

The calculation of the first and second order derivatives required in the Klein-Gordon algorithm are accomplished by finite differences. Here the order of accuracy depends on the order of the used approximation. The implementation provides n-point approximations from $n = 3$ up to $n = 9$. The index n in the expression "n-point approximation" denotes the number of points involved in the calculation.

For the first derivatives the following approximations are implemented:

$$f'(x) = \frac{1}{2h}\big[-f(x-h) + f(x+h)\big] + \mathcal{O}(h^2) \tag{A.1a}$$

$$f'(x) = \frac{1}{12h}\big[f(x-2h) - 8f(x-h) + 8f(x+h) - f(x+2h)\big] + \mathcal{O}(h^4) \tag{A.1b}$$

$$\begin{aligned} f'(x) = \frac{1}{60h}\big[&-f(x-3h) + 9f(x-2h) - 45f(x-h) \\ &+ 45f(x+h) - 9f(x+2h) + f(x+3h)\big] + \mathcal{O}(h^6) \end{aligned} \tag{A.1c}$$

$$\begin{aligned} f'(x) = \frac{1}{840h}\big[&3f(x+4h) - 32f(x-3h) + 168f(x-2h) - 672f(x-h) \\ &+ 672f(x+h) - 168f(x+2h) + 32f(x+3h) - 3f(x+4h)\big] + \mathcal{O}(h^8) \end{aligned} \tag{A.1d}$$

Note that here the value of the function at the position x is not required. Therefore the calculation of the first derivatives needs only $n-1$ values of the function. However, we still call these n-point approximations.

The approximations of the second order derivatives are given by:

$$f''(x) = \frac{1}{h^2}\big[f(x-h) - 2f(x) + f(x+h)\big] + \mathcal{O}(h^2) \tag{A.2a}$$

$$\begin{aligned} f''(x) = \frac{1}{12h^2}\big[&- f(x-2h) + 16f(x-h) - 30f(x) \\ &+ 16f(x+h) - f(x+2h)\big] + \mathcal{O}(h^4) \end{aligned} \tag{A.2b}$$

$$\begin{aligned} f''(x) = \frac{1}{180h^2}\big[&2f(x-3h) - 27f(x-2h) + 270f(x-h) - 490f(x) \\ &+ 270f(x+h) - 27f(x+2h) + 2f(x+3h)\big] + \mathcal{O}(h^6) \end{aligned} \tag{A.2c}$$

$$\begin{aligned} f''(x) = \frac{1}{5040h^2}\big[&- 9f(x+4h) + 128f(x-3h) - 1008f(x-2h) \\ &+ 8064f(x-h) - 14350f(x) + 8064f(x+h) - 1008f(x+2h) \\ &+ 128f(x+3h) - 9f(x+4h)\big] + \mathcal{O}(h^8) \end{aligned} \tag{A.2d}$$

The order of accuracy goes like $\mathcal{O}(h^{n-1})$ for an n-point approximation. Here h denotes the grid increment. Although the employment of higher order approximations gives larger accuracy, it also slows down the computation for the parallel implementation, because higher amounts of data have to be exchanged. All of the calculations presented employed the 5-point approximation with an accuracy of order $\mathcal{O}(h^4)$.

Bibliography

[1] F. Sauter, Über das Verhalten eines Elektrons im homogenen elektrischen Feld nach der relativistischen Theorie Diracs, Zeitschrift für Physik **69**, 742 (1931)

[2] W. Heisenberg and H. Euler, Folgerungen aus der Diracschen Theorie des Positrons, Zeitschrift für Physik **98**, 714 (1936)

[3] J. Schwinger, On gauge invariance and vacuum polarization, Physical Review **82**, 664 (1951)

[4] C. Bottcher and M. R. Strayer, Numerical Solution of the Time-Dependent Dirac Equation with Application to Positron Production in Heavy-Ion Collisions, Physical Review Letters **54**, 669 (1985)

[5] J. Eichler, Theory of relativistic ion-atom collisions, Physics Report **193**, 165 (1990)

[6] A. Belkacem, H. Gould, B. Feinberg, R. Bossingham, and W. E. Meyerhof, Measurement of electron capture from electron-positron pair production in relativistic heavy ion collisions, Physical Review Letters **71**, 1514 (1993)

[7] G. Baur, K. Hencken, and D. Trautmann, Electron-positron pair production in ultrarelativistic heavy ion collisions Physics Report **453**, 1 (2007)

[8] E. Brezin and C. Itzykson, Pair Production in Vacuum by an Alternating Field, Physical Review D **2**, 1191 (1970)

[9] V. S. Popov, Production of e^+e^- pairs in an alternating external field, JETP Letters **13**, 185 (1971)

[10] V. Yanovsky, V. Chvykov, G. Kalinchenko, P. Rousseau, T. Planchon, T. Matsuoka, A. Maksimchuk, J. Nees, G. Cheriaux, G. Mourou, and K. Krushelnick, Ultra-high intensity- 300-TW laser at 0.1 Hz repetition rate, Optics Express **16**, 2109 (2008)

[11] C. N. Danson, P. A. Brummitt, R. J. Clarke, J. L. Collier, B. Fell, A. J. Frackiewicz, S. Hancock, S. Hawkes, C. Hernandez-Gomez, P. Holligan, M. H. R. Hutchinson, A. Kidd, W. J. Lester, I. O. Musgrave, D. Neely, D. R. Neville, P. A. Norreys, D. A. Pepler, C. J. Reason, W. Shaikh, T. B. Winstone, R. W. W. Wyatt, and B. E. Wyborn, Vulcan Petawatt-an ultra-high-intensity interaction facility, Nuclear Fusion **44**, S239 (2004)

[12] J. M. Soures, Progress Report on the Laboratory for Laser Energetics (2007). `http://www.lle.rochester.edu/05_omega/05_omega.html`

[13] G. D. Tsakiris, K. Eidmann, J. Meyer-ter-Vehn and F. Krausz, Route to intense single attosecond pulses, New Journal of Physics **8**, 19 (2006)

[14] Ph. Zeitoun, G. Faivre, S. Sebban, T. Mocek, A. Hallou, M. Fajardo, D. Aubert, Ph. Balcou, F. Burgy, D. Douillet, S. Kazamias, G. de Lacheze-Murel, T. Lefrou, S. le Pape, P. Mercere, H. Merdji, A. S. Morlens, J. P. Rousseau, and C. Valentin, A high-intensity highly coherent soft X-ray femtosecond laser seeded by a high harmonic beam, Nature, **431**, 426 (2004)

[15] G. Materlik and T. Tschentscher, editors, The x-ray free electron laser, volume 5 of TESLA Technical Design Report, DESY, Hamburg (2001)
`http://tesla.desy.de/new_pages/TDR_CD/PartV/fel.html`

[16] F. V. Hartemann, W. J. Brown, D. J. Gibson, S. G. Anderson, A. M. Tremaine, P. T. Springer, A. J. Wootton, E. P. Hartouni, and C. P. J. Barty, High-energy scaling of Compton scattering light sources, Physical Review Special Topics - Accelerators and Beams **8**, 100702 (2005)

[17] PHELIX, Petawatt High-Energy Laser for Heavy-Ion EXperiments, GSI-98-10 report (1998)
`http://www.gsi.de/forschung/phelix/index.html`

[18] Proposal for a European Extreme Light Infrastructure (2006)
`http://www.eli-laser.eu`

[19] M. Dunne et al., HiPER Technical Background and Conceptual Design Report (2007)
`http://www.hiper-laser.org`

[20] G. A. Mourou, T. Tajima, and S. V. Bulanov, Optics in the relativistic regime, Reviews of Modern Physics **78**, 309 (2006)

[21] M. Marklund and P. K. Shukla, Nonlinear collective effects in photon-photon and photon-plasma interactions, Reviews of Modern Physics **78**, 591 (2006)

[22] Y. I. Salamin, S-X. Hu, K. Z. Hatsagortsyan, and C. H. Keitel, Relativistic high-power laser-matter interactions, Physics Reports **427**, 41 (2006)

[23] W. Becker, Quantum electrodynamics in intense laser fields , Laser and Particle Beams **9**, 603 (1991)

[24] A. Ringwald, Pair production from vacuum at the focus of an X-ray free electron laser, Physics Letters B **510**, 107 (2001)

[25] D. L. Burke, R. C. Field, G. Horton-Smith, J. E. Spencer, D. Walz, S. C. Berridge, W. M. Bugg, K. Shmakov, A. W. Weidemann, C. Bula, K. T. McDonald, E. J. Prebys, C. Bamber, S. J. Boege, T. Koffas, T. Kotseroglou, A. C. Melissinos, D. D. Meyerhofer, D. A. Reis, and W. Ragg, Positron Production in Multiphoton Light-by-Light Scattering, Physical Review Letters **79**, 1626 (1997)

[26] V. S. Popov, Method of imaginary time for periodical fields, Yadernaya Fizika **19**, 1140 (1974) [Soviet Journal of Nuclear Physics **19**, 584 (1975)]

[27] V. S. Popov, Resonant pair production in a strong electric field, JETP Letters **18**, 255 (1973)

[28] N. B. Narozhny and A. I. Nikishov, Pair production by a periodic electric field, Soviet Physics JETP **38**, 427 (1974)

[29] V. M. Mostepanenko and V. M. Frolov, Production of particles from vacuum by a uniform electric field with periodic time dependence, Soviet Journal of Nuclear Physics **19**, 451 (1974)

[30] A. A. Grib, S. G. Mamayev, and V. M. Mostepanenko, Vacuum quantum effects in strong fields, Friedmann - St. Petersburg, (1994)

[31] H. K. Avetissian, A. K. Avetissian, G. F. Mkrtchian, and Kh. V. Sedrakian, Electron-positron pair production in the field of superstrong oppositely directed laser beams, Physical Review E **66**, 016502 (2002)

[32] Q. Su and R. Grobe, Oscillatory pair-creation probabilities in time-dependent subcritical forces, Laser Physics **17**, 92 (2007)

[33] H. M. Fried, Y. Gabellini, B. H. J. McKellar, and J. Avan, Pair production via crossed lasers, Physical Review D **63**, 125001 (2001)

[34] M. V. Fedorov, M. A. Efremov, and P. A. Volkov, Double- and multi-photon pair production and electron-positron entanglement, Optics Communications **264**, 413 (2006)

[35] M. Marklund, B. Eliasson, P. K. Shukla, L. Stenflo, M. E. Dieckmann, and M. Parviainen, Electrostatic pair creation and recombination in quantum plasmas, JETP Letters **83**, 313, (2006)

[36] R. Schützhold, H. Gies, and G. Dunne, Dynamically Assisted Schwinger Mechanism, Physical Review Letters **101**, 130404 (2008)

[37] A. R. Bell and J. G. Kirk, Possibility of Prolific Pair Production with High-Power Lasers, Physical Review Letters **101**, 200403 (2008)

[38] P. Krekora, Q. Su, and R. Grobe, Klein Paradox in Spatial and Temporal Resolution, Physical Review Letters **92**, 040406 (2004)

[39] P. Krekora, Q. Su, and R. Grobe, Transition into the negative-energy Dirac continuum, Physical Review A **70**, 054101 (2004)

[40] P. Krekora, Q. Su, and R. Grobe, Relativistic Electron Localization and the Lack of Zitterbewegung, Physical Review Letters **93**, 043004 (2004)

[41] P. Krekora, Q. Su, and R. Grobe, Interpretational difficulties in quantum field theory, Physical Review A **73**, 022114 (2006)

[42] C. C. Gerry, Q. Su, and R. Grobe, Timing of pair production in time-dependent force fields, Physical Review A **74**, 044103 (2007)

[43] N. I. Chott, Q. Su, and R. Grobe, Classical-quantum correspondence in electron-positron pair creation, Physical Review A **76**, 010101 (2007)

[44] V. S. Popov, The Schwinger effect and possibilities for its observation using optical and X-ray lasers, JETP **94**, 1057 (2002)

[45] V. S. Popov, On Schwinger mechanism of e^+e^- pair production from vacuum by the field of optical and X-ray lasers, Physics Letters A **298**, 83 (2002)

[46] N. B. Narozhny, S. S. Bulanov, V. D. Mur, and V. S. Popov, e^+e^--pair production by a focused laser pulse in vacuum, Physics Letters A **330**, 1 (2004)

[47] A. Di Piazza, Pair production at the focus of two equal and oppositely directed laser beams: The effect of the pulse shape, Physical Review D **70**, 053013 (2004)

[48] S. S. Bulanov, N. B. Narozhny, V. D. Mur, and V. S. Popov, Electron-positron pair production by electromagnetic pulses, JETP **102**, 9 (2006)

[49] V. S. Popov, Schwinger mechanism of electron-positron pair production by the field of optical and X-ray lasers in vacuum, JETP Letters **74**, 133 (2001)

[50] M. Ruf, G. R. Mocken, C. Müller, K. Z. Hatsagortsyan, and C. H. Keitel, Pair production in laser fields oscillating in space and time, Physical Review Letters **102**, 080402 (2009)

[51] H. Gies and K. Klingmüller, Pair production in inhomogeneous fields, Physical Review D **72**, 065001 (2005)

[52] G. V. Dunne and C. Schubert, Worldline instantons and pair production in inhomogenous fields, Physical Review D **72**, 105004 (2005)

[53] G. V. Dunne, Q. Wang, H. Gies, and C. Schubert, Worldline instantons and the fluctuation prefactor, Physical Review D **73**, 065028 (2006)

[54] E. S. Fradkin, D. M. Gitman, and S. M. Shvartsman, Quantum-Electrodynamics with unstable vacuum, Springer, (1991)

[55] G. R. Mocken and C. H. Keitel, Quantum dynamics of relativistic electrons, Journal of Computational Physics **199**, 558 (2004)

[56] G. R. Mocken and C. H. Keitel, FFT-split-operator code for solving the Dirac equation in $2+1$ dimensions, Computer Physics Communications **178**, 868 (2008)

[57] F. Schwabl, Quantum Mechanics, 4th edition, Springer, (2007)

[58] J. J. Sakurai, Modern Quantum Mechanics, revised edition, Addison Wesley, (1994)

[59] M. D. Feit, J. A. Fleck Jr., and A. Steiger, Solution of the Schrödinger equation by a spectral method, Journal of Computational Physics **47**, 412 (1982)

[60] A. D. Bandrauk and H. Shen, Exponential split operator methods for solving coupled time-dependent Schrödinger equations, Journal of Chemical Physics **99**, 1185 (1993)

[61] J. W. Braun, Q. Su, and R. Grobe, Numerical approach to solve the time-dependent Dirac equation, Physical Review A **59**, 604 (1999)

[62] J. Javanainen,and J. Ruostekoski, Symbolic calculation in development of algorithms: split-step methods for the Gross-Pitaevskii equation, Journal of Physics A **39**, L179 (2006)

[63] G. M. Muslu and H. A. Erbay, Higher order split-step Fourier schemes for the generalized non-linear Schrödinger equation, Mathematics and Computers in Simulation **67**, 581 (2005)

[64] H. Feshbach and F. Villars, Elementary relativistic wave mechanics of spin 0 and spin 1/2 particles, Reviews of Modern Physics **30**, 24 (1958)

[65] F. Schwabl, Advanced Quantum Mechanics, 4th edition, Springer, (2008)

[66] P. Strange, Relativistic Quantum Mechanics with Applications in Condensed Matter and Atomic Physics, Cambridge University Press, (1998)

[67] F. Gross, Relativistic Quantum Mechanics and Field Theory, Wiley & Sons, (1999)

[68] W. Greiner, Relativistic Quantum Mechanics - Wave Equations, 3rd edition, Springer, (2000)

[69] A. Wachter, Relativistische Quantenmechanik, Springer, (2005)

[70] H. Kragh, Equation with many fathers. The Klein-Gordon equation in 1926, American Journal of Physics **52**, 1024 (1984)

[71] A. Mostafazadeh, Pseudo-Hermitian quantum mechanics, arXiv: 0810.5643 (2008)

[72] A. Mostafazadeh, Pseudo-unitary operators and pseudo-unitary quantum dynamics, Journal of Mathematical Physics **45**, 932 (2004)

[73] W. B. Berestetzki, E. M. Lifschitz, and L. P. Pitajewski, Lehrbuch der theoretischen Physik IV - Quatenelektrodynamik, (IV. Band der Lehrbuchreihe von L. Landau und E. M. Lifschitz), 7. Auflage, Akademie Verlag, (1991)

[74] Y. I. Salamin and F. H. M. Faisal, Harmonic generation by superintense light scattering from relativistic electrons, Pysical Review A **54**, 4383 (1996)

[75] O. Klein, Die Reflektion von Elektronen an einem Potentialsprung nach der relativistischen Dynamik von Dirac, Zeitschrift für Physik,**53**, 157 (1929)

[76] L. H. Ryder, Quatum Field Theory, second edition, Cambridge University Press, (2003)

[77] A. I. Nikishov, Problems of intense external-field intensity in quantum electrodynamics, Journal of Russian Laser Research **6**, 619 (1985)

[78] A. Das, Field Theory a Path Integral Approach, second edition, World Scientific Publishing, (2006)

[79] H. Goldstein, C. Poole, and J. Safko, Classical Mechanics, 3rd edition, Addison Wesley (2002)

[80] G. R. Mocken, M. Ruf, C. Müller, and C. H. Keitel, Resonant and non-resonant electron-positron pair creation in laser fields, to be submitted

[81] V. P. Yakovlev, Electron-Positron pair production by a strong electromagnetic wave in the field of a nucleus, Soviet Physics JETP, **22**, 223 (1964)

[82] C. Müller, A. B. Voitkiv, and N. Grün, Differential rates for multiphoton pair production by an ultrarelativistic nucleus colliding with an intense laser beam, Physical Review A **67**, 063407 (2003)

[83] C. Müller, A. B. Voitkiv, and N. Grün, Nonlinear Bound-Free Pair Creation in the Strong Electromagnetic Fields of a Heavy Nucleus and an Intense X-Ray Laser, Physical Review Letters **91**, 223601 (2003)

[84] A. I. Milstein, C. Müller, K. Z. Hatsagortsyan, U. D. Jentschura, and C. H. Keitel, Polarization-operator approach to electron-positron pair production in combined laser and Coulomb fields, Physical Review A **73**, 062106 (2006)

[85] C. Müller, C. Deneke, and C. H. Keitel, Muon-Pair Creation by Two X-Ray Laser Photons in the Field of an Atomic Nucleus, Physical Review Letters **101**, 060402 (2008)

[86] C. Deneke and C. Müller, Bound-free e^+e^- pair creation with a linearly polarized laser field and a nuclear field, Physical Review A **78**, 033431 (2008)

[87] C. Müller, Nonlinear Bethe-Heitler pair creation with attosecond laser pulses at the LHC, Physics Letters B **672**, 56 (2009)

[88] A. I. Nikishov and V. I. Ritus, Quantum processes in the field of a plane electromagnetic wave and in a constant field. I, Soviet Physics JETP **19**, 529 (1964)

[89] A. I. Nikishov and V. I. Ritus, Quantum processes in the field of a plane electromagnetic wave and in a constant field, Soviet Physics JETP **19**, 1191 (1964)

[90] A. I. Nikishov and V. I. Ritus, Nonlinear effects in Compton Scattering and pair production owing to absorption of several photons, Soviet Phyics JETP **20**, 757 (1965)

[91] V. I. Ritus, Quantum effects of the interaction of elementary particles with an intense electromagnetic field, Journal of Russian Laser Research **6**, 497 (1985)

[92] N. B. Narozhny, S. S. Bulanov, V. D. Mur, and V. S. Popov, On e^+e^- pair production by colliding electromagnetic pulses, JETP Letters **80**, 382 (2004)

[93] P. Krekora, K. Cooley, Q. Su, and R. Grobe *et al.*, Creation Dynamics of Bound States in Supercritical Fields, Physical Review Letters **95**, 070403 (2005)

[94] D. B. Blaschke, A. V. Prozorkevich, C. D. Roberts, S. M. Schmidt, and S. A. Smolyansky, Pair Production and Optical Lasers, Physical Review Letters **96**, 140402 (2006)

[95] R. Alkofer, M. B. Hecht, C. D. Roberts, S. M. Schmidt, and D. V. Vinnik, Pair Creation and an X-Ray Free Electron Laser, Physical Review Letters **87**, 193902 (2001)

[96] C. D. Roberts, S. M. Schmidt, and D. V. Vinnik, Quantum Effects with an X-Ray Free-Electron Laser, Physical Review Letters **89**, 153901 (2002)

[97] C. Müller, K. Z. Hatsagortsyan, M. Ruf, S. Müller, H. G. Hetzheim, M. C. Kohler, and C. H. Keitel, Relativistic Nonperturbative Above-Threshold Phenomena in Strong Laser Fields, submitted (2009)

[98] M. O. Scully and M. S. Zubairy, Quantum Optics, Cambridge University Press, (2002)

[99] J. D. Bjorken and S. D. Drell, Relativistische Quantenmechanik, Spektrum Akademischer Verlag (1998)

[100] V. S. Popov, The imaginary time method for periodic fields, Soviet Journal of Nuclear Physics **19**, 584 (1974)

[101] J. D. Jackson, Classical Electrodynamics, 3rd edition, Wiley & Sons (1999)

[102] M. Altarelli, *et al.*, technical Design Report of the European XFEL, DESY 2006-097
`http://www.xfel.eu`

[103] S. H. Autler and C. H. Townes, Stark Effect in Rapidly Varying Fields, Physical Review **100**, 703 (1955)

[104] Shown for an electron moving in a standing wave of circular polarization:
W. Becker and H. Mitter, Motion of relativistic particles in standing-wave fields. II. Particles with spin, Journal of Physics A: Mathematical and General **12**, 2407 (1979)

Acknowledgment

At this point I want to express my gratitude to all people who contributed to this work and made it an enjoyable task.

First of all, I want to thank Christoph H. Keitel for turning my interest onto this fascinating subject, his supervision, and for giving me the opportunity to do this project at the Max Planck Institute for Nuclear Physics.

I am especially grateful to Carsten Müller and Karen Z. Hatsagortsyan for all the enlightening discussions, their time and patience. Without their support and advice this work would not have been possible.

Special thanks go to Guido R. Mocken and Heiko Bauke for advice and discussions on programming issues concerning C++.

I am also very grateful to Peter Brunner, for fixing all the computer problems and keeping my computer up to date. Without his help I would have been totally lost.

I acknowledge an enlightening discussion with Dieter Bauer during lunch on the subject of Autler-Townes splitting.

Last but not least thanks to all the roommates and fellow colleagues who created such a pleasant atmosphere (in alphabetic order): Héctor Mauricio Castañeda Cortés, Antonino Di Piazza, Hossein Ebadi, Jörg Evers, Robert Fischer, Robert Fleischhaker, Adriana Gagyi-Pálffy, Martin Haas, Zoltán Harman, Henrik Hetzheim, Bastian Jungnitsch, Martin Kiffner, Ben King, Michael Klaiber, Markus Kohler, Erik Lötstedt, Felix Mackenroth, Sarah Müller, Stefan Pieper, Octavian Postavaru, Michael Ruggenthaler, Sandra Schmid, Andreas Staudt, David Stiff, Mario Verschl, Florian Wilken and Benedikt Wundt. Thanks to all of you for the friendships that evolved over these years. Special thanks go to Robert Fischer and Stefan Pieper for all the memorable hours during the teaching period at the university and the numerous discussions, Mario for the bell, Andreas Staudt for all the weird films, and finally Michael Ruggenthaler for revealing me strange foreign lands.